Chip scale low dimensional materials: optoelectronics & nonlinear optics

Tingyi Gu

Submitted in partial fulfillment of the requirements
for the degree of Doctor of Philosophy in the Graduate School of Arts and Sciences

COLUMBIA UNIVERSITY
2014

ABSTRACT

Chip Scale Low Dimensional Materials: Optoelectronics & Nonlinear Optics

Tingyi Gu

The CMOS foundry infrastructure enables integration of high density, high performance optical transceivers. We developed integrated devices that assemble resonators, waveguide, tapered couplers, *pn* junction and electrodes. Not only the volume standard manufacture in silicon foundry is promising to low-lost optical components operating at IR and mid-IR range, it also provides a robust platform for revealing new physical phenomenon.

The thesis starts from comparison between photonic crystal and micro-ring resonators based on chip routers, showing photonic crystal switches have small footprint, consume low operation power, but its higher linear loss may require extra energy for signal amplification. Different designs are employed in their implementation in optical signal routing on chip. The second part of chapter 2 reviews the graphene based optoelectronic devices, such as modulators, lasers, switches and detectors, potential for group IV optoelectronic integrated circuits (OEIC).

In chapter 3, the highly efficient thermal optic control could act as on-chip switches and (transmittance) tunable filters. Local temperature tuning compensates the wavelength differences between two resonances, and separate electrode is used for fine tuning of optical pathways between two resonators. In frequency domain, the two cavity system also serves as an optical analogue of Autler-Towns splitting, where the cavity-cavity resonance detuning is controlled by the length of pathway (phase) between them. The high thermal sensitivity of cavity resonance also effectively reflects the heat distribution around the nanoheaters, and thus derives the thermal

conductivity in the planar porous suspended silicon membrane.

Chapter 4 & 5 analyze graphene-silicon photonic crystal cavities with high Q and small mode volume. With negligible nonlinear response to the milliwatt laser excitation, the monolithic silicon PhC turns into highly nonlinear after transferring the single layer graphene with microwatt excitation, reflected by giant two photon absorption induced optical bistability, low power dynamic switching and regenerative oscillation, and coherent four-wave-mixing from high Kerr coefficient. The single layer graphene lowers the operational power 20 times without enhancing the linear propagation loss.

Chapter 6 moves onto high Q ring resonator made of plasma enhanced chemical vapor deposition grown silicon nitride (PECVD SiN). PECVD SiN grown at low temperature is compatible with CMOS processing. The resonator enhanced light-matter interaction leads to molecular absorption induced quality factor enhancement and thermal bistability, near the critical coupling region.

In chapter 7, carrier transport and recombination in InAs quantum dots based GaAs solar cells are characterized by current-voltage curve. The parameters include voltage dependent ideality factor, series and shunt resistance. The device variance across the wafer is analyzed and compared. Quantum dots offers extra photocurrent by extending the absorption edge further into IR range, but the higher recombination rate increases the dark current as well. Different dots sized enabled by growth techniques are employed for comparison.

Contents

List of Tables

List of Figures

states |e> and |g> with coupled strength g(t). (c) Energy state in Atom in cavity. (d) (up) Photocounting rates for cavity output (dash line) and for atomic spontaneous emission (solid line). (down) Phase of intracavity light field.

3-2: Schematic of two coupled cavity system. (a) The coupling coefficient between cavity and waveguide $\kappa=(1/2/\tau_c)^{1/2}$ (b) Schematics of (b) EIT mechanism, (c) superradiance two cavity coupled system in a. (i). Electromagnetically-Induced-Transparency (δ=1.9, βL=0) red dot line is the experimental data and the blue solid curve is the coupled mode theory simulation (ii): Superradiance condition. Light blue dash line is the single cavity dip (δ=0.1, $\beta L=\pi$). The external tuning is realized by the integrated electrode fine tuning of the local refractive index

3-3: Phase dependent cavity-cavity splitting (a) 2D FDTD simulation showing the eigen modes of the two cavity system with different optical path between two cavities. The magnitude of the electric field in waveguide evolves with time. The insets are eigen states with different relative phase, with zero detuning between two cavities. The distance between two cavities is (i) 3a (ii) 2a (b) Coupled mode theory simulated energy spectrum with different phase between two cavities. The blue curve is the spectrum of the left cavity, and the red curve is the right cavity. (i) phase=0.5π (ii) phase=0π

3-4: Experimental observation of phase determined cavity-cavity splitting (a) Measured (Blue solid line) and CMT simulated transmission spectrum (Red dashed line) with increasing phase tuning power (P_Φ), and fixed resonance tuning power (P_r=40.8 mW).(b) The CMT extracted inter-cavity splitting versus the phase tuning power. The blue dots are experimental data for 0 resonance detuning, and the green squares are for

the 0.1 resonance detuning. The lines are used for guiding eyes. (c) The CMT extracted inter-cavity phase.

3-5: Chip-scale integrated tuning of photonic crystal two-cavity optical EIT system. (a) SEM of thermally-tuned coupled cavities with thermal isolation trench and tuning electrodes. Scale bar: 5 μm. (b) SEM of single cavity. Scale bar: 500 nm. (c) 3D FDTD simulated model profile (log scale) with outline of thermal tuning electrode. (d) Schematics of two-step nanofabrication process flow. (i) SOI wafer, (ii) electron-beam lithography defined tuning electrodes, (iii) suspended silicon membrane with electrodes. (ii') initial sacrificial release, following by (iii') electron-beam writing of the electrodes.

3-6: Device nanofabrication flow chat (a) SOI structure with photonic crystal patterned on the top silicon layer. The thickness for photonic crystal layer and silicon oxide layers are 250 nm and 1 um respectively. (b) SOI structure with 200nm PMMA coating (c) Ebeam lithography for defining the metal part (d) PMMA development by MIBK:IPA (e) Chrome deposition (f) Lift-off (g) Spin casting photoresist (h) Photolithography (i) BOE wet etch (j) Sample cleaned by Aceton for removing the photoresist.

3-7: Integrated tuning of the two-cavity resonances. (a) The resonant wavelength of the active cavity (solid squares) and the target cavity (empty circles) versus the tuning power. Inset: fine tuning cavity resonances in the cavity-cavity interference region. (b) Detuning versus local tuning power within the same region as inset of (a). Solid and empty squares are data measured at base temperature (T_0) and T_0+14K respectively. Lines are linear fits. (c) Example two-cavity coherent transmission under different local tuning powers (δ = 2.3, 2.6, 2.9 and 4.0, correspondent to cavity tuning power at 3.59 mW, 3.46

mW, 3.39 mW and 3.26 mW respectively) . Solid (black) lines are experimental data and the dashed (red) lines are coupled-mode theory fits. Curves are offset by -0.5 for clarity.

3-8: Measurement for chip level thermal-optic tuning. (a) Experimental set-up. Inset: detailed configuration. The blue part is the chip and two fibers. The thermistor (yellow part) is placed on top of the chip (Thorlabs TH10K). The heating source (red part) is placed under the chip holder (grey part). (b) Resistance as a function of Thermistor temperature for the thermistor. The blue curve is the electrical specification given by the data sheet. The red circles mark the temperature (24oC, 32oC, 66oC) the transmission of the resonators are measured. (c) The resonance shift of four photonic crystal cavities with different quality factors (blue circles) and the Fabry Perod oscillation (grey dash line).

3-9: Fabrication and measurements of cavity tuning in photonic crystal systems. a, Schematic of nanofabrication process flow b, SEM of suspended photonic crystal membrane with micro-electrodes. Inset: 2D FDTD simulations of optical field distribution and its relative position to serpent electrodes. c, Transmitted spectrum with different electrical power supply. Bright lines show the drifting of cavity resonances and fringes in the background is the Fabry-Perot oscillation.

4-1: Conductivity and permittivity of graphene in the IR range. (a-b) The real and imaginary parts of the total conductivity; (c-d) permittivity, with Fermi level set at -0.4eV (red dashed line) and -0.2eV (blue solid line) respectively.

4-2: Optical field distribution and calculation for effective kerr nonlinearity of the hybrid graphene-silicon waveguide. (a) The refractive index on the x=0 plane. The

white part is the silicon (n=3.45) and the dark part is the air (n=1), (b-c) real and imaginary parts of TE polarized electric field distribution on the across section in (a), (d) The refractive index on the y=0 plane. (e-f) real and imaginary parts of TE polarized electric field in (d).(g) The amplitude of electric field along the cross section of waveguide (upper), and effective area (down) along the waveguide direction. (h) nonlinear parameter γ ($=\omega n_2/cA_{eff}$) and effective kerr coefficient of graphene silicon waveguide.

4-3: Raman spectrum and transferred graphene samples. (a) Raman G peak (black line) and its inverse (grey dashed line) to illustrate G peak symmetry. Inset: optical micrograph of the device with graphene transferred under Raman measurement. (b) A centimeter-scale graphene film prepared. Optical micrograph of graphene film transferred to various substrates (PMMA), air-bridged silicon membranes, silicon oxide and partially covered metal surfaces, with graphene interface pictured. (c) Scanning electronic micrograph of example air-bridged device sample with graphene covering the whole area except the dark (exposed) region. Scale bar: 500 nm. (d) Complete Raman spectrum of the graphene-clad silicon membrane samples.

4-4: Graphene transferred on patterned 250nm thick suspended silicon membrane. **a,** SEM of the device. Scale bar: 1μm, **b,** AFM imaged surface topology of 1μm by 1μm **c,** AFM imaged surface topology **c,** AFM imaged surface topology of graphene partially covered on the silicon photonic crystal substrate. **d,** EFM phase mapping imaging the surface conductivity as in **c**. Suspended graphene over the wholes of the silicon shows higher conductivity.

4-5: Device layout and measurement. (a) Structure schematic of an L3 cavity switch formed in graphene cladded silicon membrane. (b). The electric field distribution along z direction simulated by FDTD method. The graphene sheet (brown line) is placed on 250nm thick silicon membrane. Inset: Schematics of graphene band diagram with photon energy of pump (green), and converted ones (red and blue) (c). Top view of optic field energy distribution of an isolated S1 shifted L3 cavity. The FDTD simulation of mode profile is superimposed on the SEM picture S1 shifted L3 cavity with graphene cladding, with mode volume: $0.073\mu m^3$, and quality factor ~2.0×10^4 Scale bar: 100nm. (d). CMOS processed integrated optical devices under test. The open window is for silicon membrane undercut and graphene cladding on the photonic crystal part.

4-6: Free-carrier absorption effects on the four-wave mixing conversion efficiency. Measured idler power versus signal power at the transmitted port, with the pump power is fixed on the cavity resonance and the the signal laser detuned by 200 pm. Experimental data (×) and quadratic fit (solid line). Inset: corresponding conversion efficiency versus signal power.

4-7: Parametric four-wave mixing in graphene-cladded silicon nanocavities. (a) Measured transmission spectrum with signal laser fixed at -0.16 nm according to cavity resonance, and pump laser detuning is scanned from -0.1 to 0.03 nm. Inset: band diagram of degenerate four-wave mixing process with pump (green), signal (blue) and idler (red) lasers. (b) Measured transmission spectrum with pump laser fixed on cavity resonance, and signal laser detuning is scanned from -0.04 to -0.27 nm. (c) Modeled conversion efficiency versus pump and signal detuning from the cavity resonance. (d) Observed and

simulated conversion efficiencies of the cavity. Red solid dots are measured with signal detuning as in panel b, and the empty circles are obtained through pump detuning as in panel a, plus 29.5-dB (offset due to the 0.16 nm signal detuning). Solid and dashed black lines are modeled conversion efficiencies of graphene-silicon and monolithic silicon cavities respectively. Grey dashed line (superimposed): illustrative pump/signal laser spontaneous emission noise ratio.

5-1: Graphene-cladded silicon photonic crystal nanostructures: (a) Scanning electron micrograph (SEM) of tuned photonic crystal cavity, with lattice constant *a* of 420 nm. Example SEM with separated graphene monolayer on silicon for illustration. Scale bar: 500 nm. Inset: example E_z-field from finite-difference time-domain computations. Right inset: Dirac cone illustrating the highly-doped Fermi level (dashed blue circle) allowing only two-photon transition (blue arrows) while the one-photon transition (orange dashed arrow) is forbidden. (b) Example measured graphene-cladded cavity transmission with asymmetric Fano-like lineshapes (red dotted line) and significantly larger red-shift, compared to a control bare Si cavity sample with symmetric Lorentzian lineshapes (black dashed line). Both spectra are measured at 0.6 mW input power, and are centered to the intrinsic cavity resonances (λ_{cavity_0} = 1562.36 nm for graphene sample, and λ_{cavity_0} = 1557.72 nm for Si sample), measured at low power (less than 100 μW input power). The intrinsic cavity quality factor is similar between the graphene and the control samples.

5-2 Steady-state two-photon absorption induced thermal nonlinearities in graphene-silicon hybrid cavities: (a) Measured quasi-TE transmission spectra of a graphene-clad *L3* cavity with different input power levels (with extracted insertion loss from the facet of

waveguides in order to be comparable to simulation in b). (b) Nonlinear coupled-mode theory simulated transmission spectra. The estimated input powers are marked in the panels. (c) Measured cavity resonance shifts versus input power, with the graphene-clad cavity samples (in red) and the monolithic silicon control cavity sample (in blue). (d) Tuning efficiencies for graphene-clad cavity samples (in red) and control cavity samples (in blue) for a range of cavity loaded *Q*-factors examined.

5-3: Bistable switching in graphene-clad nanocavities. (a) Steady-state input/output optical bistability for the quasi-TE cavity mode with laser-cavity detuning δ at 1.5 (λ_{laser} = 1562.66 nm) and 1.7 (λ_{laser} = 1562.70 nm). The dashed black line is the coupled-mode theory simulation with effective nonlinear parameters of the graphene-silicon cavity sample.(b) Measured steady-state bistability at different detunings set at 0.18, 0.23, 0.26, 0.29 nm (from bottom to top). The plots are offset for clarity: green (offset 2 dB), brown (offset 8 dB) and red lines (offset 15 dB). (c) Normalized transmission of two cavities with resonance separation of δ=3. The grey dashed line is measured at -16dBm input power, and the solid black line is for 0dBm input. (d) The tranfer function for optical bistability in two cavity system as in (c). The laser detuning is set at δ=3 to the first cavity, and δ=1.5 to the second cavity (marked as dashed line in (c)).

5-4: Switching dynamics with triangular waveform drive input (a) The input waveform is dashed grey line. The bistable resonances are observed for both positive and negative detuning. Blue empty circles: δ(t=0) = -1.3(λ_{laser} = 1562.10 nm), red solid circles: δ(t=0) = 1.6 (λ_{laser} = 1562.68 nm). Inset: schematic of high- and low-state transmissions. (b) The ratio between the on off output intensities versus different

detunings. (c) The output switching dynamics with the input as in (a), at negative detunings. (d) positive detunings.

5-5: Regenerative oscillations in graphene-cladded nanocavities. (a) Observations of temporal regenerative oscillations in the cavity for optimized detuning (λ_{laser} = 1562.47 nm). The input power is quasi-triangular waveform with peak power 1.2 mW. The grey line is the reference output power, with the laser further detuned at 1.2 nm from cavity resonance (λ_{laser} =1563.56 nm). (b) Mapping the output power versus input power with slow up (blue cross) and down (red) power sweeps. In the up-sweep process, the cavity starts to oscillate when the input power is beyond 0.29 mW.(c) Measured regenerative oscillations at down-sweep, longer temporal basewidths and different detunings in graphene-silicon nanocavities. Output cavity transmission with slowly-varying (7-ms) input laser intensities. The cold cavity resonance is 1562.36 nm, and the laser wavelengths from top to bottom are fixed at 1562.51 nm, 1562.60 nm, and 1562.62 nm. The oscillation starts when the ascending power reaches 0.29, 0.66, and 0.75 mW. Reference outputs plotted as in solid lines.

5-6: Coupled mode theory calculated cavity resonance oscillation (a) Nonlinear coupled-mode theory model of cavity transmission versus resonance shift, in the regime of regenerative oscillations. With a detuning of 0.15 nm [δ(t=0) = 0.78] the free carrier density swings from 4.4 to 9.1×10^{17} per cm3 and the increased temperature ΔT circulates between 6.6 and 9.1K. (b) RF spectrum of output power at below (0.4 mW, grey dashed line) and above oscillation threshold (0.6 mW, blue solid line) at the same detuning $\delta_{(t=0)}$ = 0.78 (λ_{laser}-λ_{caviy} = 0.15 nm). Inset: Normalized transmission from model (blue line) and

experimental data at the same constant power level (red circles). (c) Cavity resonance shift due to different nonlinear dispersion versus time. (d) Thermal (red) and free carrier (blue) dispersion induced cavity resonance shift versus the energy circulating in cavity.(e) The total carrier resonance dispersion versus cavity.

5-7: Coupled-mode equations calculated time domain response to a step input with a graphene-clad silicon photonic crystal *L3* nanocavity side-coupled to a photonic crystal waveguide. (a) The output versus input powers for positive and negative detunings (laser-cavity detunings are set from -0.06 to 0.37 nm). Input laser power is set at 0.6 mW. The cavity switching dip is observed for all detunings, and regenerative oscillation exists only predominantly for positive detuning. (b) Frequency response of the cavity switching and oscillation dynamics with conditions as in a (in log scale). The laser detuning is set from -0.06 to 0.37 nm. (c) and (d) Oscillation period versus laser detunings and input powers respectively.

Figure 6-1: Figure 6-1: Structure and linear optical properties of the device (a) Silicon nitride device layout. Optical image of top view of the ring, where the dashed line shows the cleaved position for the SEM image. (b) Output spectrum of TE and TM polarized input with 0dBm input power. Inset: 650nm PECVD silicon nitride is sandwiched between the PECVD silicon oxide up cladding layer and the thermal oxide lower cladding layer. Scale bar: 1um. Inset (up right): Cross section and the optical profile of the TE mode. Inset (bottom left): SEM image of the ring-waveguide coupling part.

6-2. Wavelength dependent absorption and ring quality factor (a) Linear absorption

of the PECVD grown silicon nitride thin film, in the range of mid infrared and near infrared. (b) FTIR measured absorption versus phonon energy of PECVD silicon nitride thin film (black circles) and the absorption of a 25mm long SiN waveguide versus photon energy from tunable laser (green line). Wavelength dependent linear propagation loss near 1520nm. The absorption peak is at 0.815eV with FWHM of 0.03eV. (c) Normalized transmission of ring resonator of 70um radius (blue) and 6.7 mm long waveguide (black). Inset: transmission on resonance versus intracavity field transmission. The blue crosses are experimental data. Red solid line and blue dashed line are theoretical predictions for over-coupled and under-coupled region respectively. (d) Linear loss depdent total quality factors. Experimental results are directly derived from fitting the ring resonances in c, and theoretical predicts are given by Eq. 6-2.

6-3. Photon loss and thermal dispersion (a) The transmission spectrum with input power at 20uW for linear characterization. The red dash curve, green solid curve, and the blue dotted curve are CMT simulation results with linear absorption rate of 1/0.04ns, 1/0.4ns and 1/4ns. The cross is experimental data. (a) The transmission spectrum with input power at 156μW for linear characterization. The red dash curve, green solid curve, and the blue dotted curve are CMT simulation results with linear absorption rate of 1/0.04ns, 1/0.4ns and 1/4ns. The cross is experimental data (b) Optical transmission lineshape at different optical input power (0.02, 0.06, 0.13,0.20 and 0.26mW). The dashed curves are experimental data and the solid curves are coupled mode theory simulation. (c) Cavity resonance shift versus the input power at absorption peak (80pm/mW near 1520nm) and away of the absorption peak (20pm/mW near 1560nm) Inset: The Hysteresis loop of the output versus input power is measured for the resonance

near 1523nm with TE polarization. The laser-resonance detuning are set at 33 and 34pm for the blue and red lines respectively.

6-4 Thermal optical bistability near the molecular vibration peak (a) Output power of pump and probe versus input pump power. The pump detuning is 3.06 (red) to mode resonant at 1540.065nm and the probes are set at 2.81 (light blue), 2.87 (navy), and 2.93 (black) to the mode resonant at 1542.962nm (b) Time domain cavity response to the step function input. The laser intensity turns on at 0μs to 1mW. The laser-cavity detunings are -2pm (red) and 2pm (blue) respectively. The dots are experimental data and the lines are the exponential curve fitting. The lifetime is about 150 μs for both cases.

7-1: Photocurrent of DWELL and GaAs control cell of different sizes (2×2 mm^2, $3\times3mm^2$ and 5×5 mm^2) under AM 1.5G illumination. The inserted picture is the schematic diagram of the DWELL solar cell with six-stacks of InAs QDs embedded in InGaAs quantum wells.

7-2: A comparison of the dark behavior of GaAs control and DWELL cells for the same dimensions (2×2 mm^2 , 3×3 mm^2 and 5×5 mm^2). Measured and simulated local ideality factor (a), and the measured and simulated semi-logarithmic dark current density (b) for the control cells. Measured local ideality factor (c) and dark current density (d) for the DWELL cells. The simulation is based on Equation 1(a), where the parameters extracted by the curve fitting are illustrated in the modeling part. The inserted picture is a Silvaco simulation of the non-uniform current distribution in the device.

7-3: Normalized photoluminescence of four six stack DWELL samples. The dots are experimental data and the curves are two components Gaussian fitting for QW and QDs.

1, DWELL without InP strain concentration (SC) for small quantum dots size; 2, with SC; 3. larger quantum dots w/o SC, 4. Larger QDs with SC.

7-4: Wafer scale solar cell performance (6 stack DWELL cells with strain compensation) (a) Short circuit current (b) Open circuit voltage (c) Filling factor (d) Efficiency (%). Solar cells with three difference sizes are numbered in (d). B1-B5: 5 by 5 mm^2, M1-M9: 3 by 3 mm^2, S1-S11: 2 by 2 mm^2

7-5: The open circuit voltage versus the short circuit current for 6 stack DWELL cells with strain compensation (small dots and large dots), with three different solar cell sizes.

7-6: Device schematics and the IV characteristics (a) Bulk structure of solar cells with six-stacks of InAs QDs embedded in InGaAs quantum wells. The inserted picture is the top electroluminescence when the cell is forwardly biased. (b) Schematic band diagram is plotted according to x/z axis for DWELL (left) and Control (right). E_c, E_v, E_{fv} and E_d mark energy level of conduction, valance band, quasi hole Fermi level (under bias V~0.6V), and edge state. (c) Recombination reverse saturation current density for DWELL (left) and control cells (right).

7-7: Cross-wafer comparison (a) Measured I-V characteristics of 6-stack w/ and w/o SC, 13-stack DWELL and GaAs control cell under AM 1.5 global illumination. (b) Photocurrent versus reverse saturation current in dark for different samples.

7-8: External quantum efficiency measurement (a-c) Incremental absorption and (d-f) Photoluminescence of device and as-grown wafer (g-i) carrier transport efficiency versus

wavelength for three DWELL samples: 6 stack DWELL with/without SC, 13 stack with SC at room temperature. The lines mark the ground state of quantum well.

Acknowledgements

During the graduate study at Columbia University, I received rigorous scientific training in a corporative environment, including project planning, task delegation, time management, conference presentations and open lines of written and oral communication. I worked with research groups ranging from the fundamental material physics to the advanced interconnect architecture. Their ideas, experience and concerns corrected and stimulated my scientific exploring.

I would like to thank my advisor, Prof. Chee Wei Wong. He challenged me with cutting edge research projects and left me a lot of freedom on choosing pathways to accomplish the goals. I'd also like to thank Prof. Philip Kim, Prof. Tony Heinz, Prof. Richard Osgood, Prof. Tanya Zelevinski, Prof. Dirk Englund and Prof. Aron Pinzuck. Their clear lectures helped me to approach various physical concepts with my naïve engineer's curiosity. My labmates and seniors, Ying Li, Jinghui Yang, Xingsheng Luan, Serdar Kocaman, Xiaodong Yang, Jie Gao, Chalton Chen etc. spent many precious time together in the lab, sharing the experience and helping each other on the technical details. I want to acknowledge Nick Petrone from Prof. Jim Hone's group, for his pioneering work of growing high quality CVD graphene, lying as a magic cloth on my silicon devices. Yue Zhao and Andrea Young from Prof. Kim's group assisted me with Ebeam lithography. Dr.

Arend van der Zande and Dr. Alexander Gondarenko from Prof. Hone's group also involved me in many informative discussions. Joshua Lui, Yilei Li and Hugen Yan from Prof. Heinz group are also great scientists to work with.

I also appreciate Prof. Mark Feuer and Prof. Keren Bergman's classes on the optical devices and communication. The classes illuminated the functionality and demand for nanophotonic devices from an industrial perspective. Also, corporation work with Prof. Bergman's group members, including Kishore Padmaraju, Norm Ophir and Christine Chen, were also pleasant experience for me. Jerry Daddap and Prof. Richard Osgood constantly encouraged me at various stages of my research. Xuetao Gan, Hanna Clevenson and Xinwen Yao from Prof. Dirk Englund group are also active optical members I enjoyed discussion with.

Last but not least, I thank my father, who shared his passion on science and relentless entrepreneur spirit with me since my early age. Also thank my mother, companying me walk through the toughest years with her 339 emails.

To my parents

Chapter 1

Introduction

1.1 Background and motivation

The growth of data center internet and cloud computing demands for high data transfer speeds and 100G Hz bandwidths. The developing new technologies for matching this demand with relatively constant power have been increasing. The superior bandwidth and promising future of silicon photonics for interconnects have attracted investment and research effort from industries, including IBM Corp.[1-2], Oracle Corp. [3-4], Intel Corp. [5], Google Corp. [6], NTT Corp. [7], Alcatel-Lucent Bell Labs [8], Enablence Technologies Inc., Hewlett-Packard Co., Kotura Inc., Lightwire Inc., Luxtera Inc., PGT Photonics, a subsidiary of Pirelli & Co. SpA, Sun Microsystems Inc., Translucent Inc., a subsidiary of Silex Systems Ltd., and US Conec Ltd.

Low-power and low-cost photonic integration circuit is promising for enhancing the density, reaching distance, and data rates for next-generation datacenter networks. It also provides platform for new network architectures and applications. The fundamental understanding of the photonic properties of the nanostructure and materials promises continuous growing of the nanophotonic technology. The CMOS foundry infrastructure enables integration of high density, high performance optical transceivers based on the individual photonic elements [9]. A recent 90nm CMOS integrated nano-photonic technology (CINP) for 25Gbps wavelength division multiplexing optical communications has been demonstrated, including electro-optical converter (modulator), four channel WDM filter, 6dB optical coupler, and 11GHz integrated Ge receiver [10].

The high performance computation is under steady linear growth over the past decade. The

I/O bandwidth has always been the bottleneck for the high performance computing systems. Optical interconnects have to improve on the power, cost, density and reliability. In this thesis, I explored and compared the device performance enable by the nonlinear properties. Incorporating the Kerr nonlinearity, two-photon absorption, free charge carrier interactions and Raman effect in the low loss silicon photonics platform are important physical processes for all optical controlled modulators, switches and filters.

1.2 Photonic integrated circuits

Photonic integrated circuits (PICs) are important part of the optical transceivers, providing higher bandwidth for card-to-card, chip-to-chip interconnects. Silicon photonics transfer data in 40-120 Gbps, reaching the 10-2,000m range. High-density integrated silicon nanophotonic transceivers can be fabricated in CMOS foundry. CMOS photonics have realized the high speed modulator (400fJ/bit) based on silicon ring. Technique improvements include tuning out the resonance imperfections. Low energy target pushes the revolutionary involvement of interconnect technology from the electronics (100 fj/bit) to optics (10fj/bit). Optical interconnect is the bottleneck for the computation on chip.

Photonic crystal offers a platform to manipulate light in a sub-wavelength range, which not only shrinks the footprint of the elements, but also decreases the power dissipation. With "atom-scale" flexibility to modulate light, optical buffer can be realized in photonic crystal waveguide with 60 folds longer delay compared to channel waveguide [11], or photonic crystal based optical filters [7,12] with negligible loss or distortion [13]. Furthermore, compact modulator/switches can also be involved in the integrated photonic

circuit by using electrically controlled micro-cavity besides the waveguide [14]. PhC devices also can be engineered to have unique properties, such as negative refraction lenses [15-16], low loss harp waveguide bends, high *Q* small volume resonators for low power all optical controlled active devices. The small footprint of the photonic crystal elements also enables compact designs [17].

However, importance of PhC's role in the high performance chip scale PICs is hindered by non-conventional nanofabrication for the small structures. The surface roughness and structure distortion increase the linear loss in PhC waveguides. The large propagation loss in photonic crystal waveguide has been optimized to be comparable to channel waveguide as reported in ref [18]. Those small devices have advantage in the applications of modulators, non-blocking torus, and cascading photonic switches. As an example, the explicit performance comparison between the PhC and channel waveguide based switches in different topology system is presented in chapter two.

1.3 Network on a chip

Assuming the scalability is applicable for all the elements on chip, the delay and latency can be decreased to one tenth. For a 40 Gbits/s signal, a single bit is 25 ps or 2.5 mm long, only 4 bits could fit into one centimeter and suffer approximately 3dB loss. Obviously the technique is not ready for storing multiple packets with 100s of bits for each of them. The low optical storage of slow light could be solved by involving quantum information processing, which allows more information stored per bit [19]. The CMOS foundry infrastructure enables integration of high density, high performance optical transceivers.

They are the silicon-on-insulator (SOI) submicrometre processing.

Thermal and mechanical tuned devices usually cannot reach high speed (MHz). Comparatively speaking, local refractive index shift through carrier plasma effect, electrical injection, polarization control, second or third harmonic generation would be able to provide higher speed. The state-of-art optical signal processing on a silicon chip using slow light photonic crystal waveguide can reach up to 640 Gb/s through third harmonic generation [17]. Actively controllable slow light waveguide has been realized with bandwidth up to 100nm, 20dB extinction ratio, and FSR ranging from 0.01nm to 20nm. But large loss fluctuation (0.1 to 1dB over 10μm) also companies the large working bandwidth [11]. Nonlinear loss and signal distortion in slow light silicon photonic crystal waveguide, and the 10Gbit/s signal transmission (distorted) has been experimentally proved [18]. Femito-joule all-optical modulation energy, upto 40 Gbps modulation frequency and ultra-small size (0.025 μm^3) are realized in GaAs based photonic crystal cavities [19].

1.4 Graphene photonics

The unique linear and massless band structure of graphene, in a purely two-dimensional Dirac fermionic structure, have led to intense research spanning from condensed matter physics [20-24] to nanoscale device applications covering the electrical [25-26], thermal [27-28], mechanical [29] and optical [30-31] domains. In comparison with solely monolithic silicon cavities, the dramatically-large and ultrafast $\chi^{(3)}$ nonlinearities in graphene and the large *Q/V* ratios in wavelength-localized photonic crystal cavities enables all optical switching at femtojoule per bit energy level. These nonlinear results

demonstrate the feasibility and versatility of hybrid two-dimensional graphene-silicon nanophotonic devices for next-generation chip-scale high-speed optical communications, radio-frequency optoelectronics, and all-optical signal processing.

1.5 Thesis organization

This thesis is composed of seven chapters. The first two chapters cover the applications of the silicon based resonators for the Network on chip applications, including the comparison between channel waveguide based platform and photonic crystal platform. The chapter 3 introduces the design, fabrication of a two cavity system. The effective thermal-optical tuning enables precise the phase controlled cavity-cavity interference. The chapter 4-5 analyzed the third order nonlinearity and its related free carrier dynamics in graphene-silicon system. The Kerr nonlinearity leads to four-wave-mixing in the photonic crystal cavity, and the large two photon absorption induces optical bistability and regenerative oscillation under continuous wave excitation. Chapter 6 introduces the unique and complex properties of PECVD silicon nitride ring, involving IR light interaction with molecular vibration absorption and defects absorption in surround silicon nanocrystals. The steady state bistability and dynamic stochastic switching is experimentally explored and theoretically interpreted by the light interaction with the hydrogen bond and the silicon quantum dots. Chapter 7 focuses on the experiment and modeling of the InAs/InGaAs DWELL solar cells, showing the quantum dots layer's functionality on enhancing the solar cell efficiency in small scale. The last chapter wraps up the material explored in this thesis and discusses their contributions for energy effective modem communication systems.

Bibliography

[1] M. A. Taubenblatt, Optical interconnects for high-performance computing, *Journal of Lighwave Technology*, **30**, 448 (2012)

[2] Fuad E Doany, Benjamin G Lee, Alexander V Rylyakov, Daniel M Kuchta, Christopher Jahnes, Christian Baks, Frank Libsch, Clint L Schow, Terabit/sec 48-channel fiber-coupled optical module based on holey CMOS transceiver IC, *Electronic Components and Technology Conference (ECTC),* 2012 IEEE 62nd pp. 1499-1504

[3] C. Gunn, CMOS photonics for high-speed interconnects, *IEEE Micro*, 58-66 (2006)

[4] A. Krishnamoorthy, X. Zheng, G. Li, J. Yao, T. Pinguet, A. Mekis, H. Thacker, Exploiting CMOS manufacturing to reduce tuning requirements for resonant optical devices, *IEEE Photon. J* 3, no. 3 (2011): 567-579.

[5] H. H. Bazzaz, M. Tewari, G. Wang, G. Porter, T.S.E.Ng, D. G. Andersen, M. Kaminsky, M. A. Kozuch and A. Vahdat, Switching the optical divide: fundamental challenges for hybrid electrical/optical datacenter networks, In *Proceedings of the 2nd ACM Symposium on Cloud Computing*, p. 30. ACM (2011)

[6] H. Liu, C. F. Lam, and C. Johnson, Scaling optical interconnects in datacenter networks, *2010 18th IEEE Symposium on High Performance Interconnects*, **113** (2010)

[7] M. Notomi, A. Shinya, K. Nozaki, T. Tanabe, S. Matsuo, E. Kuramochi, T. Sato, H. Taniyama, and H. Sumikura, Low-power nanophotonic devices based on photonic crystals towards dense photonic network on chip, *Circuits, Devices & Systems, IET* **5**, 84-93 (2011)

[8] R. W. Tkach, Scaling optical communications for the next decade and beyond, *Bell Labs Technical Journal* 3-9 (2010)

[9] J. S. Orcutt, A. Khilo, C. W. Holzwarth, M. A. Popović, H. Li, J. Sun, T. Bonifield, Nanophotonic integration in state-of-the-art CMOS foundries, *Optics Express* **19** 2335-2346 (2011)

[10] Y. A. Vlasov, Silicon CMOS-integrated nano-photonics for computer and data communications beyond 100G, *Communications Magazine, IEEE* **50**, s67-s72 (2012)

[11] Y. A. Vlasov, M. O Boyle, H. F. Hamann and S. J. McNab, Active control of slow light on a chip with photonic crystal waveguides, Nature Letters, Vol. 438, pp. 65-69 (2005)

[12] X. Yang, M. Yu, D.-L. Kwong, and C.-W. Wong, All-Optical Analog to Electromagnetically Induced Transparency in Multiple Coupled Photonic Crystal Cavities, *Phys. Rev. Lett.* **102**, 173902 (2009)

[13] R. W. Boyd, D. J. Gauthier, Controlling the Velocity of Light Pulses, *Science* **326**, pp. 1074-1077 (2009)

[14] D. M. Beggs, T. P. White, L. O' Faolain and T. F. Krauss, Ultracompact and low-power optical switch based on silicon photonic crystals, *Optics Letters* **33**, pp. 147-149 (2007)

[15] R. Chatterjee, N. C. Panoiu, K. Liu, Z. Dios, M. Yu, M. T. Doan, L. J. Kaufman, R. M. Osgood, and C. W. Wong, Achieving subdiffraction imaging through bound surface states in negative refraction photonic crystals in the near-infrared range, *Phys. Rev. Lett.* **100**, 187401 (2008)

[16] S. Kocaman, M.S. Aras, P. Hsieh, J. F. McMillan, C. G. Biris, N. C. Panoiu, M. B. Yu, D. L. Kwong, A. Stein, and C. W. Wong, Zero phase delay in negative-index photonic crystal superlattices, *Nature Photonics* **5**, 499 (2011)

[17] T. F. Krauss, Slow light in photonic crystal waveguides, *J. Phys. D: Appl. Phys*. **40** 2666-2670 (2007)

[18] J. F. McMillan, M.Yu, D.-L. Kwong, and C. W. Wong, Observations of four-wave mixing in slow-light silicon photonic crystal waveguides, *Optics Express* **18**, 15484 (2010)

[19] C. A. Husko, A. de Rossi, S. Combrie, Q. V. Tran, F. Raineri, C. W. Wong, Ultrafast all-optical modulation in GaAs photonic crystal cavities, *Appl. Phys. Lett.* **94**, 021111 (2009)

[20] Y. Zhang, Y.-W. Tan, H. L. Stormer, and P. Kim, Experimental observation of the quantum Hall effect and Berry's phase in graphene, *Nature* **438**, 201-204 (2005)

[21] A. K. Geim and K. S. Novoselov, The rise of graphene, *Nature Materials* **6**, 183-191 (2007).

[22] X. Du, I. Skachko, F. Duerr, A. Luican, and E. Y. Andre, Fractional quantum Hall effect and insulating phase of Dirac electrons in graphene, *Nature* **462**, 192-195 (2009)

[23] C. R. Dean, A. F. Young, P. Cadden-Zimansky, L. Wang, H. Ren, K. Watanabe, T. Taniguchi, P. Kim, J. Hone, and K. L. Shepard, Multicomponent fractional quantum Hall effect in graphene, *Nature Phys.* **7**, 693-696 (2011)

[24] C.Berger, Z. Song, X. Li, X. Wu, N. Brown, C. Naud, D. Mayou, T. Li, J. Hass, A. N. Marchenkov, E. H. Conrad, P. N. First, W. A. de Heer, Electronic Confinement and Coherence in Patterned Epitaxial Graphene, *Science* **312**, 1191-1196 (2006)

[25] I. Meric, M. Y. Han, A. F. Young, B. Ozyilmaz, P. Kim and K. L. Shepard, Current saturation in zero-bandgap, top-gated graphene field-effect transistors, *Nature Nanotech.* **3**, 654-659 (2008)

[26] Y.-M. Lin, C. Dimitrakopoulos, K.A. Jenkins, D.B. Farmer, H. Grill and P. Avouris,

100-GHz transistors from wafer-scale epitaxial graphene, *Science* **327**, 662 (2010)

[27] J. H. Seol, I. Jo, A. L. Moore, L. Lindsay, Z. H. Aitken, M. T. Pettes, X. Li, Z. Yao, R. Huang, D. Broido, N. Mingo,R.S. Ruoff, L.Shi, Two-dimensional phonon transport in supported graphene, *Science* **328**, 213-216 (2010)

[28] N. M. Gabor, J. CW Song, Q. Ma, N. L. Nair, T. Taychatanapat, K. Watanabe, T.Taniguchi, L. S. Levitov, and P. Jarillo-Herrero, Hot carrier–assisted intrinsic photoresponse in graphene, *Science* **334**, 648-652 (2011).

[29] C. Lee, X. Wei, J. W. Kysar, and J. Hone, Measurement of the elastic properties and intrinsic strength of monolayer graphene, *Science* **321**, 385-388 (2008)

[30] F. Bonaccorso, Z. Sun, T. Hasan and A. C. Ferrari, Graphene photonics and optoelectronics, *Nature Photon.* **4**, 611-622 (2010)

[31] C.-F. Chen, H.-H. Part, B. W. Boudouris, J. Horng, B.Geng, C. Girit, A. Zettl, M. F. Crommie, R. A. Segalman, S. G. Louie and F. Wang, Controlling inelastic light scattering quantum pathways in graphene, *Nature* **471**, 617-620 (2011).

Chapter 2

Network-on-chip devices:

geometry & materials

2.1 Geometry: compare ring and photonic crystal based routers

Silicon ring resonators are building block for optical modulators, but their sharp resonances render them sensitive to temperature fluctuation and fabrication variance. And power dissipation is still an issue. Thus, compact integrated configurations with better thermal isolation are required [1].

For estimating the enhancement of performance by involving photonic crystal based delay line, PSEs, and switches, the original parameters for describing micro-ring based resonators would be replaced by the numbers (experimental) reported in the up-to-date literatures. Thus, a reliable comparison on system level performance between the two technologies (micro-ring [2] and photonic crystal) can be predicted by PhoenixSim [3]. Specifically, the PSE realized by photonic crystal direct coupler would be implanted in exist/exploring 4 by 4 non-blocking routers for seeking a superior advantage power saving [4-5]. The big issue for implanting photonic crystal switch is the loss when light propagates through the photonic crystal part. The signal is reflected from the channel waveguide and photonic crystal waveguide interface and degraded when propagates through the PhC waveguides. The interface reflection can be minimized by proper geometric design for mode matching, and the later one is confined by the surface roughness, geometric fluctuations and other non-ideal limitations in fabrication, but could be overcome by making use of Nonlinear effect in silicon (e.g. Raman scattering and Kerr nonlinearity), which can even amplify the signal.

2.1.1 Single switch analysis

A compact photonic crystal directional coupler with a similar layout in a silicon on insulator platform electro-optically switched at 150kHz with a switching time of 620ns under a low voltage operation of 2.9 V. Table1 compares the physical parameters between photonic crystal direct couplers and ring cross couplers [2, 6]. The connection length and propagation delay were left untouched considering the fact that the thermal isolation range should be same for both ring based or PhC based coupler when implanted in photonic circuits.

Table 2-1: Simulation parameters for the Silicon switches

	Photonic crystal direct coupler		**ring resonator**
	Aggressive	Realistic	Realistic
Propagation loss	2 dB/cm		2 dB/cm
Insertion loss (Bar)	0.1dB	2 dB	0.005 dB
Insertion loss (Crs)	0.1dB	2 dB	0.5 dB
Bar port ER	20 dB		25 dB
Bar delay	0.105ps		1.25ps
Cross port ER	12 dB		20 dB
Crossing delay	0.105ps		4.35ps
dn	4.2×10^{-3}		1×10^{-2}
Heat capacity	8 pJ/degree		1 μJ/s/degree
dT	23 K		20 K
Latency	0.01 ps		0.06 ps
Footprint	9×9 μm^2		50×50 μm^2
Bandwidth	100 GHz		38.5 GHz
extinction ratio	30 dB		20.79 dB
Switching length	5.2 um [2]		30 um

To make a compact and lossless modulator or switch, careful and descent geometric design is essential, not only for enhancing the light localization through nonlinear effect [7], but

also for suppressing loss (propagation, coupling, insertion) by trimming the mode (light profile on the cross section) to match the one in channel waveguides.

2.1.2 Router analysis

The major source of loss in ring resonator comes from the energy dissipation in ring when the data flow needs to change direction in the switch. Assume other losses are negligible (<0.05dB), the pass-through-ring loss (0.5 dB) is analyzed as below.

Different from ring resonator, photonic crystal switch does not have “preference” on pass through “ring” or pass by “ring”. As long as the signal meets the switch, 2dB loss is sacrificed wherever direction it comes out. The first two work more like circulator, which leads to high insertion loss and latency, while the final one prefers going straight through.

2.1.3 Blocking

However, for achieving the non-blocking functionality, the simplicity of the design is sacrificed, which means more switches and lines are involved to make sure the switch can work with all the parallel inputs. An optimized systematical design calls for leveraged functionality and simplicity, where blocking switches with matched preference as the systems are used because of their low cost, loss, latency, and energy dissipation. As an example, simple 4 × 4 blocking switches are set up for loss analysis. The working status is listed as table 1.

When all the switches are on, the data flowing in the clockwise is nonblocking and enjoys low loss, while the anti-crossing data flow is activated when the four switches are off. The

direct transmissions are always on for both conditions. Again, the loss table is based on the photonic crystal directional coupler.

2.1.4 Implantation in Torus network topology

For estimating the potential of MEMS based devices, the ring resonator and PhC based switches are put in 8 by 8 topologies for compare. Torus NX and Nonblocking Torus are selected as testing samples.

The latency and throughput are same between two kinds of switches, because circuit switches are considered as working function for the switches here, so these two parameters, determined by clock rate, are same for both cases.

The insertion loss for the systematical simulation is very sensitive to the individual insertion loss in single switches. Without any optimization, the large insertion loss (2dB) caused by mode mismatch between the channel waveguide and photonic crystal waveguide leads to intolerable (600 dB) loss. If the insertion loss for individual photonic crystal switch can decreased to 0.1 dB, the result is comparable to the ring resonator as shown in Figure 8. By using the same parameters, the insertion loss in Torus NX is much lower than Nonblocking Torus.

The main difference between two kinds of switches, in terms of insertion loss, is that the photonic crystal direction coupler has the same loss for bar state and cross state, while the ring resonator has much lower loss when it is working at bar state.

2.2 Materials: graphene hybrid optoelectronic devices

Crystalline and Polycrystalline silicon, silicon nitride, Germanium are involved in the Photonic network-on-Chip Architectures for their easy compatibility with the CMOS processing. The basic functionalities, including the waveguide crossing, switch, modulator and photodetectors are realized and carefully engineered for high complexity topologies [8]. However, the indirect bandgap makes the silicon low tunability, but involving innovative metamaterials potential to decrease the complexity and standard of the silicon geometry for tailoring the EM field [9]. Graphene is an outstanding candidate for its versatile tunability, superior performance and easy integration with silicon system [10].

Generally, graphene has demonstrated its capability for the wide band operation. Graphene maintains optical transparency window from 1033nm to 2480nm, across C and L bands [11]. Graphene based device can operate at broad optical bandwidth, high speed, easy integration, and low power. Its weakness includes dependence on fabrication process, low responsivity, and sensitive to environment change. Here I list the graphene based device performance for switch, modulator and detectors.

2.2.1 One photon absorption saturation for mode locked lasers

The Pauli blocking makes graphene an ideal broadband absorber. The ultrafast carrier dynamics allows the ~ps recovery time for Graphene Saturable absorber (GSA). The increasing number of layers would decrease the modulation depth and increases the saturable intensity, and thus single layer graphene is prefered. Here is the Cross absorption modulation in graphene-waveguide system.

Table 2-2: Parameters for waveguide integrated Saturable absorber

Wavelength	Graphene Layers	Saturable intensity	Pump power*	Modulation depth	Recovery time	Ref.
1460-1650 nm	2	2 MW/cm^2	2 mW	66.5%	1.67 ps	[12]
1525-1570 nm	1	8.0-7.8 MW/cm^2	8-7.8 mW	12.77%	<10 ps	[13]
2014 nm	1	0.15 MW/cm^2	0.15 mW	94%	882 fs	[14]

*Pump power: product of the saturable intensity and the waveguide mode area

2.2.2 Absorption induced dynamical switching

A. Two photon absorption in waveguide

Two photon absorption in silicon leads to ultrafast all-optical switching in silicon wire waveguide [15]. The 70% modulation depth is demonstrated, with 13ps recovery time. The average pump power coupled into the waveguide is about 6mW (1.9W peak power). The two photon absorption rate is 10^5 times higher in graphene, and expected to lower the pump power 20 times in the hybrid structure. The high surface recombination rate in graphene would shrink the free carrier recovery time to ~ps as well [16].

B. Free carrier absorption in cavity

Figure 2 compares cavity-based switching and modulation across different platforms including silicon, III-V and the hybrid graphene- silicon cavities examined in this work. The thermal or free-carrier plasma-based switching energy is given by$P_{0th/e} \times \tau_{th/e}$, where $P_{0th/e}$is the threshold laser power required to shift the cavity resonance half-width through thermal or free-carrier dispersion; $\tau_{th/e}$ are the thermal and free-carrier lifetimes in resonator. Note that the lifetime should be replaced by cavity photon lifetime if the latter is

larger (for high *Q* cavity). Graphene brings about a lower switching energy due to strong two-photon absorption (~3,000 cm/GW) [17]. The recovery times of thermal switching (in red) are also shortened due to higher thermal conductivity in graphene, which is measured for supported graphene monolayers at 600 W/mK [18] and bounded only by the graphene-contact interface and strong interface phonon scattering.

2.2.3 Waveguide based Graphene modulator by electrical-optic control

Table III shows the experimentally demonstrated waveguide integrated graphene modulators. Single and double layer graphene is transferred onto channel waveguide, controlled by external gating. The transmission power decreases ~2dB and 4dB as the gate voltage moves the Fermi level away from the Dirac point, for single layer and double layer graphene devices.

Table 2-3: Parameters for waveguide integrated graphene modulator

Wavelength	Layers	Footprint	Modulation depth	Drive Voltage	Bandwidth	Ref.
1350-1600 nm	1	25 μm	0.09 dB/μm	3V	1 GHz	[27]
1350-1600 nm	2	40 μm	0.16 dB/μm	5V	1 GHz	[28]

2.2.4 High speed graphene photodetector

The generation and transport of photocarriers in graphene differ fundamentally from semiconductors. It allows high bandwidth, zero source-drain bias and dark current operation. Graphene based photodetector is demonstrated for the high bandwidth operation (40GHz verified, 500GHz aggressive), but the photoresponsivity is only 0.5mA/W with 80V gate bias [29], with non-optimized design. With improved electrodes design, the

photo-responsivity can be improved to 6.1mA/W at telecommunication wavelength, with 16GHz bandwidth (10Gbit/s) [30]. Enhancement of one dimensional resonators can increase the responsivity to 21mA/W at 850nm wavelength, with on-chip integration [31-32].

The photo-excited ultrafast dynamics is also investigated experimentally. The photocurrent response time is measured to be 1.5ps at room temperature [33]. The response time is 4.9ps and 2.9ps for exfloid and CVD single layer graphene, with mobility estimated to be 1,000 and 600 $cm^2/V/s$ respectively. With the gate tunable MGM design, the responsivity is 3mA/W at room temperature, for both fs pulse excitation and CW laser excitation. The responsivity can increase upto 32mA/W at temperature 20K for CW light [34]. More recently, 0.11A/W responsibility at room temperature is shown by graphene contact with p doped silicon [35]. On chip integrated design with silicon waveguide structure allows high speed, high responsivity and broadband OE conversion from visible to Mid IR range [36-38].

2.3 Conclusion

Resonators and waveguides are building blocks of the Network-on-chip system. The geometric design for waveguides and resonators determines the linear properties of the system, such as propagation loss, insertion loss, etc. The bandwidth and power of the optoelectronic devices, including modulators, detectors, switches, are limited by the materials. Given the thermal conductivity, electrical conductivity and optical transparency, graphene could be integrated in the silicon photonics for the active devices.

Bibliography

[1] Miller, D. A. Device requirements for optical interconnects to silicon chips. Proc. IEEE 97, 1166–1185 (2009)

[2] N. Sherwood-Droz, H. Wang, L. Chen, L Chen, B. G. Lee, A. Biberman, K. Bergman, M. Lipson, Optical 4 by 4 hitless silicon router for optical Networks-on-Chip, *Optics Express* **16**, 15915-15922 (2008)

[3] G. Hendry and J. Chan, Photonic and Electronic network Integration and Execution Simulator (PhoenixSim) 1.0 User manual

[4] L. Frandsen, A. Harpeth, P. Borel, M. Kristensen, J. Jensen, and O. Sigmund, Broadband photonic crystal waveguide 60 bend obtained utilizing topology optimization, *Opt. Express* **12**, 5916-5921 (2004)

[5] Camargo, Edilson A., Harold MH Chong, and Richard M. De La Rue, Highly compact asymmetric Mach-Zehnder device based on channel guides in a two-dimensional photonic crystal, *Applied optics* **45**, 6507-6510 (2006)

[6] M. J. Zablocki, A. Sharkawy, O. Ebil, S. Shi, and D. Prather, Electro-optically switched compact coupled photonic crystal waveguide directional coupler, App. Phys. Lett. 96, 081110 (2010)

[7] C. A. Husko, A. de Rossi, S. Combrie, Q. V. Tran, F. Raineri, C. W. Wong, Ultrafast all-optical modulation in GaAs photonic crystal cavities, *Appl. Phys. Lett.* **94**, 021111

(2009)

[8] A. Biberman, K. Preston, G. Hendry, N. Sherwood-Droz, J. Chan, J. S. Levy, M. Lipson, and K. Bergman, Photonic network-on-chip architectures using multilayer deposited silicon materials for high-performance chip multiprocessors, *ACM Journal on Emerging Technologies in Computing Systems (JETC)* **7**, 7 (2011)

[9] Vakil, Ashkan, and Nader Engheta. "Transformation optics using graphene." *Science* 332, 1291-1294 (2011)

[10] K. Kim, J.-Y. Choi, T. Kim, S.-H. Cho and H.-J. Chung, A role for graphene in silicon-based semiconductor devices, *Nature* **479**, 338-344 (2011)

[11] Mak, Kin Fai, Matthew Y. Sfeir, Yang Wu, Chun Hung Lui, James A. Misewich, and Tony F. Heinz. "Measurement of the optical conductivity of graphene." *Physical review letters* **101**, 196405 (2008)

[12] Bao, Qiaoliang, Han Zhang, Yu Wang, Zhenhua Ni, Yongli Yan, Ze Xiang Shen, Kian Ping Loh, and Ding Yuan Tang. "Atomic- Layer Graphene as a Saturable Absorber for Ultrafast Pulsed Lasers." *Advanced Functional Materials* **19**, 3077-3083 (2009)

[13] Zheng, Zhiwei, Chujun Zhao, Shunbin Lu, Yu Chen, Ying Li, Han Zhang, and Shuangchun Wen, Microwave and optical saturable absorption in graphene, *Optics Express* **20**, 23201-23214 (2012).

[14] G. Q. Xie, J. Ma, P. Lv, W. L. Gao, P. Yuan, L. J. Qian, H. H. Yu, H. J. Zhang, J. Y.

Wang, and D. Y. Tang, Graphene saturable absorber for Q-switching and mode locking at 2 μm wavelength, *Optical Materials Express* **2**, 878-883 (2012)

[15] T. K. Liang, L. R. Nunes, T. Sakamoto, K. Sasagawa, T. Kawanishi, M. Tsuchiya, G. R. A. Priem, D. Van Thourhout, P. Dumon, R. Baets an H, K. Tsang, Ultrafast all-optical switching by cross-absorption modulation in silicon wire waveguides, *Opt. Express* **13**, 7298-7303 (2005).

[16] T. Gu, N. Petrone, J. F. McMillan, A. van der Zande, M. Yu, G.-Q. Lo, D.-L. Kwong, J. Hone and C. W. Wong, Regenerative oscillation and four-wave mixing in graphene optoelectronics, *Nature Photonics* **6**, 554-559 (2012).

[17] H. Yang, X. Feng, Q. Wang, H. Huang, W. Chen, A. T. S. Wee, and W. Ji, Giant two-photon absorption in bilayer graphene, *Nano Lett.* **11**, 2622 (2011)

[18] J. H. Seol, I. Jo, A. L. Moore, L. Lindsay, Z. H. Aitken, M. T. Pettes, X. Li, Z. Yao, R. Huang, D. Broido, N. Mingo, R. S. Ruoff, and L. Shi, Two-dimensional phonon transport in supported graphene, *Science* **328**, 213 (2010)

[19] T. Tanabe, M. Notomi, S. Mitsugi, A. Shinya, and E. Kuramochi, Fast bistable all-optical switch and memory on a silicon photonic crystal on-chip, *Opti. Lett.* **30**, 2575 (2005)

[20] M. Notomi, A. Shinya, S. Mitsugi, G. Kira, E. Kuramochi, and T. Tanabe, Optical bistable switching action of Si high-*Q* photonic-crystal nanocavities, *Opt. Express* **13**, 2678 (2005)

[21] L.-D. Haret, T. Tanabe, E. Kuramochi, and M. Notomi, Extremely low power optical bistability in silicon demonstrated using 1D photonic crystal nanocavity, *Optics Express* **17**, pp. 21108 (2009)

[22] K. Nozaki, T. Tanabe, A. Shinya, S. Matsuo, T. Sato, H. Taniyama, and M. Notomi, Sub-femtojoule all-optical switching using a photonic crystal nanocavity, *Nature Photon.* **4**, 477 (2010)

[23] C. Husko, A. De Rossi, S. Combrié, Q. V. Tran, F. Raineri, and C. W. Wong, Ultrafast all-optical modulation in GaAs photonic crystal cavities, *Appl. Phys. Lett.* **94**, 021111 (2009)

[24] S. Kocaman, X. Yang, J. F. McMillan, M. B. Yu, D. L. Kwong, and C. W. Wong, Observations of temporal group delays in slow-light multiple coupled photonic crystal cavities, *Appl. Phys. Lett.* **96**, 221111 (2010)

[25] V. R. Almeida and M. Lipson, Optical bistability on a silicon chip, *Opt. Lett.* **29** 2387 (2004)

[26] Q. Xu and M. Lipson, Carrier-induced optical bistability in silicon ring resonators, *Opt. Lett.* **31**, 341 (2006)

[27] M. Liu, X. Yin, E. Ulin-Avila, B. Geng, T. Zentgraf, L. Ju, F. Wang and X. Zhang, A graphene-based broadband optical modulator, *Nature* **474**, 64-67 (2011)

[28] M. Liu, X. Yin, and X. Zhang, Double-layer graphene optical modulator, *Nano letters*

12, 1482-1485 (2012).

[29] F. Xia, T. Mueller, Y.-M. Lin, A. Valdes-Garcia and P. Avouris, Ultrafast graphene photodetector, *Nature nanotechnology* **4**, 839-843 (2009)

[30] T. Mueller, F. Xia and P. Avouris, Graphene photodetectors for high-speed optical communications, *Nature Photonics* **4**, no. 5 (2010): 297-301.

[31] M. Furchi, A. Urich, A. Pospischil, G. Lilley, K. Unterrainer, H. Detz, P. Klang, A. M. Anrews, W.Schrenk, G. Strasser and T. Mueller, Microcavity-integrated graphene photodetector, *Nano letters* **12**, 2773-2777 (2006).

[32] M. Engel, M. Steiner, A. Lombardo, A. C.Ferrari, H. v. Lohneysen, P. Avouris, and R. Krupke, Light–matter interaction in a microcavity-controlled graphene transistor, *Nature Communications* **3**, 906 (2012).

[33] D. Sun, G. Aivazian, A. M. Jones, J. S. Ross, W. Yao, D. Cobden, and X. Xu. Ultrafast hot-carrier-dominated photocurrent in graphene, *Nature Nanotechnology* **7**, 114-118 (2012).

[34] C.-H. Liu, N. M. Dissanayake, S. Lee, K. Lee, and Z. Zhong, Evidence for Extraction of Photoexcited Hot Carriers from Graphene, *ACS nano* **6**, 7172-7176 (2012).

[35] A. Yanbin, A. Behnam, E. Pop, and A. Ural, Metal-semiconductor-metal photodetectors based on graphene/p-type silicon Schottky junctions, *Applied Physics Letters* **102**, 013110-013110 (2013)

[36] X. Gan, R.-J. Shiue, Y. Gao, I. Meric, T. F. Heinz, K. Shepard, J. Hone, S. Assefa, and D. Englund, Chip-integrated ultrafast graphene photodetector with high responsivity, *Nature Photonics* **7**, 883-887 (2013)

[37] X. Wang, Z. Cheng, K. Xu, H. K. Tsang, and J.-B. Xu, High-responsivity graphene/silicon-heterostructure waveguide photodetectors **7**, 888–891(2013)

[38] A. Pospischil, M. Humer, M. M. Furchi, D. Bachmann, R. Guider, T. Fromherz and T. Mueller, CMOS-compatible graphene photodetector covering all optical communication bands. *Nature Photonics* ***7***, 892-896 (2013)

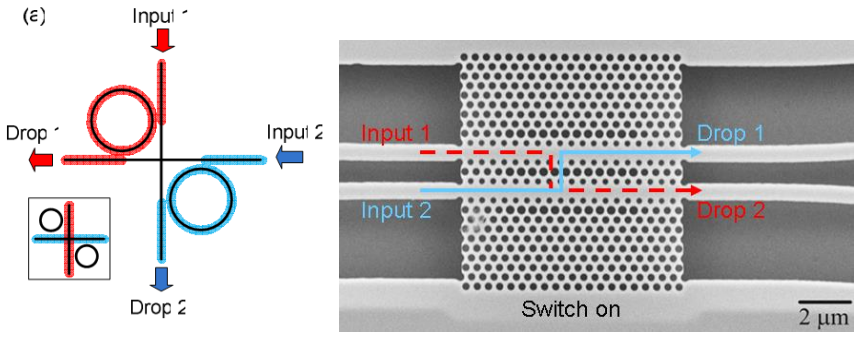

Figure 2-1. Basic 2 × 2 photonic switch element (left) ring resonator based (right) Photonic crystal directional coupler [3]

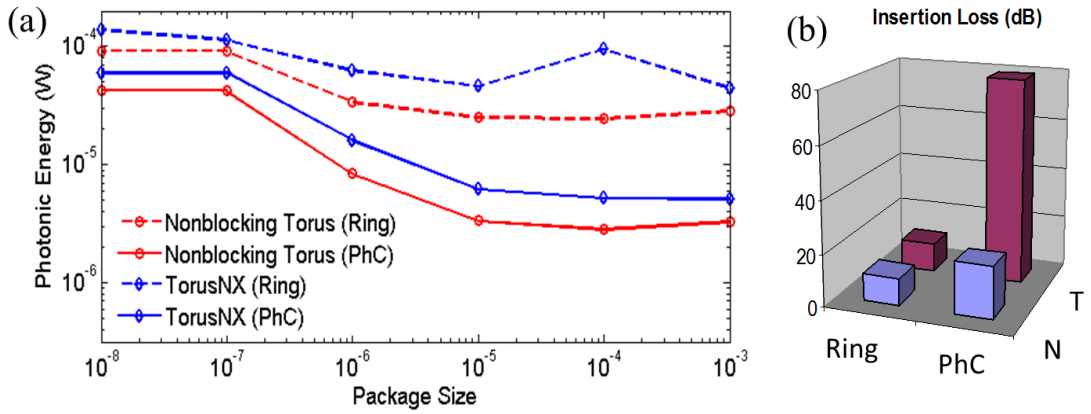

Figure 2-2. Compare the performance of nanophotonic networks based on ring resonator and Photonic Crystal （PhC) based switches by using different network topologies. (a) Photonic Energy versus Packet size. The red lines represent nonblocking torus, and the blue lines are for the torusNX ones. (b) Worst loss for ring (1) and PhC (2) based networks. The blue and purple bars are for Nonblocking Torus (N) and Torus NX (T) respectively.

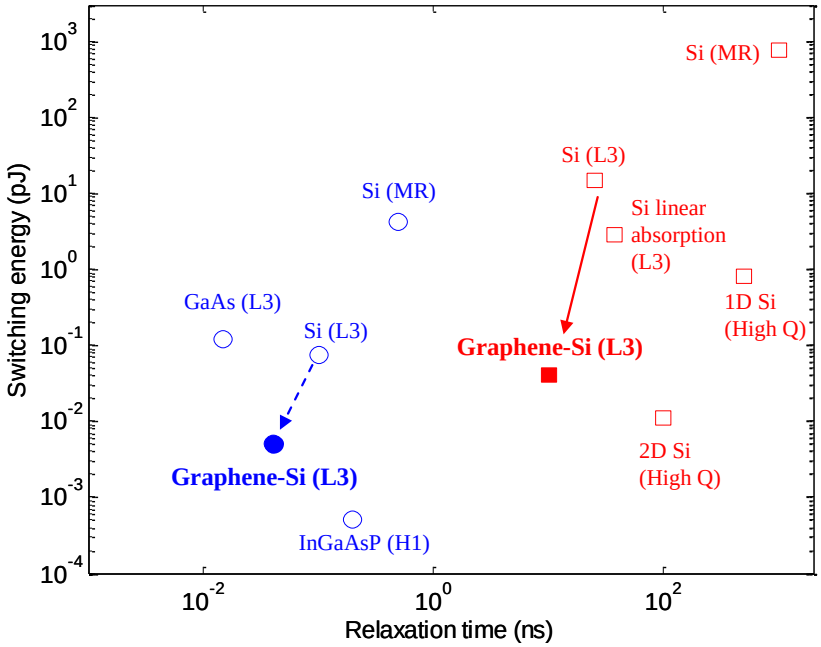

Figure 2-3 Comparison of switching energy versus recovery time of cavity-based modulators and switches across different semiconductor material platforms. The blue circles are carrier plasma-induced switches with negative detuning, and the red squares are thermal-optic switches with positive detuning. The dashed lines illustrate the operating switch energies versus recovery times, for the same material [19-26]. *L3* (*H1*) denotes photonic crystal *L3* (*H1*) cavity; *MR* denotes microring resonator.

Chapter 3

Deterministic tuning of inter-cavity coupling with integrated electrodes

3.1 Introduction

Based on analogies between classical electromagnetic fields and quantum probability amplitudes in atomic physics, electromagnetically induced transparence (EIT) and its photonic correspondence have been examined in atomic three-level canonical systems [1-2], atom – optical cavity systems [3], and chip-scale coupled photonic resonators such as indirectly coupled whispering gallery resonators [4-5] and photonic crystal cavities [6-7]. In its optical analogue, the interferences of the electromagnetic wave between excitation pathways to the upper level in three-level realization has led to highly-dispersive absorption cancellation of the medium [3], resulting in phenomena such as stopping and dynamical storage of light [8-9]. All optical analogue electromagnetically-induced-transparency (EIT) gives rise to strong interest due to its capability of controlling the qubit storage on chip at room temperature. The photon can be stored coherently between cavities much longer than in single cavity [10-12]. Previously the interference between the two discrete states are profoundly studied in the discretely coupled system [13], but the Autler-Townes splitting results from Rabi oscillation is only observable in well controlled system [8]. Here we use electron-beam defined microheater to locally adjust the refractive index. It is demonstrated that the thermal tuning effect is negligible when the cavity to heater distance is longer than 5 micrometers. The system parameters, including the cavity and phase are well-isolated for external control.

Here the observations of deterministic resonance and phase tuning of multiple photonic crystal cavities with precisely-positioned chip-scale integrated electrodes are presented, followed by the realization of an all-optical solid-state analogue to EIT on-chip. The

optical EIT-like lineshape has a comparable bandwidth-delay product to the atomic systems, although it has a significantly larger bandwidth and a correspondingly shorter delay [8]. To achieve the coherent interferences on-chip, the detuning and phase mismatch between the optical transitions or oscillators must be tightly controlled; to overcome the resonance variations between multiple cavities on-chip [14], tuning schemes involving for example optical [15] or electrically carrier injection [16], atomic layer deposition [17], integrated piezoelectric [18] and thermal heating [19] have been examined. Efficient carrier injection through Drude plasma dispersion has enabled for example fast CMOS-compatible optoelectronic modulators with appreciable extinction ratios and small drive voltage requirements [20]. These integrated approaches pave a scalable approach for chip-scale tuning, such as to simplify the resonance alignments of multiple cavities [21] in variable delay lines, controllable light-matter interactions in slow light photonic crystal waveguides [22], and high-speed efficient optical interconnects and transceivers on-chip [23].

3.2 Control optical pathways for cavity-cavity interaction

Cavity-atom or cavity-quantum dot interaction has been an important building block for the quantum information technology [24]. Controlling the spontaneous emission and stimulated emission of single photon has been demonstrated in the quantum dot-cavity system [25-26]. Meanwhile, the classic optics in the cavity-cavity interaction is also well studied by the coupled mode theory [26-27]. Here we demonstrate the intercavity phase can also be used to control the reflectivity of single cavities [28], for gaining classical insight of the cavity QED.

By placing a two state system in an external field, the coupling between spin and magnetic field, or the coupling between electric field and dipole would lead to rabi splitting of ω_R. Coupled differential equation for a two state system can be expressed in a dressed state form:

$$\frac{db_1}{dt} + \frac{i\delta}{2} b_1 = \frac{i}{2} \omega_R b_2 \tag{1a}$$

$$\frac{db_2}{dt} - \frac{i\delta}{2} b_2 = \frac{i}{2} \omega_R b_1 \tag{1b}$$

where b_1 and b_2 are probability amplitude of dressed states. δ is the detuning between two states. This model is based on two strongly coupled states with negligible spontaneous decay. Rewrite the expression in term of Hamiltonian:

$$H = H_0 + H_1 = \frac{1}{2} \begin{pmatrix} \delta & \omega_R \\ \omega_R & -\delta \end{pmatrix} \tag{2}$$

However, in the latter discussion, the strong interaction field is hard to achieve due to the photon loss through various channels (radiative or nonradiative recombination), and thus finite lifetime is introduced in further cases. Quantum dot is a two state emitter. When it is placed in a strong field resonant with its transition wavelength, the quantum dot interacts with the field.

Fig. 3-1a shows the quantum node unit composed of an atom and cavity. The externally controlling and related quantum transmission process is illustrated in Fig. 3-1b. Under the external light excitation, the total Hamiltonian for describing the atom-cavity system is:

$$H = H_{Atom} + H_{Field} + H_{Inter} = \begin{pmatrix} < e,n \mid H \mid e,n > & < e,n \mid H \mid e,n+1 > \\ < e,n+1 \mid H \mid e,n > & < e,n+1 \mid H \mid e,n+1 > \end{pmatrix} \quad (3)$$

Where the Atom's term $H_{Atom}=1/2h\omega\sigma_z$, $H_{Field}=h\nu(a^{+}a+1/2)$, and the interaction term is expressed as $H_{inter}=h(g^{*}\sigma_{-}a^{+}+g\sigma_{+}a)$. The critical parameter g is proportional to the local photon density of states ($D(k)$). The local field density is enhances as the cavity quality factor versus cavity mode volume:

$$V = \frac{\int n^2(r) \mid E \mid^2 dr^3}{n^2(r)_{\max} \mid E \mid^2_{\max}} \quad (4)$$

Fig. 3-1(d) shows the calculated photocounting rate of the cavity and the atom spontaneous emission of the cavity (generated by Quantum Optics Toolbox, from Sze Meng Tan [29]). Consider a quantum dot coupled to a nanocavity with a Rabi frequency $g/2\pi$= 10 GHz, suppose that its spontaneous emission rate $\gamma/2\pi$= 1 GHz, and that the cavity field decay rate is $\kappa/2\pi$ = 10 GHz, equal to the Rabi frequency.

3.2.1 Autler-Towns splitting in classic cavity-cavity system

Two coupled cavities (Fig. 3-2a) only evolve classical interaction. The relative phase between two cavities determines the cavity-cavity interaction. Take the two cavities (usually have different resonant wavelength, and detuned in the scale of the cavity linewidth) as two excited states sharing the same ground state:

$$\frac{da_1}{dt} = \left(i(\omega_{01} - \omega) - \frac{1}{2\tau} \right) a_1 + \frac{1}{2\tau} e^{i(-\beta L)} a_2 + \sqrt{\frac{1}{2\tau}} s_{1+} \quad (5a)$$

$$\frac{da_2}{dt} = \left(i(\omega_{02} - \omega) - \frac{1}{2\tau} \right) a_2 + \frac{1}{2\tau} e^{i(-\beta L)} a_1 + \sqrt{\frac{1}{2\tau}} e^{i(-\beta L)} s_{1+} \qquad (5b)$$

Where a_1 and a_2 are light amplitude in two cavities. For simplicity, I assume other loss channels, including the out-of-plan radiation and nonlinear absorption, are negligibly small compared to the coupling loss to the waveguide. The loss rate is inversely proportional to photon lifetime in cavity: $\gamma = 1/\tau$. ω_{01} and ω_{02} represent the cavity resonant frequencies. ω is the frequency of input laser. β is the propagation constant in waveguide and L is the distance between two cavities. The phase of the light changes βL after traveling from one cavity to another one. Neglect the external power supply term ($s_{1+} = sqrt(P_{in})$) and set the input laser right in the middle of two cavity resonances, the 'Hamiltonian' for the two cavities can be expresses as:

$$H = \frac{1}{2} \begin{pmatrix} \delta + i/\tau & ie^{-i\beta L}/\tau \\ ie^{-i\beta L}/\tau & -\delta + i/\tau \end{pmatrix} \qquad (6)$$

Compare to equation 1 for classical two state system, the rabi-frequency has the correspondent expression $\omega_R = i\gamma e^{-i\beta L}$. The detuning δ is defined as $|\omega_{01} - \omega_{02}|$. The rabi oscillation is an complex number here, whose real and imaginary parts depend on the phase term. The real part represents the cavity-cavity splitting and the imaginary part is from the photon cancellation during the cavity-cavity interference.

The cavity-cavity coupling can be controlled by the detuning between two cavities and the phase of waveguide linking the two cavities. In experiment, the cavities are resonant at optical communication band, ~1550nm wavelength. The in-plane cavity quality factor is

usually designed to be ~6000, correspondent to the cavity lifetime of $\tau=1/\gamma=Q/\omega_0=Q\lambda_0/(2\pi c)$=4.7ps. The cavity-cavity distance L is in the order of tens of μm, for separately controlling the cavity resonance and phase by external sources. Usually the detuning between two cavities is set below $(\omega_{02} - \omega_{01})\tau < 3.5$ for achieving strong interference.

In order to achieve the Electromagnetically induced transparency (shown in Fig. 3-2b), a little offset (or by cavity-cavity splitting) is required to observe the interference peak between two cavity resonance on the transmission spectrum. And the cavity-cavity phase (βL) is $\pi/2$ in order to form the destructive interference. Superluminescence (Fig. 3-2c) happens when the cavities are coherently radiate with the same phase. Constructive interference is required for the Superluminescnence as the βL is tuned to be zero. The supermode is formed between the two cavities and the waveguide linking them. We compare the optical field distribution in time domain by FDTD simulation (Fig. 3-3a), and the frequency domain cavity energy distribution by CMT (Fi.g 3-3b). In Superluminescence, the optical field distribution of the eigen mode is symmetric between the two cavities are symmetric at any time spot (Fig. 3-3a(i)), while the optical energy exchanges between the two cavities in EIT (Fig. 3-3a(ii)). In time domain, the energy dissipation doubles in the superluminescence and EIT can slow the light down. The splitting between two cavities should have the form of effective rabi splitting:

$$\omega_R' = \sqrt{\omega_R^2 + \delta^2} = \sqrt{(\sin(\beta L)/\tau)^2 + \delta^2} \quad (7)$$

The detuning is expected to be smallest as sin term is zero, and reaches its maximum (

$\sqrt{(1/\tau)^2+\delta^2}$) at $\beta L=\pi/2$.

Similarities between two models have been presented and compared, whether two distant coupled cavities can achieve Rabi oscillation stay controversial for a while. Sato et al. have demonstrated strong coupling between two distant coupled photonic crystal cavities separated by more than 100 wavelength [8]. Two cavities with 1 million quality factor are employed here. The cavity bandwidth is 1.5pm, with photon decay time $\tau=1/\gamma=Q/\omega_0=Q\lambda_0/(2\pi c)$=0.78 ns, so light can be reflected back and forth between two cavities through ~150 μm long waveguide without significant decay. The researchers experimentally obtained a Rabi splitting of 150pm on spectrum and periodic oscillation with a period of 54ps. The ~100μm separation between two cavities allows independent tuning one of the cavities. By introducing a short control pulse to shift the resonance of the two cavities, the oscillation stops.

Light oscillation between direct coupled cavities (two cavities separated by less than one wavelength in space) seems as ideal objective to study Jaynes-Cummings oscillation [30], but the coupling is usually hard to be externally tuned/controlled without affecting the cavity resonance.

In atomic systems, different cooling and trapping schemes (laser cooling, magnetic-optic trapping etc.) are used to suppress Doppler broadening and narrow the atom linewidth. Effort on engineering the layout of the cavities for enhancing the cavity quality factor is also undergoing [31]. The loss in cavity can be suppressed by avoiding any abrupt interruption of optical distribution. The fabrication for implementing the optimal design

stays challenging for the nano-meter scale engineering of the device layout, where the light distribution only depends on the refractive index and cavity designs rather than the intensity profile generated in free space laser.

The functionalities realized by on-chip devices (quantum dot-cavity, or cavity-cavity coupling) can be used broadly for stopping/slowing light in optical buffers/memories, which is an important building block for classical photonic circuits.

3.2.2 Experimental implementation

We next examine the controlled cavity-cavity phase tuning with integrated electrodes as illustrated in Fig. 3. Phase between the cavities is given by $\Phi = \int_0^L dl\omega_g n_{eff}(l,T)$ where n_{eff} is local effective index of photonic crystal waveguide, 2.768 at 1550 nm for room temperature, and L is the length of the photonic crystal waveguide between two cavities. A second electrode is placed beside the photonic crystal waveguide to locally adjust the refractive index of the waveguide between the two cavities (the red part in Fig. 3-2a). For this second sample, the active cavity has Q_{loaded} = 7,500, Q_{in} = 30,000, and resonance wavelength is thermally tuned to 1569.86 nm, and the target cavity has loaded quality factor Q_{loaded} = 8,500, Q_{in} = 15,000, with resonance wavelength at 1569.97 nm. After placing the resonant frequencies of the two cavities close enough (δ [=$2\tau_{total}(\omega_1-\omega_2)$] = 1.9 and less than 3.5 [6]), the relative cavity-cavity phase difference is adjusted through thermal-optic control of the waveguide between two cavities: $\Delta\Phi=dn/dT\times\Delta T\times L_{eff}/\lambda_c\times 2\pi$, where ΔT is the increased waveguide temperature, and L_{eff} is the the length of the

waveguide effectively heated up by the electrode placed between two cavities. Fig. 3a shows that the transmission lineshape is gradually tuned from a flat-top reflection filter to an EIT-like optical resonance when the power applied on integrated phase tuning electrode is increased from 4.13 mW to 6.91 mW. The phase shift $\Delta\Phi$ by the local refractive index change is tuned from 0.07π to -0.03π when the phase local tuning power increases from 4.13 mW to 6.91 mW, which corresponds to a sensitivity of 0.038π/mW. To illustrate the phase tuning physics, the CMT simulated lineshape with fixed detuning (δ at 1.6) and increasing phase (from out-of-phase to in-phase) is illustrated in Fig. 3-4a, and matched well with experimental results without any fitting parameters. With the average of the two cavity resonances maintained, the tilted EIT-like peak with increasing phase tuning power is induced by the different *Q*s of the two interfering cavities. The curve fitting extracted cavity-cavity splitting and the phase are plotted in Fig. 3-4 b and c respectively. The maximum cavity splitting would be upto 27GHz, verified at two different initial resonance detuning (δ=0 and 0.1). The cavity splitting would decreases with higher phase tuning power. The phase only changes ~0.07 by fitting the CMT with the measured transmission spectrum.

3.3 Device fabrication and measurement

3.3.1 Integrated electrodes fabrication

As shown in Fig. 3-5a, b, the photonic crystal cavities and membranes examined in this work are fabricated on a 250 nm thick silicon-on-insulator device layer via optimized 248 nm deep-ultraviolet lithography and etching for reduced disorder scattering [32]. The lattice constant of the photonic crystal is 420 nm with 110 nm hole radius (a = 420 nm, r =

0.261a, t = 0.595a). Each cavity is designed with three missing central holes (termed "*L3*"), with the nearest neighboring holes tuned and shifted [33] to enhance intrinsic quality factor (Q_{in} ~ 60,000 from 3D FDTD calculations [34]). Fig. 3-5c shows an example 2D finite-difference time-domain simulation of the *L3* cavity with the tuning electrode outline. We note that the thermal electrodes are nanofabricated at four lattice periods away from the cavity (Fig. 3-5c) such that the heat is effectively diffused from electrodes to the cavity region and intrinsic cavity Q is not affected by the metal absorption. If the metal is placed too close to cavity (less than three lattice periods), much of the light would be coupled into plasmon modes (experimentally observed from the top scattering image) of metal electrode and the cavity Q is significantly attenuated. The distance separation (L) between two *L3* cavities is 60 μm and includes thermal isolation trenches to achieve independent cavity and phase (in the photonic crystal waveguide) tuning.

To achieve the integrated tuning electrodes on the suspended membranes, two nanofabrication approaches are developed. The first approach is shown in Fig. 3-5d subpanels (i), (ii), (iii), where the electrode features are first aligned to the photonic crystal cavities through electron-beam lithography and the sacrificial undercut etch of the photonic crystal membranes as the final step. The second approach involves sacrificial release of the membranes first, before electron-beam alignment and electrode patterning through lift-off [Fig. 3-5 subpanels (i), (ii'), (iii')]. The misalignment in the spatial electron-beam registration between the electrodes and the cavities is estimated to be ~ 200 nm. The tuning electrode is electron-beam evaporated with 100 nm chrome. The folded serpentine layout of the heating electrodes, along with a convex profile "bending away" from the cavity center, is designed and written so as to maximize the (joule) heating while

minimizing perturbation to the *L3* optical cavity field (from intrinsic metal absorption) when positioned close to the nanocavities (Fig. 3-5c) [35].

Table 3-1. The tuning efficiency by using metal pads with two thicknesses

	$\lvert\lambda_A - \lambda_B\rvert$	Pad Thickness	Pad Resistance	Thermal tuning efficiency	Cavity resonance tuning efficiency
Set 1	10nm	50nm	2.7 k Ohm	1.29 K/mW	1.27 nm / mW
Set 2	2.5nm	100nm	1.3 k Ohm	7.5 K/mW	1.60 nm / mW

The symmetric electrode profile ensures symmetric heat flux to the coupled cavities. With a brief HF etch before electron-beam evaporation, the native oxide or organic materials on the top surface is removed and hence direct contact between the chrome and photonic crystal membrane is achieved. With the second approach in nanofabrication [Fig. 3-5d subpanels (i), (ii'), and (iii')], the resulting edge interface of the lifted-off electrodes is around 50 nm and the resistance for this specific design is around 1.3 kΩ. Fig. 3-6 (a-j) shows the detailed nanofabrication flowchat described above.

3.3.2 Measurement

Transmission measurements are performed with amplified spontaneous emission sources, with polarization controllers and tapered lensed input/output fiber coupling. DC bias is applied to the nanofabricated electrodes. The output is sent to an optical spectrum analyzer. An optical image of the sample and three probes is shown in Fi.g 3-7a. Fig. 3-7b is the image of one cavity tuning, and Fig. 3-7c illunstrates the both cavity and phase tuning by three cavities. In these measurements, each cavity is implemented in the

over-coupled regime ($Q_{coupling}$ ~ 6,000), with a resulting measured loaded Q in the range of 5,600 to 8,500 to allow for coherent in-plane cavity-cavity interference. The typical resonance extinction ratio is measured to be ~ 15 dB, and the correspondent intrinsic cavity Qs is ~ 33,000.

3.4 Thermal electric tuning of silicon photonic crystal cavities

3.4.1 Tuning photonic crystal cavity with integrated electrodes

Fig. 3-8a shows the resonance wavelengths of two *L3* cavities when the shorter wavelength resonance (at 1581.9 nm) of the active cavity is thermally red-shifted to align up to the longer wavelength resonance (1584.4 nm) of the target one. The initial resonance wavelength difference between the active and target cavities (λ_{target} - λ_{active}) is 2.7 nm without external power supplied. In Fig. 3-8a inset, we show the fine-tuning at a higher base temperature (with ~ 1 nm red-shifted resonances). In Fig. 3-8b we plot the fine tuning of the active cavity near the target cavity for observing the interference patterns, with the resulting detuning δ [=$2\tau_{total}(\omega_1-\omega_2)$] illustrated. We emphasize that when δ < ~3.5, the linewidth of the transparency peak is narrower than the individual cavity linewidths [6, 21], in the regime of Fano- and EIT-like interferences. We also exploring the sensitivity of interference lineshapes to different chip (base) temperatures – the tuning efficiency $d\delta/dP$ drops from 8.5 /mW to 2.9 /mW after the base temperature being raised by 14K. Fig. 3-8c shows four example transmission lineshapes with interference between two indirectly coupled cavities, with detuning δ of 2.3, 2.6, 2.9 and 4.0, corresponding to local cavity tuning power 3.59, 3.49, 3.39 and 3.26 mW applied on the electrodes respectively. In addition to the lineshape shown in Fig. 2c with δ at 4.0, the other panels also illustrate an

even smaller detuning through the integrated control, where an asymmetric lineshape indicative of Fano-like interferences is observed. There is also a Fabry-Perot background in the measured spectra which arises from the finite termination of the photonic crystal and the chip. By simulating the experimental data with coupled mode theory (CMT), the cavity-to-cavity phase difference that satisfies the condition of forming a Fabry–Perot resonance is 0.85π for all cases.

The thermal control of the cavity has a resonance redshift of 1.60 nm/mW at room temperature. The tuning efficiency decreases to only one third as substrate temperature increases 14K. When only the shorter wavelength cavity is thermally-tuned, we note that there is negligible cross-talk for the target cavity, where the tuning cross-talk is observed to be 0.038 nm/mW by linear curve fitting of the unintended target cavity shift (Inset of Fig. 3-8a). The devices typically operate with voltage biases up to ~ 6 V. The thermal impedance of the photonic crystal cavity is defined as: $1/R_{th}=\Delta T/\Delta P =(\Delta\lambda/\Delta P)\times(\Delta n/\Delta\lambda)\times(\Delta T/\Delta n)$, where R_{th} is the thermal resistance (in units of mW/K), ΔT is the temperature difference, ΔP is the joule heating power supplied by electrodes, and $\Delta\lambda$ is the cavity wavelength shift. $\Delta\lambda/\Delta P$ is given by the measurement. The temperature dependence of the refractive index $\Delta n/\Delta T$ in silicon is 1.86×10^{-4} /K [22], with $\Delta n/\Delta\lambda=n_{Si}/\lambda_{active}$ obtained within the first-order perturbation for the high index material [12, 23] (n_{Si}=3.485). The thermal resistance at room temperature is estimated to be 18.7 K/mW, comparable to optical tuning at 15.4 K/mW [6, 21].

3.4.2 Effects of substrate temperature on tuning efficiency

It is noted that the electrodes tuning efficiency decreases dramatically with the increasing substrate temperature. By placing the heater on the sample holder and a thermistor on top the chip, we demonstrate effective heating by the off-chip heater. We take the transmission spectrum of a four cavity system at different substrate temperatures (25^{o}C, 32^{o}C, 66^{o}C) and background Fabry Perot (Fig. 3-9b). The cavity resonance and background Fabry Perot shifts are ploted in Fig. 3-9c. The tuning efficiency from chip temperature to the cavity resonance is about 0.023nm/^{o}C.

The measured thermal optical tuning of silicon refractive index is $5x10^{-5}/^{o}$C, which is lower than the standard parameter for silicon ($8x10^{-5}/^{o}$C at 1550nm and room temperature). The mismatch between measurement and theory may be caused by non-fully contacted thermistor and the chip.

3.4.3 Thermal conductivity on photonic crystals

Two dimensional photonic crystals can be considered as in-plane porous silicon thin film with large pore radius and high porosity. The thermal conductivity of bulk silicon is 148 W/mK at room temperature, but it would be greatly hindered by phonon scattering in the nanostructured systems. Crystalline silicon with pores of diameter 200nm is measured to have thermal conductivity of 23 W/mK [36]. In-plane thermal conductivity of the 260nm thick silicon membrane on silicon oxide substrate is measured to be 90 W/mK [37].

In experiment, we fabricated micro-heater with ~5μm diameter radius by e-beam lithography with round edge. Six S1-L3 cavities with different distance to the heating pad

are employed as sensors to measure the local temperature by thermal optic effect (Fig. 3-10). The six cavities are coupled onto the same waveguide, and we track the cavity resonances on the transmission with different heating power. Only the cavities within 1.5μm away from the heater are effectively tuned. We confirm the measured parameter by a compact model for analyzing the heat flow in silicon photonic crystal membrane. The thermal conductivity measured here might be useful for operating optoelectronic devices on chip (lasers, modulators), where high thermal stability is of paramount importance.

The thermal transport equation can be expressed as:

$$dQ / dt = \kappa A \times dT / dr \tag{8}$$

Where dQ/dt is the heat flux from the source. A is the cross-section area, and is the product of the thin film thickness t and the half circumference of the heating pad (πr). K is the thermal conductivity. T is the temperature. r is the distance to the heating source. dT/dx represents the temperature gradience over the space. Considering the heat is dissipated homogeneously along the 2D plane, the equation can be simplified as:

$$\frac{d(T / P)}{dr} = -\frac{1}{\pi t \kappa \times r} \tag{9}$$

Here P is the heating power. r is the distance to the heating source. t is the thickness of the film. From the curve fitting, we know that near the edge of the half-circle metal, the tuning efficiency $d(T/P)/dr$ is estimated to be 10.7 K/mW/μm. The half circumference of the heating pad is estimated to be 20μm. The thickness of the membrane is 0.25μm. From the parameters given above, the thermal conductivity of the photonic crystal membrane is

about 20 W/m/K, which is about 7 times smaller than the bulk silicon at room temperature: 148 W/m/K.

The thermal conductivity of the photonic crystals can also be theoretically calculated. Based on Molecular dynamics simulations and ballistic diffusive models, the transverse thermal conductivity of silicon with cylindrical pores can be expressed as:

$$k_{eff} = k_m \frac{1}{\frac{1}{f(f_v)} + \alpha \frac{\sqrt{f_v}}{F(f_v) d_p}} \tag{10}$$

$$F(f_v) = \sqrt{4 f_v / \pi}(\sin^{-1}\sqrt{4 f_v / \pi} - \pi/2) + \sqrt{1 - 4 f_v / \pi} \tag{11}$$

Where k_m is the thermal conductivity of the silicon thin film; f_v=0.247 is the prosity (air to volume ratio); $f(f_v)=(1-f_v)(1+\beta f_v^{\gamma})$; d_p=0.1 is the diameter of the hole; α=50.9, β=1821.1, γ=1.9 are fitting parameters [38-39].

According to Fick's law, the thermal diffusion length inside silicon could be obtained through the equation: $L=2\ sqrt(Dt)$. Where D is the thermal diffusivity of silicon, 0.88 cm^2/s [40], t is the recombination lifetime. We measured the resistance of the meta-material made of silicon membrane with periodic holes. The resistance tested between the two electrodes (top one and the bottom heater) is around 1 MΩ, From the equation: $R=\rho L/S$, the resistivity of the photonic crystal membrane is estimated as 0.1 Ω-cm, with the distance between the electrodes L=10μm, the cross section 0.25μm×3μm (estimated effective width, taken into account of the carrier flow blocking by the holes). Thermal conductivity of silicon is about 148 W/m-K at room temperature. The surface carrier doping is estimated around 10^{18} cm-3 from the resistivity value, which is much higher than the impurity doping in the membrane (p dope 10^{16} cm-3). The carrier lifetime

is estimated around 10^{-6}s for surface doping (either on the surface or sidewall of the air-holes), and 10^{-4}s for bulk doping (given by IME) [41]. In silicon membrane, the heat transport would be dominant by the fast recombined surface carriers, so the thermal diffusion length would be around L=15 μm. Different from usual bulk/thin film material, the air holes on the silicon membrane would impede the carrier transport, and thus enhance the resistance and shorten the thermal diffusion length.

Previously the thermal optic tuning on PhC membrane is using laser beam as heating source [42], which involves more complexity on modeling, Because the laser beam does not have sharp boundary (Gaussian beam), and the conversion efficiency from light to heat is hard to be accurately tested . In measurement, the rigorous and stable alignment is hard to be achieved also. For the electric micro-heater, the heat flux is generated from joule heating only, and the location of the heater is pre-defined in the fabrication. The parameters, including the heat flux, and the heater to sensor distance can be easily tested.

Surface effect would hinder both phonon and electron transport in low dimensional silicon structure, including two dimensional (2D) thin film, one dimensional (1D) nanowires. The thermal conductance usually reduces with the dimension number due to boundary scattering. For example, the thermal conductivity of bulk silicon is 150 W/m-K at room temperature, but reduces to ~100 W/m-K for 0.5um thick membrane (2D), and further cut down to 10 W/m-K for 8nm by 8nm silicon nano wire (1D). However, the high surface to volume ratio of low dimensional material would increase the phonon-boundary scattering, and thus increases the thermal conductance by ballistic phonon transport.

The phonon transport is converted from diffusive phonon transport to ballistic transport when the device characteristic length is comparable to the heat-carrier mean free path [43]. The Phonon Mean free path in silicon is measured to be 12 μm around room temperature [44]. The geometric confinement adds a frequency independent term to total phonon lifetime to represent the effect of boundaries [45].

Bibliography

[1] J. I. Cirac, P. Zoller, H. J. Kimble, and H. Mabuchi, Quantum State Transfer and Entanglement Distribution among Distant Nodes in a Quantum Network, *Phys. Rev. Lett.* **78**(16), 3221–24 (1997)

[2] G. Khitrova, H. M. Gibbs, M. Kira, S. W. Koch, and A. Scherer, Vacuum Rabi splitting in semiconductors. *Nature Physics* **2**, 81-90 (2006)

[3] D. Englund, D. Fattal, E. Waks, G. Solomon, B. Zhang, T. Nakaoka, Y. Arakawa, Y. Yamamoto, and J. Vuckovic, Controlling the Spontaneous Emission Rate of Single Quantum Dots in a Two-Dimensional Photonic Crystal, *Phys. Rev. Lett.* **95**, 013904 (2005)

[4] X. Yang, M. Yu, D. L. Kwong, and C. W. Wong, All-Optical Analog to Electromagnetically Induced Transparency in Multiple Coupled Photonic Crystal Cavities. *Phy. Rev. Lett.* **102**, 173902-173905 (2009).

[5] J. Pan, S. Sandhu, Y. Huo, N. Stuhrmann, M. L. Povinelli, J. S. Harris, Fejer, M. M. & S. Fan, Experimental demonstration of an all-optical analogue to the superradiance effect in an on-chip photonic crystal resonator system. *Physical Review B* **81**, 041101-041104 (2010).

[6] M. Yamaguchi, T. Asano, S. Sato and S. Noda, Photonic Quantum Computation with Waveguide-Linked Optical Cavities and Quantum Dots. arXiv:1101.3508v1.

[7] http://qwiki.stanford.edu/images/1/1c/Qousersguide.pdf

[8] S. Yoshiya, Y. Tanaka, J. Upham, Y. Takahashi, T. Asano and S. Noda, Strong coupling between distant photonic nanocavities and its dynamic control **6**, 56-61 *Nature Photonics* (2011).

[9] D. D. Smith, H. Chang, K. A. Fuller, A. T. Rosenberger, and R.W.Boyd,

Coupled-resonator-induced transparency, *Phys. Rev. A* **69**, 063804 (2004)

[10] S. Kocaman, X. Yang, J. F. McMillan, M. B. Yu, D. L. Kwong, and C. W. Wong, Observations of temporal group delays in slow-light multiple coupled photonic crystal cavities, *Applied Physics Letters* 96, 221111 (2010).

[11] M. F. Yanik, W. Suh, Z. Wang, and S. Fan, Stopping light in a waveguide with an all-optical analog of electromagnetically induced transparency, *Phys. Rev. Lett.* **93**, 233903 (2004);

[12] S. Fan, Manipulating light with photonic crystals, *Physica B* **394**, 221 (2007).

[13] X. Yang, M. Yu, D.-L. Kwong, and C. W. Wong, All-optical analogue to electromagnetically induced transparency in multiple coupled photonic crystal cavities, *Phys. Rev. Lett.* **102**, 173902 (2009);

[14] L. Ramunno and S. Hughes, Disorder-induced resonance shifts in high-index-contrast photonic crystal nanocavities, *Phys. Rev. B* **79**, 161303 (2009).

[15] C. A. Husko, A. de Rossi, S. Combrie, Q. V. Tran, F. Raineri, and C. W. Wong, Ultrafast all-optical modulation in GaAs photonic crystal cavities, *Appl. Phys. Lett.* **94**, 021111 (2009).

[16] D. Englund, B. Ellis, E. Edwards, T. Sarmiento, J. S. Harris, D. A. B. Miller, and J. Vuckovic, Electrically controlled modulation in a photonic crystal nanocavity, *Opt. Express* **17**, 15409 (2009).

[17] X. Yang, C. J. Chen, C. A. Husko, and C. W. Wong, Digital resonance tuning of high-Q/Vm silicon photonic crystal nanocavities by atomic layer deposition, *Appl. Phys. Lett*. **91**, 161114 (2007);

[18] C. W. Wong, P. Rakich, S. G. Johnson, M. Qi, H. I. Smith, L. C. Kimerling, E. P.

Ippen, Y.-B. Jeon, G. Barbastathis, S.-G. Kim, Strain-tunable silicon photonic band gap microcavities in optical waveguides, *Appl. Phys. Lett.* **84**, 1242 (2004).

[19] R. L. Espinola, M. C. Tsai, J. Yardley, and R. M. Osgood, Jr., Fast and low power thermo-optic switch on thin silicon-on-insulator, *Photon. Tech. Lett.* **15**, 1366 (2003); A Faraon and J Vučković, Local temperature control of photonic crystal devices via micron-scale electrical heaters, *Appl. Phys. Lett.* **95**, 043102 (2009).

[20] S. Manipatruni, K. Preston, L. Chen, and M. Lipson, Ultra-low voltage, ultra-small mode volume silicon microring modulator, *Optics Express* **18**, 18235 (2010); A. Alduino, and M. Paniccia, Interconnects: Wiring electronics with light, *Nature Photonics* **1**, 153 (2007).

[21] S. Kocaman, X. Yang, J. F. McMillan, M.B. Yu, D. L. Kwong, and C. W. Wong, Observations of temporal group delays in slow-light multiple coupled photonic crystal cavities, *App. Phys. Lett.* **96**, 221111 (2010).

[22] G. Cocorullo and I. Rendina, Thermo-optical modulation at 1.5 μm in silicon etalon, *Elect.. Lett.* **28**, 83 (1992).

[23] F. Xia, L. Sekaric, and Y. Vlasov, Ultracompact optical buffers on a silicon chip, *Nature Photonics* **1**, 65 (2007); S. Mookherjea, J. S. Park, S. H. Yang and P. R. Bandaru, Localization in silicon nanophotonic slow-light waveguides, *Nature Photonics* **2**, 90 (2008).

[24] T. Baba, Slow light in photonic crystals, *Nature Photonics* **2**, 465 (2008); J. F. McMillan, M. Yu, D.-L. Kwong, and C. W. Wong, Observations of spontaneous Raman scattering in silicon slow-light photonic crystal waveguides, *Appl. Phys. Lett.* **93**, 251105 (2008).

[25] S. E. Harris, Electromagnetically Induced Transparency, *Phys. Today* **50**, 36 (1997); L.V. Hau, S. E. Harris, Z. Dutton, and C. H. Behroozi, Light speed reduction to 17 metres per second in an ultracold atomic gas, *Nature* **397**, 594 (1999).

[26] M. S. Bigelow, N. N. Lepeshkin, and R. W. Boyd, Superluminal and Slow Light Propagation in a Room-Temperature Solid, *Science* **301**, 200 (2003); J. J. Longdell, E. Fraval, M. J. Sellars, and N. B. Manson, Stopped Light with Storage Times Greater than One Second Using Electromagnetically Induced Transparency in a Solid, *Phys. Rev. Lett.* **95**, 063601 (2005).

[25] M. Mucke, E. Figueroa, J. Bochmann, C. Hahn, K. Murr, S. Ritter, C. J. Villas-Boas, and G. Rempe, Electromagnetically induced transparency with single atoms in a cavity, *Nature* **465**, 755 (2010).

[26] D. D. Smith, H. Chang, K. A. Fuller, A. T. Rosenberger, and R. W. Boyd, Coupled-resonator-induced transparency, *Phys. Rev. A* **69**, 063804 (2004); Q. Xu, S. Sandhu, M. L. Povinelli, J. Shakya, S. Fan, and M. Lipson, Experimental realization of an on-chip all-optical analogue to electromagnetically induced transparency, *Phys. Rev. Lett.* **96**, 123901 (2006); Q. Xu, P. Dong, and M. Lipson, Breaking the Delay-Bandwidth Limit in a Photonic Structure, *Nature Physics* **3**, 405 (2007).

[27] L. Maleki, A. B. Matsko, A. A. Savchenkov, and V. S. Ilchenko, Tunable delay line with interacting whispering-gallery-mode resonators, *Optics Lett.* **29**, 626 (2004); Q. Li, T. Wang, Y. Su, M. Yan, and M. Qiu, Coupled mode theory analysis of mode-splitting in coupled cavity system, *Optics Exp.* **18**, 8367 (2010).

[28] X. Yang, M. Yu, D.-L. Kwong, and C. W. Wong, Coupled resonances in multiple silicon photonic crystal cavities in all-optical solid-state analogy to

electromagnetically-induced transparency, *IEEE J. Sel. Top. Quant. Elect.* **16**, 288 (2010).

Y.-F. Xiao, J. Gao, J. F. McMillan, X. Yang, Y.-L. Chen, Z.-F. Han, G.-C. Guo, and C. W. Wong, Coupled electrodynamics in photonic crystal cavities towards controlled phase gate operations, *New J. of Phys.* **10**, 123013 (2008).

[29] S.-M. Tan, A quantum optics toolbox for Matlab 5, *J. Opt. B: Quantum Semiclass. Opt* **1**: 161 (1999)

[30] G. Lenz, B. J. Eggleton, C.K. Madsen, and R. E. Slusher, Optical delay lines based on optical filters, *IEEE J. Quant. Elect.* **37**, 525 (2001).

[31] B.-S Song, et al, Ultra-high-Q photonic double-heterostructure nanocavity, *Nature Materials* **4**, 207-210 (2005)

[32] R. Chatterjee, N. C. Panoiu, K. Liu, Z. Dios, M. Yu, M. T. Doan, L. J. Kaufman, R. M. Osgood, and C. W. Wong, Achieving subdiffraction imaging through bound surface states in negative refraction photonic crystals in the near-infrared range, *Phys. Rev. Lett.* **100**, 187401 (2009); S. Kocaman, R. Chatterjee, N. C. Panoiu, J. F. McMillan, M. B. Yu, R. M. Osgood, D. L. Kwong, and C. W. Wong, Observations of zero-order bandgaps in negative-index photonic crystal superlattices at the near-infrared, *Phys. Rev. Lett.* **102**, 203905 (2009).

[33] Y. Akahane, T. Asano, B.-S. Song, and S. Noda, High-*Q* photonic nanocavity in a two-dimensional photonic crystal, *Nature* **425**, 944 (2003).

[34] S. G. Johnson, M. Ibanescu, M. A. Skorobogatiy, O. Weisberg, J. D. Joannopoulos, and Y. Fink, Perturbation theory for Maxwell's equations with shifting material boundaries, *Phys. Rev. E* **65**, 066611 (2002)

[35] T. Gu, S. Kocaman, X. Yang, J. F. McMillan, M. B. Yu, G.-Q. Lo, D.-L. Kwong, and

C. W. Wong, Deterministic integrated tuning of multi-cavity resonances and phase for slow-light in coupled photonic crystal cavities, *Appl. Phys. Lett.* **98**, 121103 (2011)

[36] G. Benedetto, L. Boarino and R. Spagnolo, Evaluation of thermal conductivity of porous silicon layers by a photoacoustic method, *Applied Physics A: Materials Science & Processing* **64**, 155-159 (1997)

[37] M. S. Aubain, and Prabhakar Bandaru, In-plane thermal conductivity determination in silicon on insulator (SOI) structures through thermoreflectance measurements, In *MRS Proceedings*, vol. 1267, Cambridge University Press, 2010

[38] J-H. Lee, J. C. Grossman, J. Reed, and G. Galli, Lattice thermal conductivity of nanoporous Si: Molecular dynamics study, *Applied Physics Letters* **91**, 223110-223110 (2007)

[39] J. Fang, and L. Pilon, Scaling laws for thermal conductivity of crystalline nanoporous silicon based on molecular dynamics simulations, *Journal of Applied Physics* 110, **6** 064305-064305 (2011)

[40] http://www.electronics-cooling.com/2007/08/thermal-diffusivity/ Materials Data

[41] R. Hacker, and A. Hangleiter, Intrinsic upper limits of the carrier lifetime in silicon, *J.Appl. Phys.* **75**, 1 (1994)

[42] J. Pan, Y. Huo, S. Sandhu, N. Stuhrmann, M. L. Povinelli, J. S. Harris, M. M. Fejer, and S. Fan, Tuning the coherent interaction in an on-chip photonic-crystal waveguide-resonator system, *App. Phys. Lett.* **97**, 101102 (2010).

[43] G. Chen, Ballistic-Diffusive Heat-Conduction Equations, *Phys. Rev. Lett.* **86**, 2297-2300 (2001)

[44] R. Gereth adn K. Hubner, Phonon Mean Free Path in Silion Between 77 and 250K,

Phys. Rev. **134**, A235-A240 (1964)

[45] H. B. Casimir, *Physica* **5**, 295 (1938)

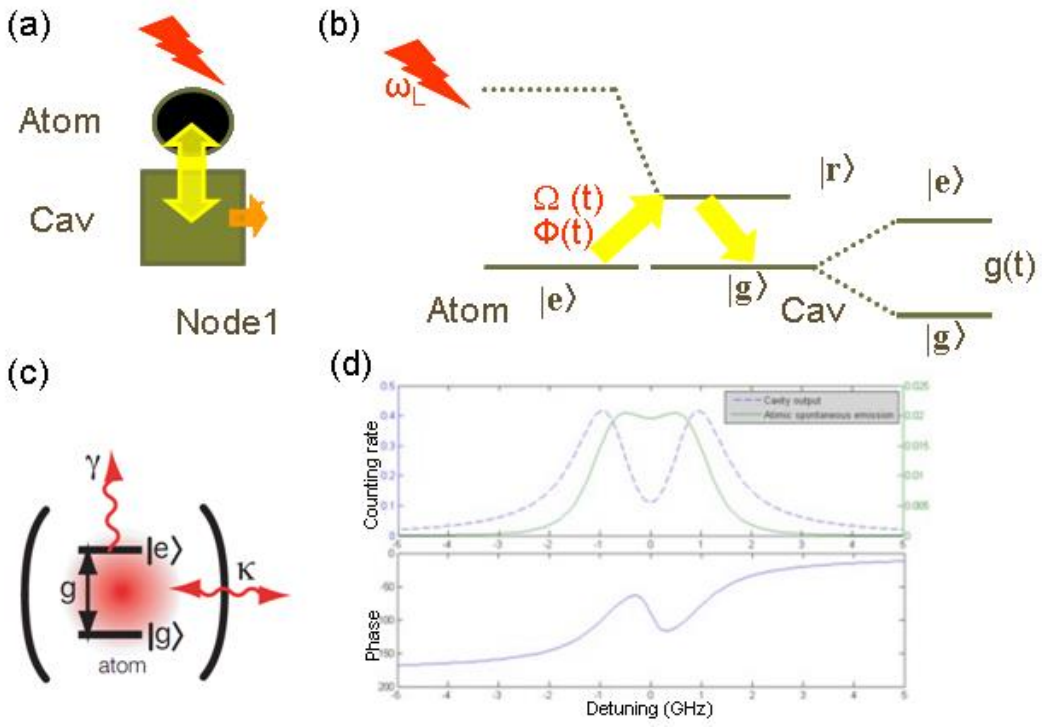

Fig. 3-1 Controlling information storage and release in single node. (a) Node composition of an atom and cavity. Red arrow: excitation laser; Yellow arrow: atom-cavity interaction; Orange arrow: photon leakage in cavity. (b) Excitation process shown in band diagram [1]. The control light pulse (with wavelength of ω_L, amplitude of $\Omega(t)$ and phase of $\Phi(t)$) excite the atom to an high energy state, and the energy is delivered to the excited state |r> through Raman process. Under the resonance excitation, the ground state |g> splits to two states |e> and |g> with coupled strength g(t). (c) Energy state in Atom in cavity. (d) (up) Photocounting rates for cavity output (dash line) and for atomic spontaneous emission (solid line). (down) Phase of intracavity light field.

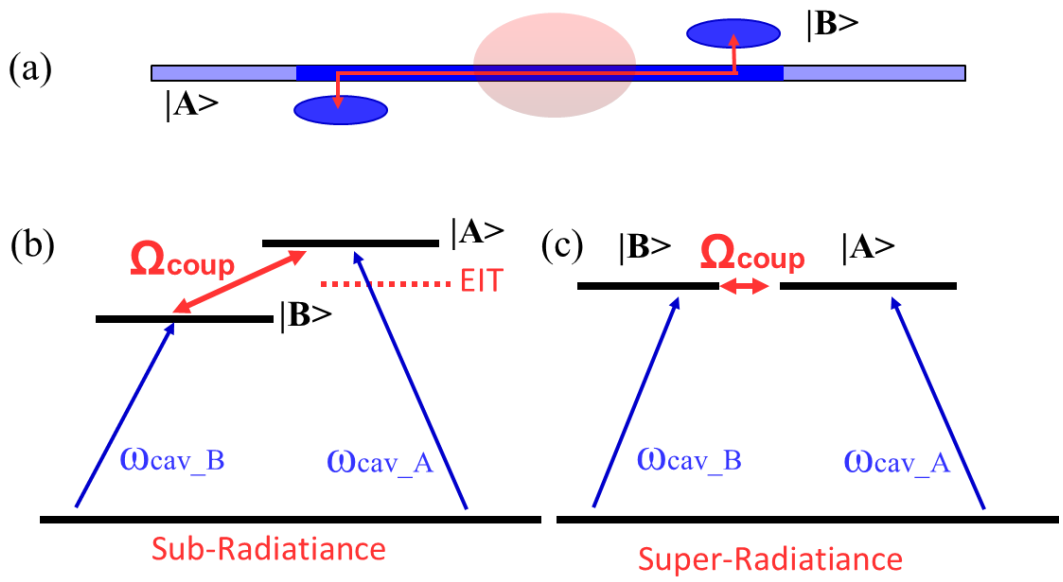

Fig. 3-2 Schematic of two coupled cavity system. (a) The coupling coefficient between cavity and waveguide $\kappa=(1/2/\tau_c)^{1/2}$ (b) Schematics of (b) EIT mechanism, (c) superradiance two cavity coupled system in a. (i). Electromagnetically-Induced-Transparency (δ=1.9, βL=0) red dot line is the experimental data and the blue solid curve is the coupled mode theory simulation (ii): Superradiance condition. Light blue dash line is the single cavity dip (δ=0.1, $\beta L=\pi$). The external tuning is realized by the integrated electrode fine tuning of the local refractive index

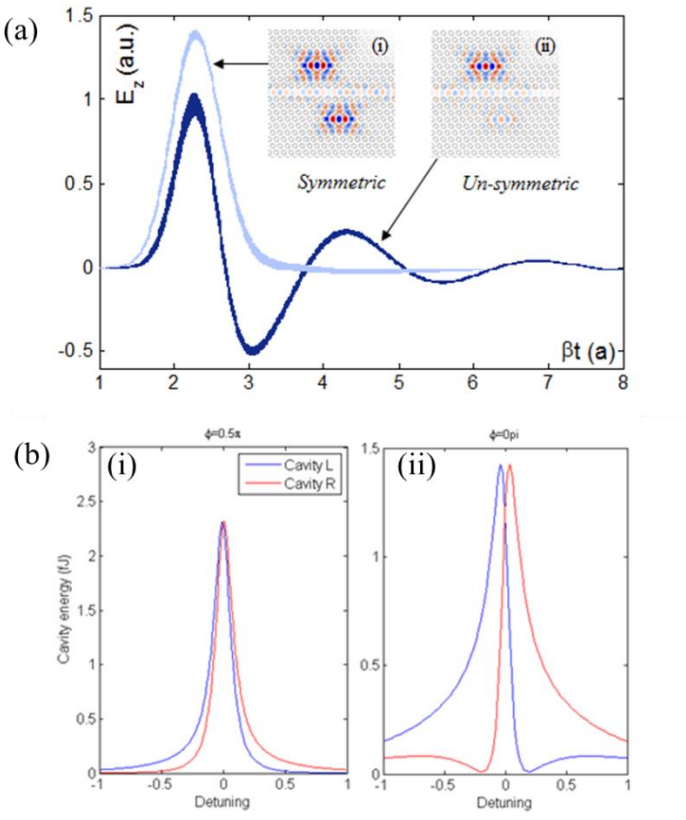

Fig. 3-3 Phase dependent cavity-cavity splitting (a) 2D FDTD simulation showing the eigen modes of the two cavity system with different optical path between two cavities. The magnitude of the electric field in waveguide evolves with time. The insets are eigen states with different relative phase, with zero detuning between two cavities. The distance between two cavities is (i) 3a (ii) 2a (b) Coupled mode theory simulated energy spectrum with different phase between two cavities. The blue curve is the spectrum of the left cavity, and the red curve is the right cavity. (i) phase=0.5π (ii) phase=0π

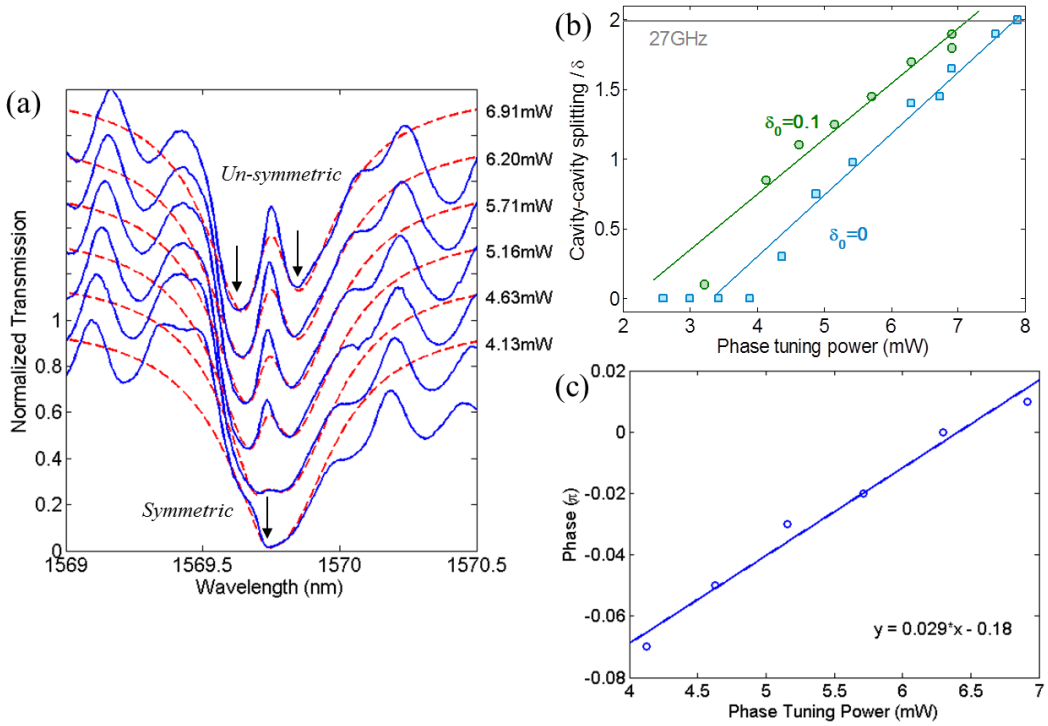

Fig. 3-4 Experimental observation of phase determined cavity-cavity splitting (a) Measured (Blue solid line) and CMT simulated transmission spectrum (Red dashed line) with increasing phase tuning power (P_{Φ}), and fixed resonance tuning power (P_r=40.8 mW).(b) The CMT extracted inter-cavity splitting versus the phase tuning power. The blue dots are experimental data for 0 resonance detuning, and the green squares are for the 0.1 resonance detuning. The lines are used for guiding eyes. (c) The CMT extracted inter-cavity phase.

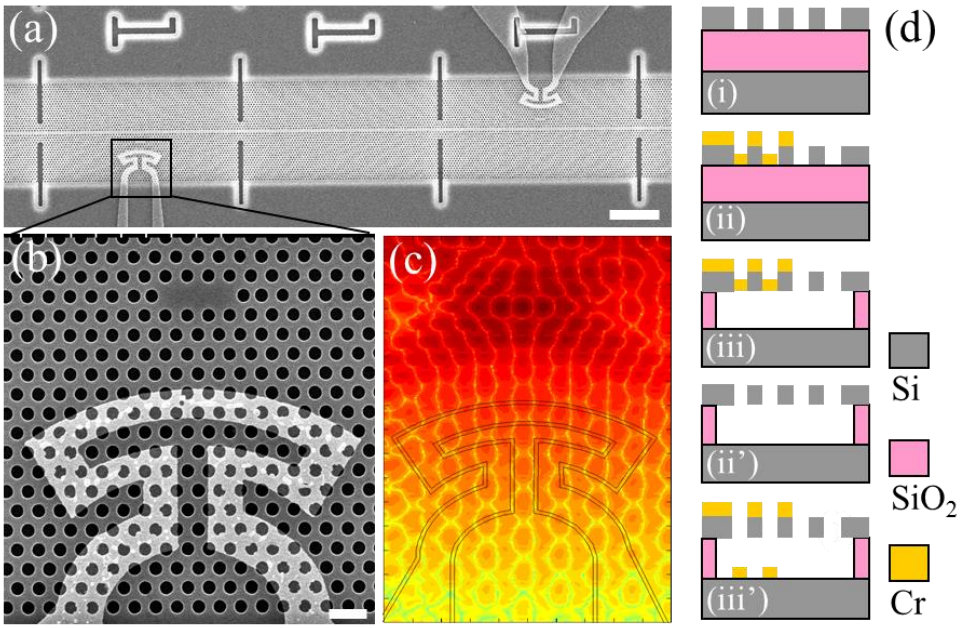

Fig. 3-5 Chip-scale integrated tuning of photonic crystal two-cavity optical EIT system. (a) SEM of thermally-tuned coupled cavities with thermal isolation trench and tuning electrodes. Scale bar: 5 μm. (b) SEM of single cavity. Scale bar: 500 nm. (c) 3D FDTD simulated model profile (log scale) with outline of thermal tuning electrode. (d) Schematics of two-step nanofabrication process flow. (i) SOI wafer, (ii) electron-beam lithography defined tuning electrodes, (iii) suspended silicon membrane with electrodes. (ii') initial sacrificial release, following by (iii') electron-beam writing of the electrodes.

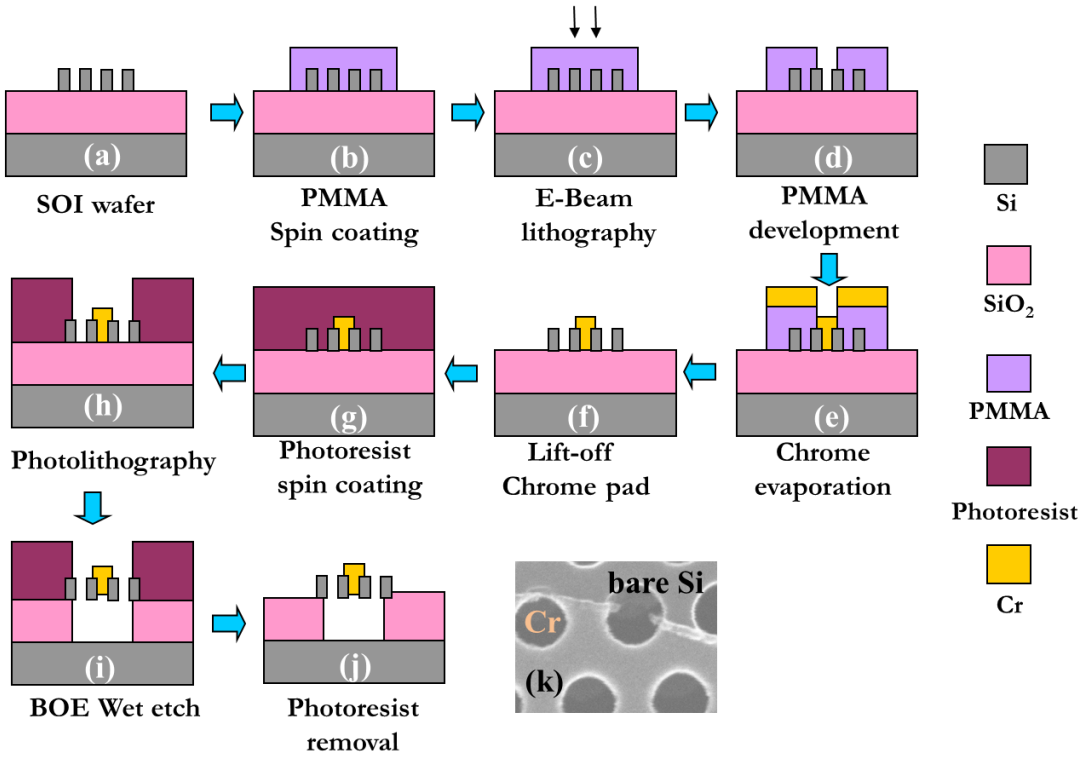

Fig. 3-6 Device nanofabrication flow chat (a) SOI structure with photonic crystal patterned on the top silicon layer. The thickness for photonic crystal layer and silicon oxide layers are 250 nm and 1 um respectively. (b) SOI structure with 200nm PMMA coating (c) Ebeam lithography for defining the metal part (d) PMMA development by MIBK:IPA (e) Chrome deposition (f) Lift-off (g) Spin casting photoresist (h) Photolithography (i) BOE wet etch (j) Sample cleaned by Aceton for removing the photoresist.

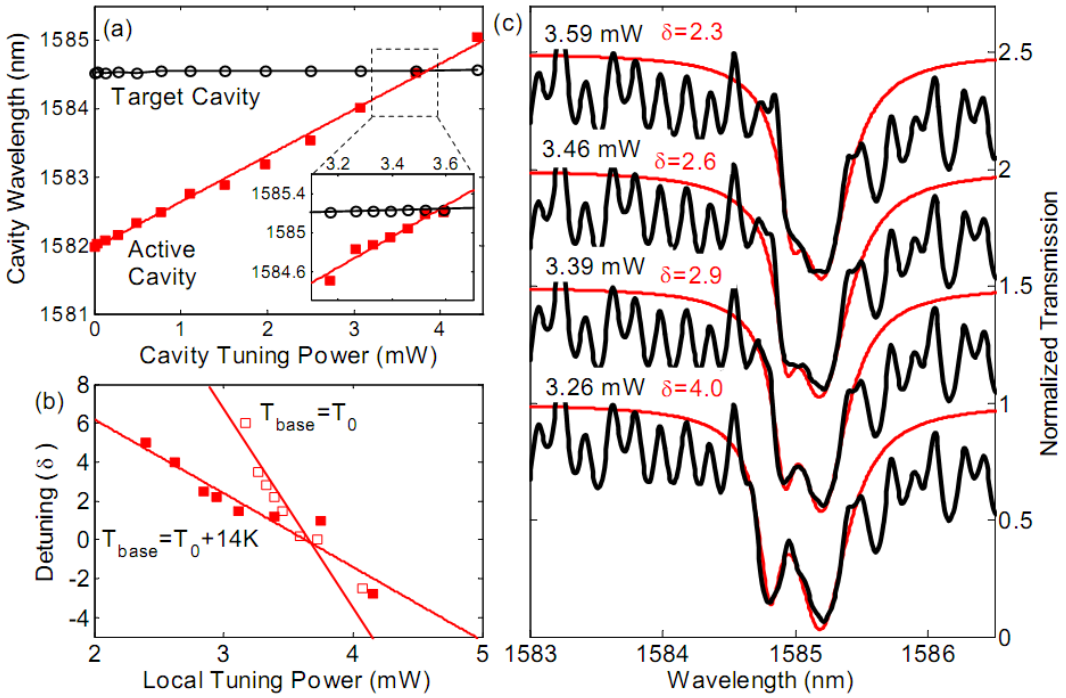

Fig. 3-7 Integrated tuning of the two-cavity resonances. (a) The resonant wavelength of the active cavity (solid squares) and the target cavity (empty circles) versus the tuning power. Inset: fine tuning cavity resonances in the cavity-cavity interference region. (b) Detuning versus local tuning power within the same region as inset of (a). Solid and empty squares are data measured at base temperature (T_0) and T_0+14K respectively. Lines are linear fits. (c) Example two-cavity coherent transmission under different local tuning powers (δ = 2.3, 2.6, 2.9 and 4.0, correspondent to cavity tuning power at 3.59 mW, 3.46 mW, 3.39 mW and 3.26 mW respectively) . Solid (black) lines are experimental data and the dashed (red) lines are coupled-mode theory fits. Curves are offset by -0.5 for clarity.

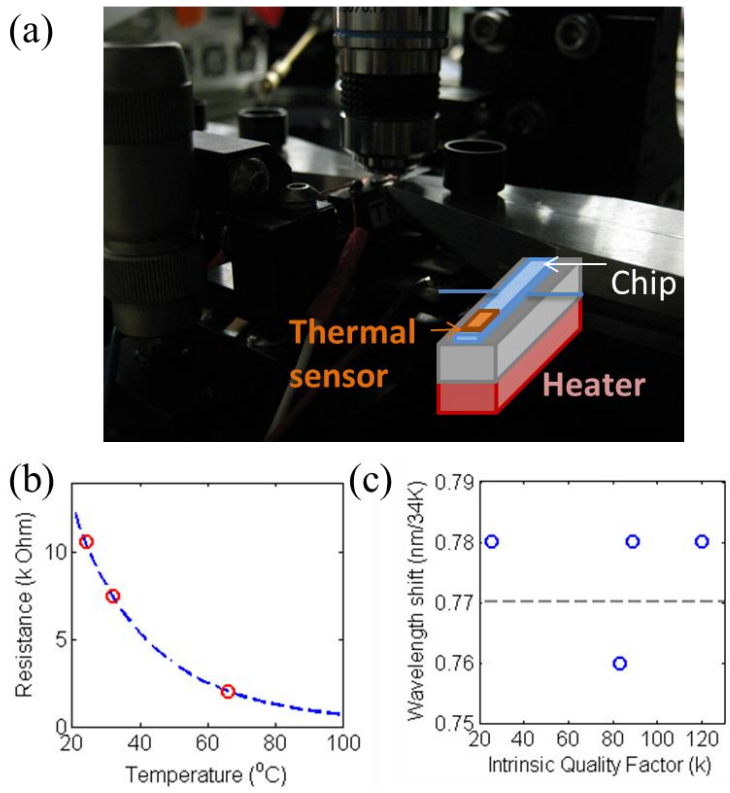

Fig. 3-8 Measurement for chip level thermal-optic tuning. (a) Experimental set-up. Inset: detailed configuration. The blue part is the chip and two fibers. The thermistor (yellow part) is placed on top of the chip (Thorlabs TH10K). The heating source (red part) is placed under the chip holder (grey part). (b) Resistance as a function of Thermistor temperature for the thermistor. The blue curve is the electrical specification given by the data sheet. The red circles mark the temperature (24oC, 32oC, 66oC) the transmission of the resonators are measured. (c) The resonance shift of four photonic crystal cavities with different quality factors (blue circles) and the Fabry Perod oscillation (grey dash line).

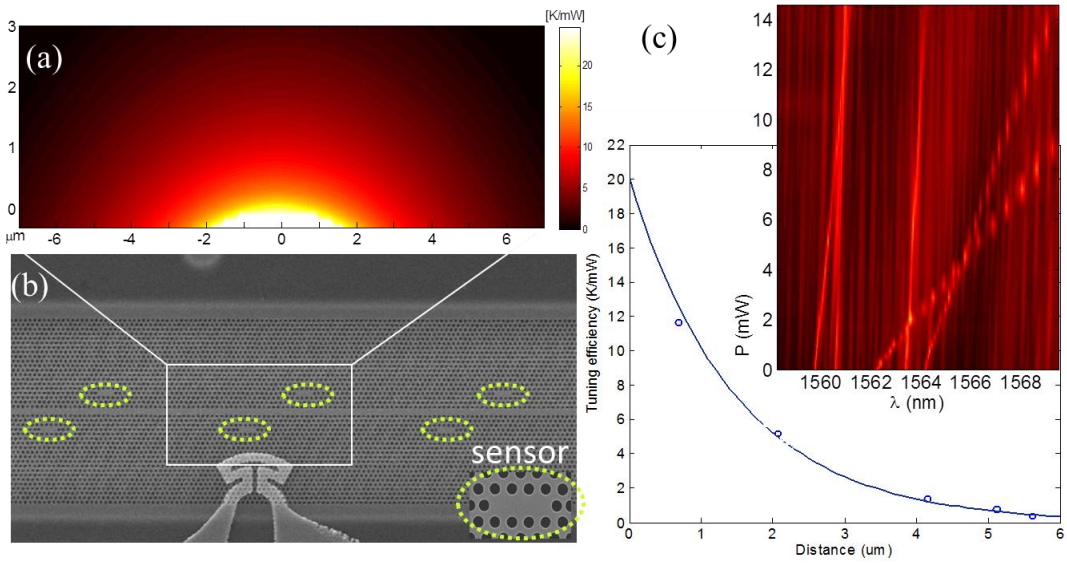

Fig. 3-9 Fabrication and measurements of cavity tuning in photonic crystal systems. a, Schematic of nanofabrication process flow b, SEM of suspended photonic crystal membrane with micro-electrodes. Inset: 2D FDTD simulations of optical field distribution and its relative position to serpent electrodes. c, Transmitted spectrum with different electrical power supply. Bright lines show the drifting of cavity resonances and fringes in the background is the Fabry-Perot oscillation.

Chapter 4

Kerr nonlinearity in graphene-silicon cavity

4.1 Introduction

Kerr effect is one of nonresonant Electronic Nonlinearities. They occur as the result of the nonlinear response of bound electrons to an applied optical field. This nonlinearity usually is not particularly large in semiconductors. But the materials having delocalized π electrons (such as polydiacetylene or graphene) can have nonresonant third-order susceptibilites five order higher than others [1]. Four-wave mixing is a Kerr nonlinear effect can be viewed as the elastic scattering of two photons of a high power pump beam, which results in the generation of two new photons at different frequencies. Four-wave mixing attracts great attention due to its broadband operation and ultra-fast response time (femtosecond scale), for the application of wavelength conversion, parametric oscillatior, amplifier etc.

4.2 Effective Kerr nonlinearity in graphene-silicon system

4.2.1 Calculations of graphene's dynamic conductivity

Graphene is a two dimensional atomic thin material and strongest material. Its charge carriers exhibit superlative intrinsic mobility [2]. The linear absorption is firstly presented here. The dynamic conductivity for intra- and inter-band optical transitions [3] can be determined from the Kubo formalism as:

$$\sigma_{\text{intra}}(\omega) = \frac{je^2\mu}{\pi\hbar(\omega + j\tau^{-1})} \quad , \tag{1}$$

$$\sigma_{\text{inter}}(\omega) = \frac{je^2\mu}{4\pi\hbar}\ln\left(\frac{2|\mu| - \hbar(\omega + j\tau^{-1})}{2|\mu| + \hbar(\omega + j\tau^{-1})}\right) , \tag{2}$$

where e is the electron charge, $\hbar$ is the reduced Plank constant, ω is the radian frequency, μ is chemical potential, and τ is the relaxation time (1.2 ps for interband conductivity and 10 fs for intraband conductivity). The dynamic conductivity of intra- and inter-band transitions at 1560 nm are $(-0.07-0.90i)\times10^{-5}$and $(4.15-0.95i)\times10^{-5}$ respectively, leading to the total dynamic conductivity $\sigma_{total}=\sigma_{intra}+\sigma_{inter}$ of $(4.1-1.8i)\times10^{-5}$. The real and imaginary parts of the conductivity and permittivity is calculated in Fig. 4-1. Given negative imaginary part of total conductivity, the TE mode is supported in graphene [4]. The light can travel along the graphene sheet with weak damping and thus no significant loss is observed for the quasi-TE mode confined in the cavity [5]. The impurity density of the 250 nm silicon membrane is ~10^{11} cm^{-2}, slightly lower than the estimated doping density in graphene.

4.2.2 Computations of effective Kerr coefficient in graphene-silicon cavities

Third-order nonlinearity susceptibility for graphene is reported as large as $|\chi^{(3)}|$~10^{-7}esu in the wavelength range of 760 to 840 nm [6]. When two external beams with frequency ω_1 (pump) and ω_2 (signal) are incident on graphene, the amplitude of sheet current generated at the harmonics frequencies ($2\omega_1$-ω_2) is described by:

$$j_e = -\frac{3}{32}\frac{e^2}{\hbar}\varepsilon_2\left(\frac{ev_F\varepsilon_1}{\hbar\omega_1\omega_2}\right)^2\frac{2\omega_1^2+2\omega_1\omega_2-\omega_2^2}{\omega_1(2\omega_1-\omega_2)}, \quad (3)$$

whereε_1, ε_2 are the electric field amplitudes of the incident light at frequencies ω_1 and ω_2 respectively. v_F (=10^6 m/s) is the Fermi velocity of graphene. Under the condition that both ω_1 and ω_2 are close to ω, the sheet conductivity can be approximated as:

$$\sigma^{(3)} = \frac{j_e}{\varepsilon_1 \varepsilon_1 \varepsilon_2} = -\frac{9}{32}\frac{e^2}{\hbar}\left(\frac{e v_F}{\hbar \omega^2}\right)^2 , \quad (4)$$

Since most of the sheet current is generated in graphene, the effective nonlinear susceptibility of the whole membrane can be expressed as:

$$\chi^{(3)} = \frac{\sigma^{(3)}}{\omega d} = -\frac{9}{32}\frac{e^4 {v_F}^2}{\hbar^3 c^5}\frac{\lambda^5}{d} , \quad (5)$$

where d is the thickness of the graphene (~1 nm), λ is the wavelength, and c is the speed of light in vacuum. The calculated $\chi^{(3)}$ of a monolayer graphene is in the order of 10^{-7}esu (corresponding to a Kerr coefficient $n_2 \sim 10^{-13}$ m^2/W), at 10^5 times higher than in silicon ($\chi^{(3)} \sim 10^{-13}$esu, $n_2 \sim 4\times10^{-18}$ m^2/W) [7].

Effective n_2 of the hybrid graphene-silicon cavity is then calculated for an inhomogeneous cross-section weighted with respect to field distribution [8] (Fig. 4-2 a-f). With a baseline model without complex graphene-surface electronic interactions, the effective n_2 can be expressed as:

$$\overline{n_2} = \left(\frac{\lambda_0}{2\pi}\right)^d \frac{\int n^2(r) n_2(r)\left(|E(r)\cdot E(r)|^2 + 2|E(r)\cdot E(r)^*|^2\right) d^d r}{\left(\int n^2(r)|E(r)|^2 \, d^d r\right)^2} , \quad (6)$$

where *E(r)* is the complex fields in the cavity and n(r) is local refractive index (Fig. 4-2 g-h). The local Kerr coefficient n_2(r) is 3.8×10^{-18} m^2/W in silicon membrane and ~10^{-13} m^2/W for graphene, λ_0 is the wavelength in vacuum, and d=3 is the number of dimensions. The complex electric field *E(r)* is obtained from Three-dimensional finite-difference

time-domain computations of the optical cavity examined [9]. The resulting field-balanced effective n_2 is calculated to be 7.7×10^{-17} m^2/W ($\chi^{(3)}\sim 10^{-12}$esu), close to the best reported chalcogenide photonic crystal waveguides [10-11]**.**

TABLE 4-1 Field-balanced third-order nonlinear parameter.

Computed parameters	$\overline{n_2}$ (m^2/W)	$\overline{\beta_2}$ (m/W)
Graphene	10^{-13} [6]	10^{-7} [12]
Silicon	3.8×10^{-18}	8.0×10^{-12}
Monolayer graphene-silicon	7.7×10^{-17}	2.5×10^{-11}
Chalcogenide waveguide	7.0×10^{-17}	4.1×10^{-12}

The 3D FDTD method with sub-pixel averaging is used to calculate the real and imaginary parts of the E-field distribution for the cavity resonant mode. The spatial resolution is set at 1/30 of the lattice constant (14 nm). Time-domain coupled mode theory, including free carrier dispersion and dynamics and thermal time constants, is carried out with 1 ps temporal resolution.

Likewise, the effective two-photon absorption coefficient is computed in the same field-balanced approach, with a result of 2.5×10^{-11}m/W. The resulting nonlinear parameter γ ($=\omega n_2/cA_{eff}$) is derived to be 800 $W^{-1}m^{-1}$, for an effective mode area of 0.25 μm^2 (Fig. 4-2 h).

4.3 Device fabrication and calibration

4.3.1 Graphene growth and transferring

Centimeter-scale graphene are grown on 25 μm thick copper foils by chemical vapor deposition of carbon. The top oxide layer of copper is firstly removed in the hydrogen atmosphere (50 mTorr, 1000oC, 2 sccm H_2 for 15 min), then monolayer carbon is formed on copper surface (250 mTorr, 1000oC, 35 sccm CH_4, 2 sccm H_2 for 30 min). The growth is self-limiting once the carbon atom covers the Cu surface catalytic. The single layer graphene is then rapidly cooled down before being moved out of chamber. Poly-methyl-methacrylate (PMMA) is then spun-casted onto the graphene and then the copper foil etch-removed by floating the sample in $FeNO_3$ solution. After the metal is removed, graphene is transferred to a water bath before subsequent transfer onto the photonic crystal membranes. Acetone dissolves the PMMA layer, and the sample is rinsed with isopropyl alcohol and dry baked for the measurements.

4.3.2 Optical calibration by Raman spectrum

A. Raman calibration

Confocal microscopy was used for the graphene Raman spectroscopic measurements with a 100× (numerical aperture at 0.95) objective, pumped with a 514 nm laser.

The Raman spectra are shown in Fig. 4-3. The G and 2D band peaks are excited by a 514 nm laser and are located at 1582 cm^{-1} and 2698 cm^{-1} respectively. The Raman spectra are homogeneous within one device, and vary less than 5 cm^{-1} from sample to sample. The Lorentzian lineshape with full-width half-maximum of the G (34.9 cm^{-1}) and 2D (49.6 cm^{-1}) band indicates the graphene monolayer [13], perhaps broadened by chemical doping and disorder. The phonon transport properties are represented by the G and 2D peak

positions (varying within 1 cm^{-1} over the sample) and the intensity ratios between the G and 2D peaks (fluctuating from 1 to 1.5) [14].

Fig. 4-3 b and c illustrates example transfers of large-area CVD graphene into various substrates including air-bridged silicon membranes, silicon oxide, and partially covered metal surfaces. CVD grown graphene is thicker and has rough surfaces compared to exfoliated graphene, shown by the broadened 2D peak and the fluctuation of the 2D versus G peak ratio [15]. The thickness of graphene is ~ 1 nm. Wrinkles on the graphene surface are formed during the cool down process, due to the differential thermal expansion between the copper substrate and graphene, and consistently appear only at the edges of our samples. We emphasize that at the device regions most of the devices are covered with a single unwrinkled graphene layer.

The 2D peak is observable only when the laser excitation energy (E_L) and the energy corresponding to electron-hole recombination process (E_T) follow the relation: $(E_L-E_T)/2 > E_F$, where E_F is the Fermi energy of graphene. With 514 nm laser excitation, the *2D* peak is located at 2698 cm^{-1} (Fig. 4-3d).

We note that wet transfer of graphene is used in these measurements. While a very thin (in the range of nanometers) residual layer of PMMA can remain on the sample after transfer, PMMA typically only has a non-centrosymmetric $\chi^{(2)}$ response with a negligible $\chi^{(3)}$ response and hence does not contribute to the enhanced four-wave mixing observations. The dopants can arise from residual absorbed molecules or ions on graphene or at the grain boundaries, during the water bath and transfer process.

B. Optical transparency

The Fermi level of graphene can be modified by chemical dopants. Sulfuric acid the nitric acid molecules are physically adsorbed on the surface of graphene without intercalations. The doping level can be well controlled beyond 1eV, for producing graphene with high transparency [16].

In CVD growth graphene preparation, we used $FeNO_3$ as the etchant to remove the copper layer. The NO_3^- molecular in the solution is attached on graphene, and the doping is still there even the sample is left in water for weeks.

With almost all of the undoped samples, the transmission was too low to ascertain good fiber-chip coupling. In addition, in the dry transfer process with solely heating and inter-surface stiction, much contaminants or particles are transferred onto the pristine silicon photonic crystal chip, damaging many of the transmission features. Other than these technicalities, a 11-dB higher power should lead to similar bistability and four-wave mixing properties – however the high power laser might introduce more background Fabry-Perot shifts (modifying the cavity lineshapes) and background noise.

4.3.3 Photonic crystal preparation and transferring

The photonic crystal nanostructures are defined by 248 nm deep-ultraviolet lithography in the silicon CMOS foundry onto undoped silicon-on-insulator (100) substrates. Optimized lithography and reactive ion etching was used to produce device lattice constants of 420 nm, hole radius of 124 ± 2 nm. The photonic crystal cavities and waveguides are designed

and fabricated on a 250 nm silicon device thickness, followed by a buffered hydrofluoric wet-etch of the 1 μm buried oxide to achieve the suspended photonic crystal nanomembranes. The nanoscale Atomic force Microscopy gives the surface topology for the graphene suspended on the periodic holes with200nm. The graphene conductivity superlattice is presented by transferring to the periodically patterned substrate, measured by Electrostatic force microscope (Fig. 4-5).

4.4 Four-wave-mixing in photonic crystal cavity

The four-wave mixing measurements were performed on the in-plane cavity photonic crystal membranes, where a clear four-wave-mixing-generated idler intensity was observed only when graphene is present.

4.4.1 Cavity enhancement of light-matter interaction

The conversion efficiency of the single cavity $\eta=|\gamma P_p L'|^2 FE_p^4 FE_s^2 FE_c^2$, where FE_p, FE_s, and FE_c are the field enhancement factors of pump, signal and idler respectively [17]. The effective length L' includes the phase mismatch and loss effects. Compared to the original cavity length (~ 1582.6 nm), the effective cavity length is only slightly modified by less than 1 nm. However, the spectral dependent field enhancement factor is the square of the cavity build-up factor $FE^2=P_{cav}/P_{wg}=F_{cav}(U/U_{max})\eta_p^2$, where U/U_{max} is the normalized energy distribution with the Lorenzian lineshape. η_p=0.33 is the correction term for the spatial misalignment between the quasi-TE mode and graphene, and the optical field polarization. The field enhancement effect in the cavity is proportional to the photon mode density: $F_{cav}=Q\lambda^3/(8\pi V)$ [18], where Q is the total quality factor; λ is the wavelength of the light; V is the cavity mode volume (Fig. 4-5).

The enhanced two-photon-absorption and induced free-carrier absorption would produce nonlinear loss. To investigate the direct effect of two-photon absorption and free-carrier absorption on the four wave mixing, we measure the conversion efficiency with varying input signal power as shown in Fig. 4-6. Extra 4-dB loss is measured when the input signal power increases from -22 to -10 dBm, with the additional contribution from nonlinear absorption of the graphene-silicon cavity membrane.

4.4.2 Detuning dependence

To examine only the Kerr nonlinearity, next we performed degenerate four-wave mixing measurements on the hybrid graphene – silicon photonic crystal cavities as illustrated in Fig. 4-7, with continuous-wave laser input. A lower-bound Q of 7,500 was specifically chosen to allow a ~ 200 pm cavity linewidth within which the highly dispersive four-wave mixing can be examined. The input pump and signal laser detunings are placed within this linewidth, with matched TE-like input polarization, and the powers set at 600 μW. Two example series of idler measurements are illustrated in Fig. 4-7a and b, with differential pump and signal detunings respectively. In both series the parametric idler is clearly observed as a sideband to the cavity resonance, with the pump detuning ranging -100 pm to 30 pm and the signal detuning ranging from -275 pm to -40 pm, and from 70 pm to 120 pm (shown in Fig. 4-7b). For each fixed signal- and pump-cavity detunings, the generated idler shows a slight intensity roll-off from linear signal (or pump) power dependence when the transmitted signal (or pump) power is greater than ~ 400 μW due to increasing free-carrier absorption effects (Fig. 4-7). As illustrated in Fig. 4-7a and b, the converted

idler wave shows a four-wave mixing 3-dB bandwidth roughly matching the cavity linewidth when the pump laser is centered on the cavity resonance.

A theoretical four-wave mixing model with cavity field enhancement matches with these first graphene-cavity observations. The detuning between the cavity resonance and the laser would decrease the field enhancement factor:

$$F(\lambda) = F(\lambda_{cav}) \frac{1}{1 + 4Q^2 (\frac{\lambda}{\lambda_{cav}} - 1)^2} \tag{7}$$

Based on this numerical model match to the experimental observations, the observed Kerr coefficient n_2 of the graphene-silicon cavity ensemble is 4.8×10^{-17} m^2/W, an order of magnitude larger than in monolithic silicon and GaInP-related materials [19], and two orders of magnitude larger than in silicon nitride [20]. The computed n_2 is at 7.7×10^{-17} m^2/W, matching well with the observed four-wave mixing derived n_2. The remaining discrepancies arise from a Fermi velocity slightly smaller than the ideal values ($\sim 10^6$ m/s) in the graphene. As illustrated in Fig. 4-7d for both measurement and theory, the derived conversion efficiencies are observed up to -30-dB in the unoptimized graphene-cavity, even at cavity *Q*s of 7,500 and low pump powers of 600 μW. The highly-doped graphene with Fermi-level level in the optical transparency region is a pre-requisite to these observations. We note that for a silicon cavity without graphene the conversion efficiencies are dramatically lower (by more than 20-dB lower) as shown in dashed black line, and even below the pump/signal laser spontaneous emission noise ratio (dotted grey line) preventing four-wave mixing observation in a silicon photonic crystal cavity.

Bibliography

[1] Boyd, Robert W. Nonlinear optics. *Academic press*, (2002)

[2] Y. Zhang, Y.-W. Tan , H. L. Stormer, & P. Kim, Experimental observation of the quantum Hall effect and Berry's phase in graphene, *Nature* **438**, 201-204 (2005).

[3] K.F. Mak, M.Y. Sfeir, Y. Wu, C.H. Lui, J.A. Misewich, and T.F. Heinz, Measurement of the Optical Conductivity of Graphene, *Phys. Rev. Lett.* **101**, 196405 (2008).

[4] Q. Bao, H. Zhang, B. Wang, Z. Ni, C. H. Y. X. Lim, Y. Wang, D. Yuan Tang, and K. P. Loh, Broadband graphene polarizer, *Nature Photon.* **5**, 411 (2011).

[5] S. Mikhailov and K. Ziegler, New electromagnetic mode in graphene. *Phys. Rev. Lett.* **99**, 016803 (2007).

[6] E. Hendry, P.J. Hale, J. Moger, and A. K. Savchenko, Coherent nonlinear optical response of graphene, *Phys. Rev. Lett.***105**, 097401 (2010).

[7] M. Dinu, F. Quochi, and H. Garcia, Third-order nonlinearities in silicon at telecom wavelengths, *Appl. Phys. Lett.* **82**, 2954 (2003).

[8] S. Afshar V. and T. M. Monro, A full vectorial model for pulse propagation in emerging waveguides with subwavelength structures part I: Kerr nonlinearity, *Optics Express* **17**, 2298 (2009).

[9] A. F. Oskooi, D. Roundy, M. Ibanescu, P. Bermel, J. D. Joannopoulos, and S. G. Johnson, MEEP: A flexible free-software package for electromagnetic simulations by the FDTD method, *Computer Physics Communications* **181**, 687 (2010).

[10] B. J. Eggleton, B. Luther-Davies and K. Richardson, Chalcogenide photonics, *Nature Photonics* **5**, 141 (2011).

[11] K. Suzuki, Y .Hamachi, and T. Baba, Fabrication and characterization of chalcogenide glass photonic crystal waveguides. *Opt. Express* **17**, 22393 (2009).

[12] A. D. Bristow, N. Rotenberg, and H. M. van Driel, Two-photon absorption and Kerr coefficients of silicon for 850–2200 nm, *Appl. Phys. Lett.* **90**, 191104 (2007).

[13] A. Das, S. Pisana, B. Chakraborty, S. Piscanec, S. K. Saha, U. V. Waghmare, K. S. Novoselov, H. R. Krishnamurthy, A. K. Geim, A. C. Ferrari, and A. K. Sood, Monitoring dopants by Raman scattering in an electrochemically top-gated graphene transistor, *Nature Nanotech.* **3**, 210 (2008); C. Casiraghi, S. Pisana, K. S. Novoselov, A. K. Geim, and A. C. Ferrari, Raman fingerprint of charged impurities in graphene, *Appl. Phys. Lett.* **91**, 233108 (2007).

[14] X. Li, W. Cai, J. An, S. Kim, J. Nah, D. Yang, R. Piner, A. Velamakanni, I. Jung, E. Tutuc, S. K. Banerjee, L. Colombo, and R. S. Ruoff, Large-area synthesis of high-quality and uniform graphene films on copper foils, Science 324, 1312 (2009).

[15] W. Zhao, P. H. Tan, J. Liu, and A. C. Ferrari, Intercalation of few-layer graphite flakes with $FeCl_3$: Raman determination of Fermi level, layer by layer decoupling, and stability, *J. Am. Chem. Soc.* **133**, 5941 (2011).

[16] Zhao, WeiJie, PingHeng Tan, Jun Zhang, and Jian Liu. "Charge transfer and optical phonon mixing in few-layer graphene chemically doped with sulfuric acid." *Physical Review B* **82**, no. 24 (2010): 245423.

[17] P. P. Absil, J. V. Hryniewicz, B. E. Little, P. S. Cho, R. A. Wilson, L. G. Joneckis, and P.-T. Ho, Wavelength conversion in GaAs micro-ring resonators, *Opt. Lett.* **25**, 554 (2000).

[18] R. K. Chang and A. J. Campillo, *Optical processes in microcavities*, World Scientific, Singapore, 1996.

[19] A. M. Pasquazi, M. Peccianti, Y. Park, B. E. Little, S. T. Chu, R. Morandotti an J. Azaña, Sub-picosecond phase-sensitive optical pulse characterization on a chip, *Nature Photon.* **5**, 618 (2011).

[20] F. Wang, Y. Zhang, C. Tian, C. Girit, A. Zettl, M.Crommie, and Y. R. Shen, Gate-variable optical transitions in graphene, *Science* **320**, 206-209 (2008).

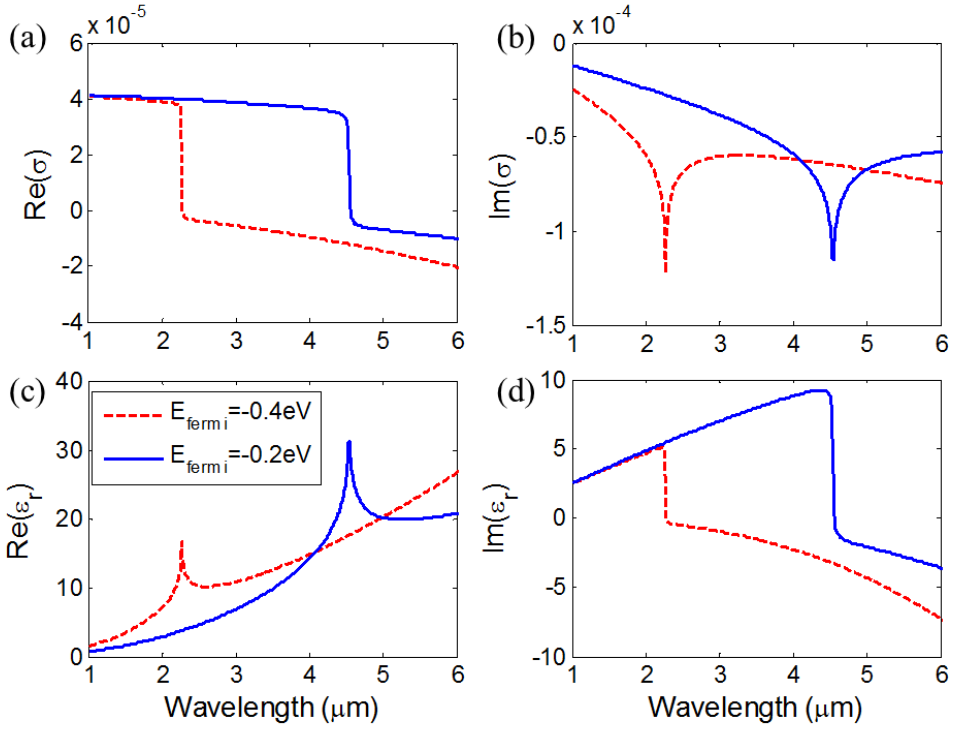

Fig. 4-1 Conductivity and permittivity of graphene in the IR range. (a-b) The real and imaginary parts of the total conductivity; (c-d) permittivity, with Fermi level set at -0.4eV (red dashed line) and -0.2eV (blue solid line) respectively.

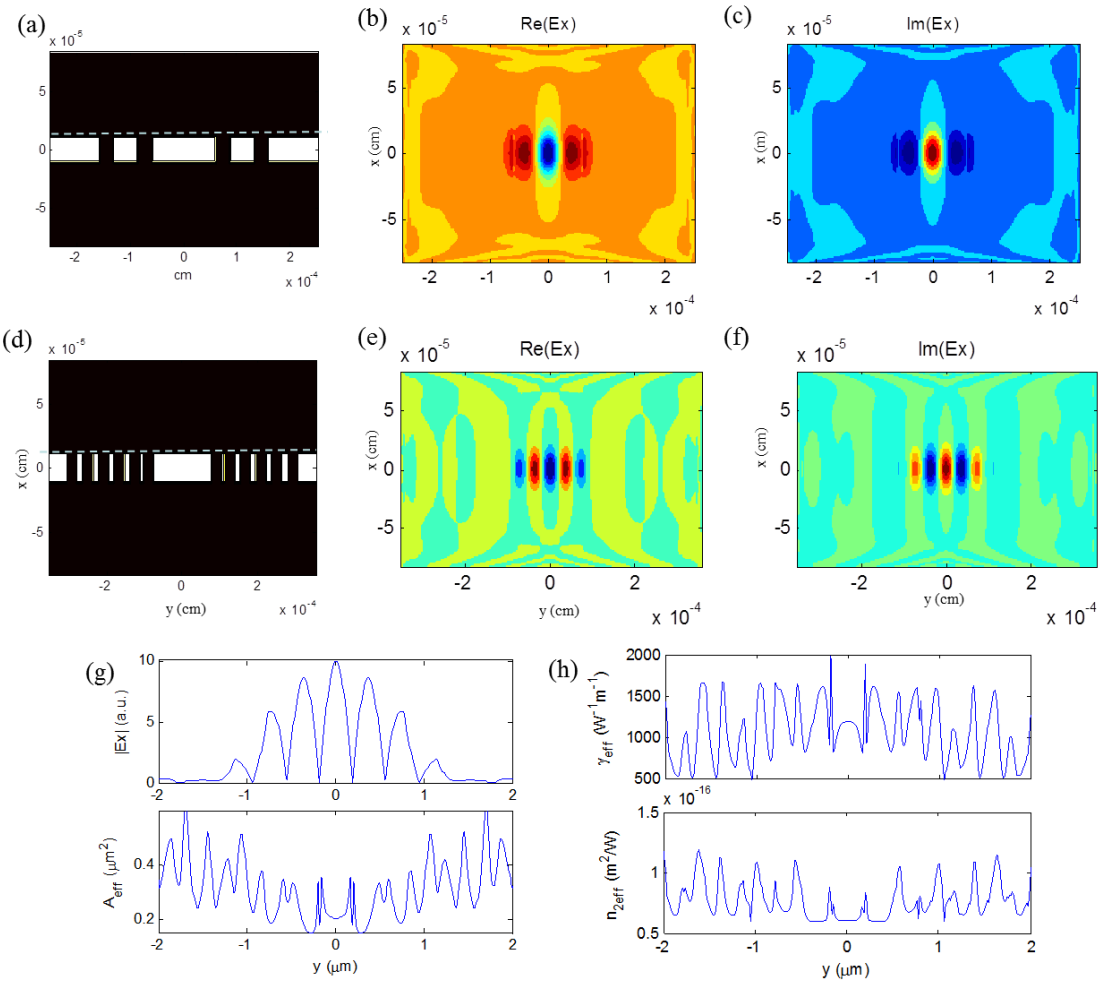

Fig. 4-2 Optical field distribution and calculation for effective kerr nonlinearity of the hybrid graphene-silicon waveguide. (a) The refractive index on the x=0 plane. The white part is the silicon (n=3.45) and the dark part is the air (n=1), (b-c) real and imaginary parts of TE polarized electric field distribution on the across section in (a), (d) The refractive index on the y=0 plane. (e-f) real and imaginary parts of TE polarized electric field in (d).(g) The amplitude of electric field along the cross section of waveguide (upper), and effective area (down) along the waveguide direction. (h) nonlinear parameter γ ($=\omega n_2/cA_{eff}$) and effective kerr coefficient of graphene silicon waveguide.

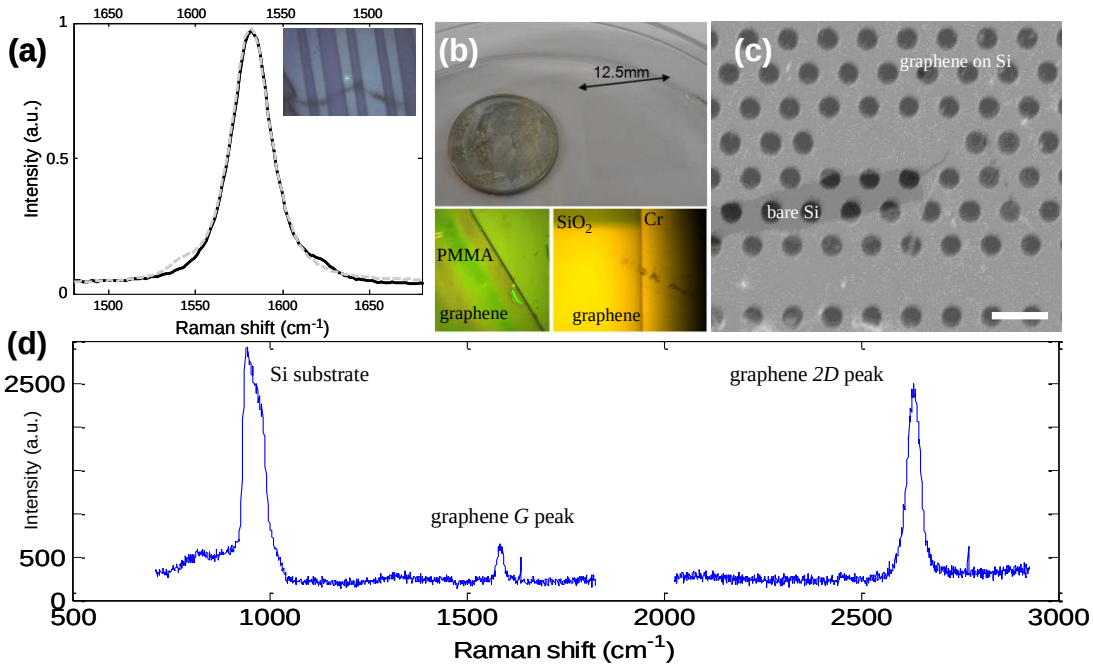

Fig. 4-3 Raman spectrum and transferred graphene samples. (a) Raman G peak (black line) and its inverse (grey dashed line) to illustrate G peak symmetry. Inset: optical micrograph of the device with graphene transferred under Raman measurement. (b) A centimeter-scale graphene film prepared. Optical micrograph of graphene film transferred to various substrates (PMMA), air-bridged silicon membranes, silicon oxide and partially covered metal surfaces, with graphene interface pictured. (c) Scanning electronic micrograph of example air-bridged device sample with graphene covering the whole area except the dark (exposed) region. Scale bar: 500 nm. (d) Complete Raman spectrum of the graphene-clad silicon membrane samples.

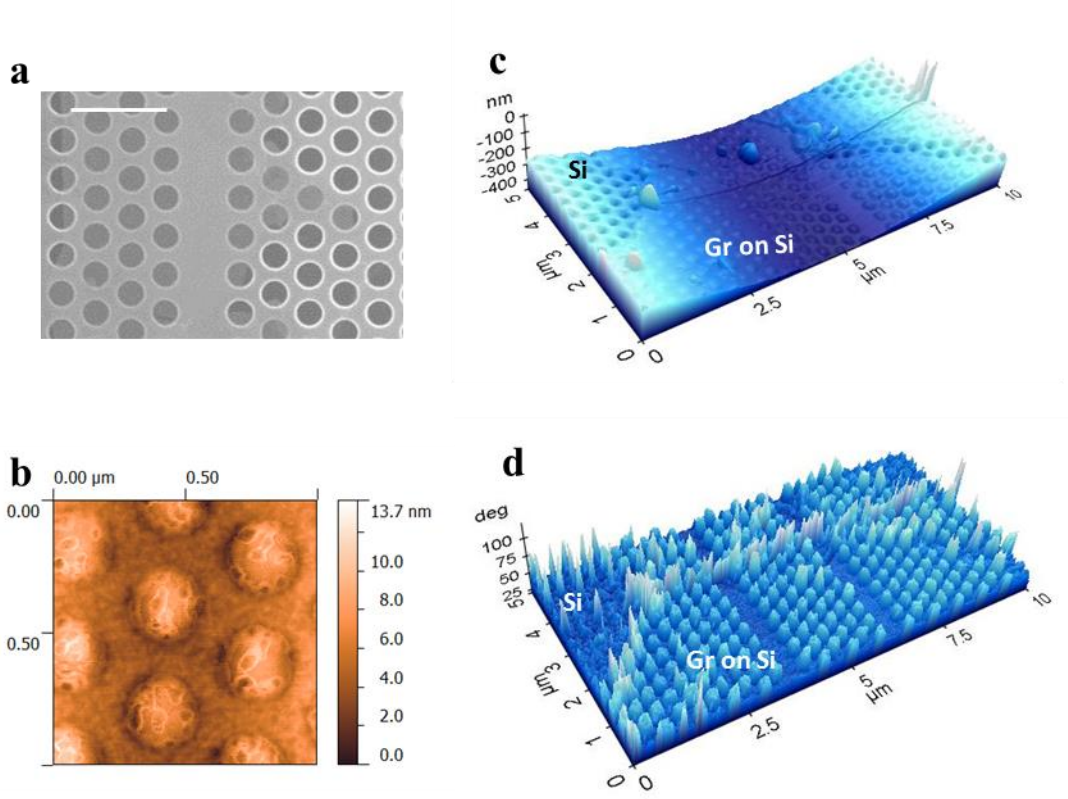

Fig. 4-4. Graphene transferred on patterned 250nm thick suspended silicon membrane. a, SEM of the device. Scale bar: 1μm, **b,** AFM imaged surface topology of 1μm by 1μm **c,** AFM imaged surface topology **c,** AFM imaged surface topology of graphene partially covered on the silicon photonic crystal substrate. **d,** EFM phase mapping imaging the surface conductivity as in **c**. Suspended graphene over the wholes of the silicon shows higher conductivity.

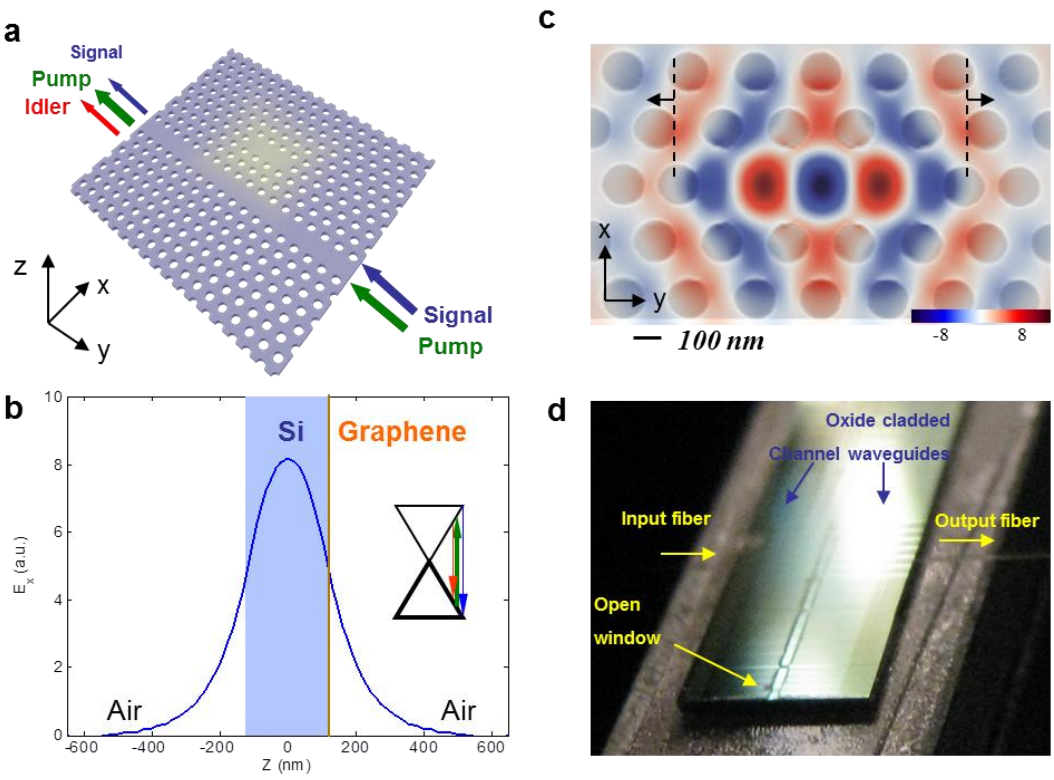

Fig. 4-5 Device layout and measurement. (a) Structure schematic of an L3 cavity switch formed in graphene cladded silicon membrane. (b). The electric field distribution along z direction simulated by FDTD method. The graphene sheet (brown line) is placed on 250nm thick silicon membrane. Inset: Schematics of graphene band diagram with photon energy of pump (green), and converted ones (red and blue) (c). Top view of optic field energy distribution of an isolated S1 shifted L3 cavity. The FDTD simulation of mode profile is superimposed on the SEM picture S1 shifted L3 cavity with graphene cladding, with mode volume: 0.073μm^3, and quality factor ~2.0×10^4 Scale bar: 100nm. (d). CMOS processed integrated optical devices under test. The open window is for silicon membrane undercut and graphene cladding on the photonic crystal part.

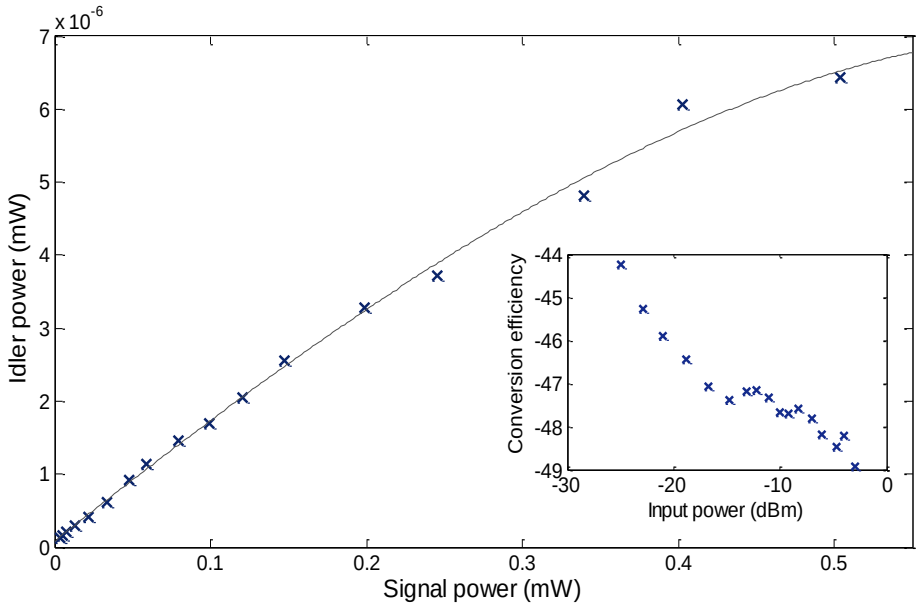

Fig. 4-6 Free-carrier absorption effects on the four-wave mixing conversion efficiency. Measured idler power versus signal power at the transmitted port, with the pump power is fixed on the cavity resonance and the the signal laser detuned by 200 pm. Experimental data (×) and quadratic fit (solid line). Inset: corresponding conversion efficiency versus signal power.

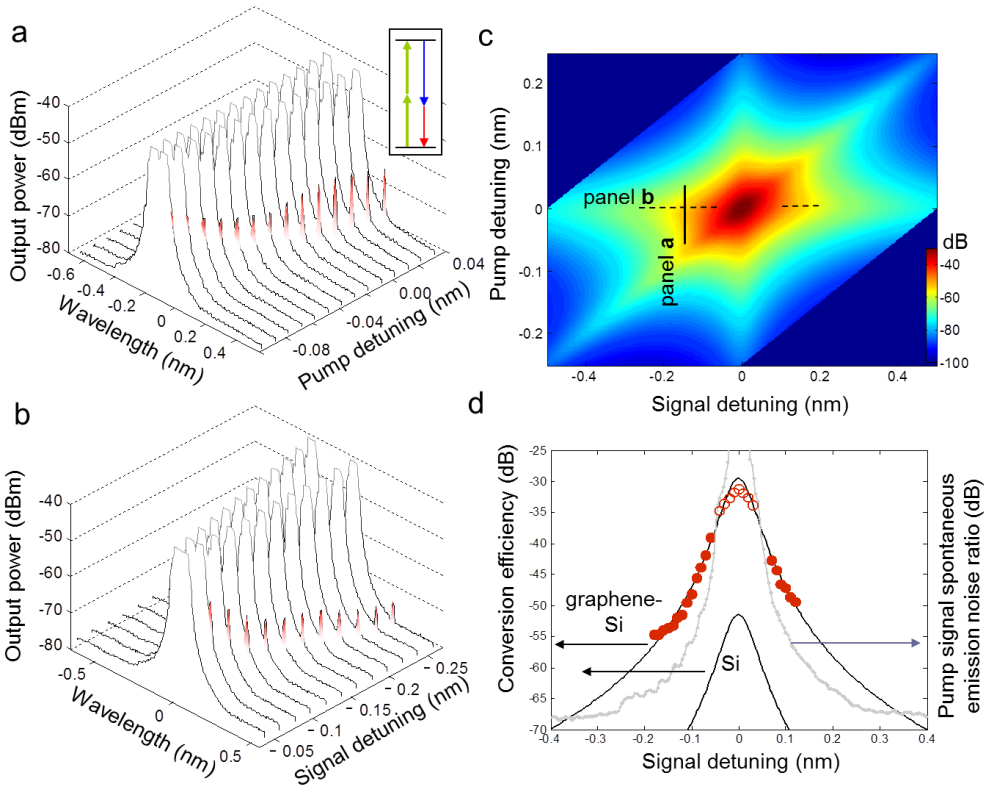

Fig. 4-7 Parametric four-wave mixing in graphene-cladded silicon nanocavities. (a) Measured transmission spectrum with signal laser fixed at -0.16 nm according to cavity resonance, and pump laser detuning is scanned from -0.1 to 0.03 nm. Inset: band diagram of degenerate four-wave mixing process with pump (green), signal (blue) and idler (red) lasers. (b) Measured transmission spectrum with pump laser fixed on cavity resonance, and signal laser detuning is scanned from -0.04 to -0.27 nm. (c) Modeled conversion efficiency versus pump and signal detuning from the cavity resonance. (d) Observed and simulated conversion efficiencies of the cavity. Red solid dots are measured with signal detuning as in panel b, and the empty circles are obtained through pump detuning as in panel a, plus 29.5-dB (offset due to the 0.16 nm signal detuning). Solid and dashed black lines are modeled conversion efficiencies of graphene-silicon and monolithic silicon

cavities respectively. Grey dashed line (superimposed): illustrative pump/signal laser spontaneous emission noise ratio.

Chapter 5

Free carrier dynamics in graphene-silicon resonator

5.1 Introduction

Silicon based subwavelength structure enables realization of chip-scale optoelectronic modulators [1-4], photoreceivers [5-6], and high-bitrate signal processing architectures [7-8]. Coupled with ultrafast nonlinearities as a new parameter space for optical physics [9], breakthroughs such as resonant four-wave mixing [10] and parametric femtosecond pulse characterization [11-12] have been described. Recently, graphene – with its broadband dispersionless nature and large carrier mobility – has been examined for its gate-variable optical transitions [13-14] towards broadband electroabsorption modulators [15] and photoreceivers [16-17] including planar microcavity-enhanced photodetectors [18-19], as well as saturable absorption for mode-locking [20]. Due to its linear band structure allowing interband optical transitions at all photon energies, graphene has been suggested as a material with large $\chi^{(3)}$ nonlinearities [21]. In this chapter we demonstrate the two photon absorption of graphene in a wavelength-scale localized photonic crystal cavity, enabling ultralow power optical bistable switching, self-induced regenerative oscillations, and coherent four-wave mixing at femtojoule cavity energies on the semiconductor chip platform (Fig. 5-1). The structure examined is a hybrid graphene-silicon cavity (as illustrated in Fig. 5-2), achieved by rigorous transfer of monolayer large-area graphene sheet onto air-bridged silicon photonic crystal nanomembranes with minimal linear absorption and optimized optical input/output coupling. This optoelectronics demonstration is complemented with recent examinations of large-area [22-23] graphene field-effect transistors and analog circuit designs [24] for potential large-scale silicon integration.

5.2 Two photon absorption

5.2.1 Effective two photon absorption in graphene-Si system

With increasing input power, the transmission spectra evolve from symmetric Lorentzian to asymmetric lineshapes as illustrated in the examples of Fig 5-2b and Fig. 5-3 a-b. Through second-order perturbation theory [25], the two-photon absorption coefficient β_2 in monolayer graphene is estimated through the second-order interband transition probability rate per unit area as:

$$\beta_2 = \frac{4\pi^2}{\varepsilon_\omega \omega^4 \hbar^3}\left(\frac{v_F e^2}{c}\right)^2 , \qquad (1)$$

where v_F is the Fermi velocity, $\hbar$ is the reduced Planck's constant, e is the electron charge, and ε_ω is the permittivity of graphene in the given frequency. At our 1550 nm wavelengths, β_2 is determined through *Z*-scan measurements and first-principle calculations to be in the range of ~ 3,000 cm/GW [25].

The effective two-photon absorption coefficient of graphene on silicon is defined as:

$$\overline{\beta_2} = (\frac{\lambda_0}{2\pi})^d \frac{\int n^2(r)\beta_2(r)(|E(r)\cdot E(r)|^2 + 2|E(r)\cdot E(r)^*|^2)d^d r}{(\int n^2(r)|E(r)|^2 d^d r)^2}, \qquad (2)$$

The two-photon absorption coefficients of the hybrid cavity calculated from 3D finite-difference time-domain field averages.

With the same CVD growth process, we also examined the dry transfer technique which controls the doping density to be low enough such that the Fermi level is within the interband optical transition region. In that case, the measured samples have a significantly increased propagation loss from ~0dB to ~ 11 dB over the 120 μm length photonic crystal

waveguide. The wet transfer technique significantly reduced the linear absorption, thereby allowing the various nonlinear optoelectronic measurements observed in this work.

5.2.2 Parameter space of nonlinear optics in graphene nanophotonics

Comparing the cavity-based switching and modulation across different platforms including silicon, III-V and the hybrid graphene- silicon cavities examined in this work. The thermal or free-carrier plasma-based switching energy is given by $P_{0th/e} \times \tau_{th/e}$, where $P_{0th/e}$ is the threshold laser power required to shift the cavity resonance half-width through thermal or free-carrier dispersion; $\tau_{th/e}$ are the thermal and free-carrier lifetimes in resonator. Note that the lifetime should be replaced by cavity photon lifetime if the latter is larger (for high Q cavity). Graphene brings about a lower switching energy due to strong two-photon absorption (~3,000 cm/GW) [25]. The recovery times of thermal switching (in red) are also shortened due to higher thermal conductivity in graphene, which is measured for supported graphene monolayers at 600 W/mK [26] and bounded only by the graphene-contact interface and strong interface phonon scattering.

TABLE 5-1 **Estimated physical parameters from time-dependent coupled-mode theory-experimental matching, three-dimensional numerical field simulations, and measurement data.**

Parameter	Symbol	GaAs [S17]	Si	Monolayer Graphene-Si
TPA coefficient	β_2 (cm/GW)	10.2	1.5 [S27]	25[3D]
Kerr coefficient	n_2 (m^2/W)	1.6×10-17	0.44×10^{-17} [27]	7.7×10^{-17} [3D]
Thermo-optic coeff.	dn/dT	2.48×10-4	1.86×10^{-4}	
Specific heat	$c_v\rho$(W/Km^{-3})	1.84×106	1.63×10^6 [cal]	
Thermal relaxation time	$\tau_{th,c}$ (ns)	8.4	12	10 [cal]
Thermal resistance	R_{th} (K/mW)	75	25 [28]	20 [cal]
FCA cross section	σ ($10^{-22}m^3$)	51.8	14.5	
FCD parameter	ζ ($10^{-28}m^3$)	50	13.4	

Carrier lifetime	τ_{fc} (ps)	8	500 [29]	200 [CMT]
Loaded Q	Q	7000	7000 [m]	
Intrinsic Q	Q_0	30,000	23,000 [m]	

[CMT]: nonlinear time-dependent coupled-mode theory simulation; [3D]: three-dimensional numerical field calculation averages; [m]: measurement at low power; [cal]: first-order hybrid graphene-silicon media calculations. τ_{fc} is the effective free-carrier lifetime accounting for both recombination and diffusion.

The switching energy is inversely proportional to two photon absorption rate (β_2). Table 5-1 below summarizes the first-order estimated physical parameters from: (1) coupled-mode theory and experimental data matching; (2) full three-dimensional numerical field simulations, and (3) directly measured data. With the enhanced two-photon absorption in graphene and first-order estimates of the reduced carrier lifetimes, the switching transmission lineshape of different power of the hybrid graphene-silicon cavity is illustrated in Figure 4-2, compared to monolithic GaAs or silicon ones.

5.3 Graphene thermal and free-carrier nonlinearities

5.3.1 Steady state response of graphene-Si cavity

A. Optical bistability

We track the *L3* cavity resonance in the transmission spectra with different input powers as illustrated in Fig. 5-3. With thermal effects, the cavity resonance red-shifts 1.2 nm/mW for the graphene-clad sample (Q ~ 7,000) and only 0.3 nm/mW for silicon sample (similar Q ~ 7,500). The thermal red-shift is sizably larger in the graphene-clad sample versus a near-identical monolithic silicon cavity. In addition, Figure 5-3 d shows the tuning efficiency for a range of cavity Qs examined in this work – with increasing Q the

monolithic silicon cavity shows an increase in tuning efficiency while the converse occurs for the graphene-silicon cavity. Fig. 5-4 shows the steady-state bistable hysteresis for more detunings, and Fig. 5-5 shows the temporal switching with illustrative detunings of -0.8 and 0.6 nm.

B. Hysteresis loop

5.3.1.B.1 One cavity bistable switch

The insertion loss at 0.4-nm seems negligible between the graphene-cladded and bare sample, but this is because of the slight increased Fabry-Perot resonances after the graphene transfer. The Fabry-Perot resonances (from finite reflections in the waveguide) give rise background spectral oscillations that increases or decreases the transmission of the waveguide (Fig. 5-1b). To accurate determine the additional ~ 1-dB or less excess loss from graphene cladded over the short photonic crystal sample, we compared the transmission spectra between with and without graphene. Independently, we also note that for heavily-doped graphene the linear absorption is 0.02-dB/um (while at 0.1-dB/um for intrinsic graphene).

With coupled-mode theory, the dynamic equation for the amplitude of the resonance mode are described by coupled mode theories. Due to the partial reflection from the faclets of the waveguide, a Fabry-Perod mode is formed in the waveguide, and coupled to the cavity mode [30]. The interference is weak when the extinction ratio of the cavity is large (~10dB), but the cavity resonance shift due to interference is more significant with decreased extinction ratio at high power induced by nonlinear effect. From curve-fitting the transmission spectrum at low power (linear region), we obtained that waveguide facelet reflectivity 0.12 waveguide length 2mm. We fix the reflectivity and plot the

transmission spectrum at five different power levels, and observed maximum 0.05nm variation of the cavity resonance shift due to different phase between waveguide and cavity at input power 0.6mW (Figure 5-2 a-b).

The intrinsic $Q_{intrinsic}$ and loaded Q_{loaded} are 22,000 and 7,500 respectively. The total Q obtained from the transmission spectral linewidth is related to the loaded and intrinsic Qs through the relation: $1/Q=1/Q_{loaded}+1/Q_{intrinsic}$. The loaded and intrinsic Qs denote respectively the photon decay rates of the cavity into the coupling waveguide and into the free-space continuum. Q_{loaded} is less than 1/3 of $Q_{intrinsic}$ here (from design simulations), and thus roughly estimated to be the same as the total Q: $Q_{loaded} = \omega_0/\Delta\omega$, where ω_0 is the cavity resonance frequency, and $\Delta\omega$ is the cavity linewidth. The Qs are calibrated at low input powers, and also matched with our nonlinear coupled mode theory models. After knowing Q_{loaded}, $Q_{intrinsic}$ can be derived from $Q_{intrinsic} = Q_{loaded} / \sqrt{T}$ for a side-coupled cavity, where T is the normalized transmittance of laser power when its wavelength is set on the cavity resonance..

The cavity energy is a measure of the internal cavity energy that would be lost if the external continuous-wave laser is turned off rapidly; it is a measure used in switching and dynamical studies [31-32]. The formal definition of the intrinsic cavity energy U_c is $U_c= Q_{intinsic}P_l/\omega$, where P_l is the power loss from the cavity and ω is the excitation frequency [33]. For our side-coupled cavity in transmission, $U_c= Q_{intinsic}(1-T_{min})P_{in}/\omega$, where T_{min} is the minimum transmission and P_{in} the coupled input power, which gives the femtojoule per cavity switching energies.

5.3.1.B.2 Multi-stability in coupled cavity system

The master equation for the dynamics of two side-coupled cavity system is as follow.

$$\frac{da_n}{dt} = [-\frac{1}{2\tau_{total,n}} + i(\omega_n + \Delta\omega_n - \omega_{wg})]a_n + \kappa S_{R(n-1)} + \kappa S_{Ln} \quad (4)$$

$$\frac{dN}{dt} = \frac{1}{2\hbar\omega_0\tau_{TPA}}\frac{V_{TPA}}{V_{FCA}{}^2}|a|^4 - \frac{N}{\tau_{fc}} \quad , \quad (5)$$

$$\frac{d\Delta T}{dt} = \frac{R_{th}}{\tau_{th}\tau_{FCA}}|a|^2 + \frac{\Delta T}{\tau_{th}} \quad , \quad (6)$$

where n is the cavity number, ω is the resonant frequency, a is the normalized cavity mode amplitude, and s is the normalized waveguide mode amplitude. $\gamma=1/(2\zeta_t)$ is the total cavity loss rate, including the power dissipation by radiation and coupling to waveguide. ζ_t is the total cavity lifetime. $\kappa = i\exp(-i\phi/2)/\sqrt{2\tau_c}$ is the coupling coefficient between cavity and waveguide, where $\phi = \omega_{wg} n_{eff} L/c$ is the phase difference between two cavities (Figure 5-4 c-d).

5.3.2 Bistable switching dymanics

To verify the bistable switching dynamics, we input time-varying intensities to the graphene-cladded cavity, allowing a combined cavity power – detuning sweep. Figure 5-4a shows an example time-domain output transmission for two different initial detunings [$\delta_{(t=0)}$ = -1.3 and $\delta_{(t=0)}$ = 1.6] and for an illustrative triangular-waveform drive, with nanosecond resolution on an amplified photoreceiver (Figure 5-4c). With the drive period at 77 ns, the observed thermal relaxation time is ~ 40 ns. Cavity resonance dips (with modulation depths ~ 3-dB in this example) are observed for both positive detuning (up to 0.34 nm, δ = 1.4) and negative detuning (in the range from -0.15 nm (δ = - 0.75) to -0.10 nm (δ = - 0.5)). The respective two-state high- and low-state transmissions are illustrated in the inset of Fig 5-4 a-b, for each switching cycle. With the negative detuning and the

triangular pulses, the carrier-induced (Drude) blue-shifted dispersion overshoots the cavity resonance from the drive frequency and then thermally pins the cavity resonance to the laser drive frequency. Since the free carrier lifetime of the hybrid media is about 200 ps and significantly lower than the drive pulse duration, these series of measurements are thermally dominated; the clear (attenuated) resonance dips on the intensity up-sweeps (down-sweeps) are due to the measurement sampling time shorter than the thermal relaxation timescale and a cooler (hotter) initial cavity temperature.

5.3.3 Regenerative oscillation

When the input laser intensity is well above the bistability threshold, the graphene-cavity system deviates from the two-state bistable switching and becomes oscillatory as shown in Fig. 5-5. Regenerative oscillation has only been suggested in a few prior studies, such as theoretically predicted in GaAs nanocavities with large Kerr nonlinearities [34] or observed in high-Q (3×10^5) silicon microdisks [35]. These regenerative oscillations are formed between the competing phonon and free carrier populations, with slow thermal red-shifts (~ 10 ns timescales) and fast free-carrier plasma dispersion blue-shifts (~ 200 ps timescales) in the case of our graphene-silicon cavities. The self-induced oscillations across the drive laser frequency are observed at threshold cavity powers of 0.4 mW, at ~ 9.4 ns periods in these series of measurements which gives ~ 106 MHz modulation rates, at experimentally-optimized detunings from $\delta_{(t=0)}$ = 0.68 to 1.12. We emphasize that, for a monolithic silicon *L3* cavity, such regenerative pulsation has not been observed nor predicted to be observable at a relatively modest Q of 7,500, and attenuated by significant nonlinear absorption.

Fig. 5-6a shows the input-output intensity cycles constructed from the temporal response measurements of a triangular-wave modulated 1.2 mW laser with a 2 μs cycle. Clear bistability behavior is seen below the carrier oscillation threshold. The system transits to the regime of self-sustained oscillations as the power coupled into the cavity is above the threshold, by tuning the laser wavelength into cavity resonance. We show an illustrative numerical modeling in Fig. 5-6: the fast free-carrier response fires the excitation pulse (blue dashed line; start cycle)), and heat diffusion (red solid line) with its slower time constant determines the recovery to the quiescent state in the graphene-cladded suspended silicon membrane. The beating rate between the thermal and free carrier population is around 50 MHz, as shown in the inset of Fig. 5-4a, with the matched experimental data and coupled-mode theory simulation. The beating gives rise to tunable peaks in the radio frequency spectra, which are absent when the input power is below the oscillation threshold (grey dashed line). We note that the model does not include a time varying cavity quality factor, considering the high power would usually broaden the cavity bandwidth.

The high two photon absorption in graphene-silicon hybrid system generates large free carrier dispersion (negative cavity resonance shift), and the thermal dispersion from the free carrier recombination (positive cavity resonance shift). Either of the processes is demonstrated to show optical bistability in silicon [36-37]. The free carrier dispersion dominants the carrier resonance shift at first several seconds while the thermal dispersion dominants the long term response (c.w. input as in Fig. 5-2b). In Fig. 5-5, we scan the cavity response in time domain, and the input triangular pulse width is set to make both free carrier and thermal bistability observable. It is emphasized that the role of graphene

here is enhancing the nonlinear absorption, induced free carrier population, decreased thermal relaxation time, thermal resistance, and carrier lifetime, while the dispersion effects are similar to monolithic silicon (parameters explicit the in Table 5-1). The combination of the system parameter set gives the unique properties of the graphene-silicon cavity.

To further illustrate the cavity response to the laser set at red and blue detuning, the output power from cavity to step input at different detuning is simulated and shown in Fig. 5-5. The switching on/off ratio, defined as the output power at time zero versus the power intensity when the cavity is switched on resonance. The on/off ratio is observed to be strongly dependent on laser detuning, both in simulation and experiment.

A. Time domain coupled mode theory

From the nonlinear coupled-mode modeling, the dynamical responses of the hybrid cavity to step inputs are shown in Figure 5-7a, illustrating the switching dynamics and regenerative oscillations. Free-carrier dispersion causes the switching on the negative-detuned laser, and the thermal nonlinearity leads to the switching on the positive side. The interplay of the free-carrier-induced cavity resonance blue-shift dynamics with the thermal-induced cavity red-shift time constants is observed. Fig. 5-7b shows the correspondent radio frequency spectrum. By tuning the laser wavelength, the fundamental mode can be set from 48 MHz (zero detuning) to 55 MHz (0.3 nm detuning). The dependence of oscillation period to the detuning and input laser power is further provided in Fig. 5-7c and Fig. 5-7d respectively.

We model the nonlinear cavity transmissions with time-domain nonlinear coupled -mode theory for the temporal rate evolution of the photon, carrier density and temperatures as

described by [38]:

$$\frac{da}{dt} = (i(\omega_L - \omega_0 + \Delta\omega) - \frac{1}{2\tau_t})a + \kappa\sqrt{P_{in}} \quad , \tag{7}$$

$$\frac{dN}{dt} = \frac{1}{2\hbar\omega_0\tau_{TPA}}\frac{V_{TPA}}{V_{FCA}^2}|a|^4 - \frac{N}{\tau_{fc}} \quad , \tag{8}$$

$$\frac{d\Delta T}{dt} = \frac{R_{th}}{\tau_{th}\tau_{FCA}}|a|^2 + \frac{\Delta T}{\tau_{th}} \quad , \tag{9}$$

where a is the amplitude of resonance mode; N is the free-carrier density; ΔT is the cavity temperature shift. P_{in} is the power carried by incident continuous-wave laser. κ is the coupling coefficient between waveguide and cavity, adjusted by the background Fabry-Perot resonance in waveguide [39]. ω_L-ω_0 is the detuning between the laser frequency (ω_L) and cold cavity resonance (ω_0). The time-dependent cavity resonance shift is $\Delta\omega=\Delta\omega_N-\Delta\omega_T+\Delta\omega_K$, where the free-carrier dispersion is $\Delta\omega_N=\omega_0\zeta N/n$.The thermal induced dispersion is $\Delta\omega_T=\omega_0\Delta T(dn/dT)/n$. $\Delta\omega_K$ is the Kerr dispersion, and is negligibly small compared to the thermal and free-carrier mechanisms.

The total loss rate is $1/\tau_t= 1/\tau_{in}+1/\tau_v+1/\tau_{lin}+1/\tau_{TPA}+1/\tau_{FCA}$. $1/\tau_{in}$ and $1/\tau_v$is the loss rates into waveguide and vertical radiation into the continuum, ($1/\tau_{in/v} =\omega/Q_{in/v}$), the linear absorption $1/\tau_{lin}$for silicon and graphene are demonstrated to be small. The free-carrier absorption rate $1/\tau_{FCA}=c\sigma N(t)/n$. The field averaged two-photon absorption rate$1/\tau_{TPA}=\overline{\beta_2}$ $c^2/n^2/V_{TPA}|a|^2$.

The mode volume for two-photon absorption (same as Kerr):

$$V_{TPA/Kerr} = \frac{(\int n^2(r)|A(r)|^2\,dr^3)^2}{\int_{Si} n^4(r)|A(r)|^4\,dr^3} \quad , \tag{10}$$

The effective mode volume for free-carrier absorption is:

$$V^2_{FCA} = \frac{(\int n^2(r)\,|A(r)|^2\,dr^3)^3}{\int_{Si} n^6(r)\,|A(r)|^6\,dr^3} \quad . \tag{11}$$

The model shows remarkable match to the measured transmissions. With the first-order estimates of the thermal properties (specific heat, effective thermal resistance, and relaxation times), the carrier lifetime of the graphene-clad photonic crystal cavity is estimated to first-order at 200 ps.

B. Graphene-silicon cavity and High *Q* photonic crystal cavity

Regenerative oscillations were theoretically predicted in GaAs nanocavities with large Kerr nonlinearities [40], or observed only in high-*Q* silicon microdisks (*Q* at 3×10^5) with *V* at $40(\lambda/n_{Si})^3$, at sub-mW power levels [41]. The graphene-enhanced two-photon absorption, free-carrier and thermal effects allow regenerative oscillations to be experimentally observable with Q^2/V values [of $4.3\times10^7(\lambda/n)^3$] at least 50× lower, at the same power threshold levels [42]. The regenerative oscillations with lower *Q*s allow higher speed and wider bandwidth operation, and are less stringent on the device nanofabrication.

We also show new measurement plots of the self-induced regenerative oscillations at different detunings and also numerical model of the two-state switching and oscillation for a large range of detunings (Fig. 5-8).

5.4 Conclusion

This chapter concludes graphene-silicon hybrid optoelectronic devices operating at a few femtojoule cavity recirculating energies: (1) ultralow power resonant optical bistability; (2) self-induced regenerative oscillations. All These observations, in comparison with

control measurements on solely monolithic silicon cavities, are enabled only by the dramatically-large and ultrafast $\chi^{(3)}$ nonlinearities in graphene and the large *Q/V* ratios in wavelength-localized photonic crystal cavities. These nonlinear results demonstrate the feasibility and versatility of hybrid two-dimensional graphene-silicon nanophotonic devices for next-generation chip-scale high-speed optical communications, radio-frequency optoelectronics, and all-optical signal processing.

Bibliography

[1] Q. Xu, B. Schmidt, S. Pradhan and M. Lipson, Micrometre-scale silicon electro-optic modulator, *Nature* **435**, 325-327 (2005).

[2] A. Liu, R. Jones, L. Liao, D. Samara-Rubio, D. Rubin, O. Cohen, R. Nicolaescu, and M. Paniccia, A high-speed silicon optical modulator based on a metal-oxide-semiconductor capacitor, *Nature* **427**, 615-618 (2005);

[3] J. Liu, M. Beals, A. Pomerene, S. Bernardis, R. Sun, J. Cheng, L. C. Kimerling, and J. Michel., Waveguide-integrated, ultralow-energy GeSi electro-absorption modulators, *Nature Photon.* **2**, 433-437 (2008).

[4] Y.-H. Kuo, Y. K. Lee, Y. Ge, S. Ren, J. E. Roth, T. I. Kamins, D. Miller, and J. S. Harris, Strong quantum-confined Stark effect in germanium quantum-well structures on silicon, *Nature* **437**, 1334-1336 (2005).

[5] S. Assefa, F. Xia, and Y. A. Vlasov, Reinventing germanium avalanche photodetector for nanophotonic on-chip optical interconnects, *Nature* **464**, 80-84 (2010).

[6] Y. Kang, H.-D. Liu, M. Morse, M. J. Paniccia1, M. Zadka, S. Litski, G. Sarid, A. Pauchard, Y.-H. Kuo, H.-W. Chen, W. S. Zaoui, J. E. Bowers, A. Beling, D. C. McIntosh, X. Zheng and J. C. Campbell, Monolithic germanium/silicon avalanche photodiodes with 340 GHz gain–bandwidth product, *Nature Photon.* **3**, 59-63 (2009).

[7] A. Biberman, S. Manipatruni, N. Ophir, L. Chen, M. Lipson, and K. Bergman, First demonstration of long-haul transmission using silicon microring modulators, *Opt. Express* **18**, 15544-15552 (2010).

[8] M. Pelusi., F. Luan, T. D. Vo, M. R. E. Lamont, S. J. Madden, D. A. Bulla, D.-Y. Choi, B. Luther-Davies and B. J. Eggleton, Photonic-chip-based radio-frequency spectrum

analyser with terahertz bandwidth, *Nature Photon.* **3**, 139-143 (2009).

[9] P. Colman, C. Husko, S. Combrié, I. Sagnes, C. W. Wong and A. De Rossi, Temporal solitons and pulse compression in photonic crystal waveguides, *Nature Photon.* **4**, 862-868 (2010).

[10] F. Morichetti, A. Canciamilla, C. Ferrari, A. Samarelli, M. Sorel and A. Melloni, Travelling-wave resonant four-wave mixing breaks the limits of cavity-enhanced all-optical wavelength conversion, *Nature Commun.* **2**, 1-8 (2011).

[11] M. A. Foster, R. Salem, D. F. Geraghty, A. C. Turner-Foster, M. Lipson and A. L. Gaeta, Silicon-chip-based ultrafast optical oscilloscope, *Nature* **456**, 81-84 (2008).

[12] A. Pasquazi, M. Peccianti, Y. Park, B. E. Little, S. T. Chu, R. Morandotti, J. Azaña and D. J. Moss, Sub-picosecond phase-sensitive optical pulse characterization on a chip, *Nature Photon.* **5**, 618 (2011).

[13] F. Wang, Y. Zhang, C. Tian, C. Girit, A. Zettl, M. Crommie, Y. Ron Shen, Gate-variable optical transitions in graphene, *Science* **320**, 206-209 (2008).

[14] Z. Q. Li, E. A. Henriksen, Z. Jiang, Z. Hao, M. C. Martin, P. Kim, H. L. Stormer and D. N. Basov, Dirac charge dynamics in graphene by infrared spectroscopy, *Nature Phys.* **4**, 532-535 (2008).

[15] M. Liu, X. Yin, E. Ulin-Avila, B. Geng, T. Zentgraf, L. Ju, F. Wang and X. Zhang, A graphene-based broadband optical modulator, *Nature* **474**, 64-67 (2011).

[16] T. Mueller, F. Xia, and P. Avouris, Graphene photodetectors for high-speed optical communications, *Nature Photon.* **4**, 297-301 (2010).

[17] F. Xia, T. Mueller, Y.-M. Lin, A. Valdes-Garcia1 and P. Avouris, Ultrafast graphene photodetector, *Nature Nanotech.* **4**, 839-843 (2009).

[18] M. Engel, M. Steiner, A. Lombardo, A. C. Ferrari, H. v. Löhneysen, P. Avouris and R. Krupke, Light-matter interaction in a microcavity-controlled graphene transistor, *Nature Communications* **3**, 906 (2011).

[19] M. Furchi, A. Urich, A. Pospischil, G. Lilley, K. Unterrainer, H. Detz, P. Klang, A. M. Andrews, W. Schrenk, G. Strasser, and T. Mueller, Microcavity-integrated graphene photodetector, *Nano Lett.* **12**, 2773 (2011).

[20] Z. Sun, T. Hasan, F. Torrisi, D. Popa, G. Privitera, F. Wang, F. Bonaccorso, D. M. Basko and A. C. Ferrari, Graphene mode-locked ultrafast laser, *ACS Nano* **4**, 803-810 (2010).

[21] E. Hendry, P. J. Hale, J. Moger, A. K. Savchenko and S. A. Mikhailov, Coherent nonlinear optical response of graphene, *Phys. Rev. Lett.* **105**, 097401 (2010).

[22] X. Li, W. Cai, J. An, S. Kim, J. Nah, D. Yang, R. Piner, A. Velamakanni, I. Jung, E. Tutuc, S. K. Banerjee, L. Colombo, R. S. Ruoff, Large-area synthesis of high-quality and uniform graphene films on copper foils, *Science* **324**, 1312-1314 (2009).

[23] S. Bae, H. Kim, Y. Lee, X. Xu, J.-S. Park, Y. Zheng, J. Balakrishnan, T. Lei, H. R. Kim, Y. II Song, Y.-J. Kim, K. S. Kim, B. Özyilmaz, J.-H. Ahn, B. H. Hong and S. Iijima, Roll-to-roll production of 30-inch graphene films for transparent electrodes, *Nature Nanotech.* **5**, 574-578 (2010).

[24] Y.-M. Lin, A. Valdes-Gacia, S.-J. Han, D. B. Farme, I. Meric, Y. Sun, Y. Wu, C. Dimiraakopulos, A. Grill, P. Avouris, K. A. Jenkins, Wafer-scale graphene integrated circuit, *Science* **332**, 1294-1297 (2011).

[25] H. Yang, X. Feng, Q. Wang, H. Huang, W. Chen, A. T. S. Wee, and W. Ji, Giant two-photon absorption in bilayer graphene, *Nano Lett.* **11**, 2622 (2011).

[26] J. H. Seol, I. Jo, A. L. Moore, L. Lindsay, Z. H. Aitken, M. T. Pettes, X. Li, Z. Yao, R. Huang, D. Broido, N. Mingo, R. S. Ruoff, and L. Shi, Two-dimensional phonon transport in supported graphene, *Science* **328**, 213 (2010).

[27] A. D. Bristow, N. Rotenberg, and H. M. van Driel, Two-photon absorption and Kerr coefficients of silicon for 850–2200 nm, *Appl. Phys. Lett.* **90**, 191104 (2007).

[28] C. J. Chen, J. Zheng, T. Gu, J. F. McMillan, M. Yu, G.-Q. Lo, D.-L. Kwong, and C. W. Wong, Selective tuning of silicon photonic crystal nanocavities via laser-assisted local oxidation, *Optics Express* **19**, 12480 (2011).

[29] P. E. Barclay, K. Srinivasan, and O. Painter, Nonlinear response of silicon photonic crystal micro-resonators excited via an integrated waveguide and fiber taper, *Opt. Express* **13**, 801 (2005).

[30] X. Yang, C. Husko, M. Yu, D.-L. Kwong, and C. W. Wong, Observation of femto-joule optical bistability involving Fano resonances in high-Q/V_m silicon photonic crystal nanocavities, *Appl. Phys. Lett.* **91**, 051113 (2007).

[31] K. Nozaki, T. Tanabe, A. Shinya, S. Matsuo, T. Sato, H. Taniyama and M. Notomi, Sub-femtojoule all-optical switching using a photonic-crystal nanocaviy, *Nature Photonics* **4**, 477 (2010)

[32] V. R. Almeida, C. A. Barrios, R. R. Panepucci and M. Lipson, All-optical control of light on a silicon chip, *Nature* **431**, 1081 (2004).

[33] J. D. Jackson, Classical Electrodynamics, Wiley 1999

[34] A. Armaroli, S. Malaguti, G. Bellanca, S. Trillo, A. de Rossi, and S. Combrié., Oscillatory dynamics in nanocavities with noninstantaneous Kerr response, *Phys. Rev. A* **84**, 053816 (2011).

[35] T. J. Johnson, M. Borselli and O. Painter, Self-induced optical modulation of the transmission through a high-*Q* silicon microdisk resonator, *Opt. Express* **14**, 817-831 (2006).

[36] V. R. Almeida and M. Lipson, Optical bistability on a silicon chip, *Opt. Lett.* **29** 2387 (2004).

[37] Q. Xu and M. Lipson, Carrier-induced optical bistability in silicon ring resonators, *Opt. Lett.* **31**, 341 (2006).

[38] H. A. Haus, *Waves and Fields in Optoelectronics* (Prentice-Hall, Englewood Cliffs, NJ), p. 99 (1984).

[39] X. Yang, C. Husko, M. Yu, D.-L. Kwong, and C. W. Wong, Observation of femto-joule optical bistability involving Fano resonances in high-Q/V_m silicon photonic crystal nanocavities, *Appl. Phys. Lett.* **91**, 051113 (2007).

[40] A. Armaroli, S. Malaguti, G. Bellanca, S. Trillo, A. de Rossi, and S. Combrié, Oscillatory dynamics in nanocavities with noninstantaneous Kerr response, *Phys. Rev. A* **84**, 053816 (2011)

[41] T. J. Johnson, M. Borselli, and O. Painter, Self-induced optical modulation of the transmission through a high-*Q* silicon microdisk resonator, *Opt. Express* **14**, 817 (2006).

[42] J. Yang, T. Gu, J. Zheng, M. Yu, G.-Q. Lo, D.-L. Kwong, C. W. Wong, Radio frequency regenerative oscillations in monolithic high-*Q/V* heterostructured photonic crystal cavities, *Applied Physics Letters* **6**, 104 (2014)

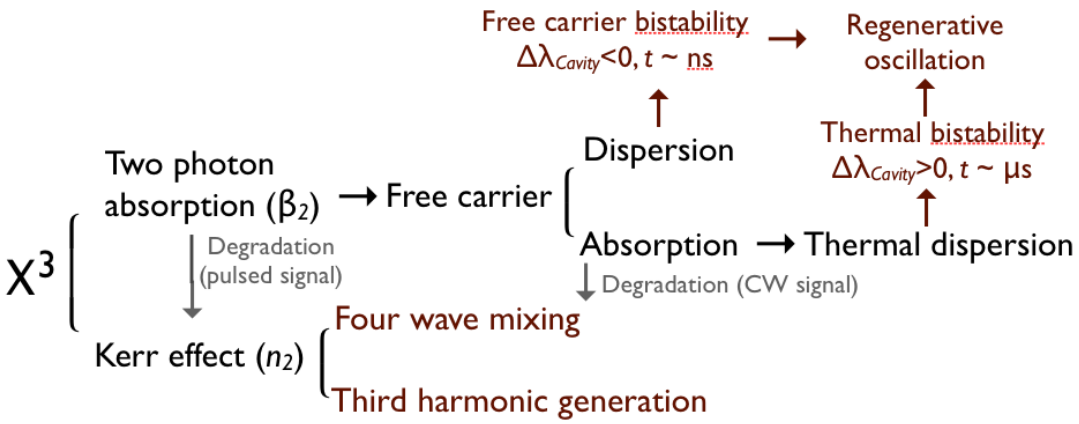

Figure 5-1 | Third order and related high order nonlinear interaction in cavity. The two photon absorption triggers free carriers. Free cavity reduces the refractive index (dispersion) and absorb light. The absorbed light and recombined free carriers leads to thermal dispersion. The dispersion changes the optical power feeding as the cavity resonance shifts. The two photon and free carrier absorption lowers the four wave mixing conversion efficiency.

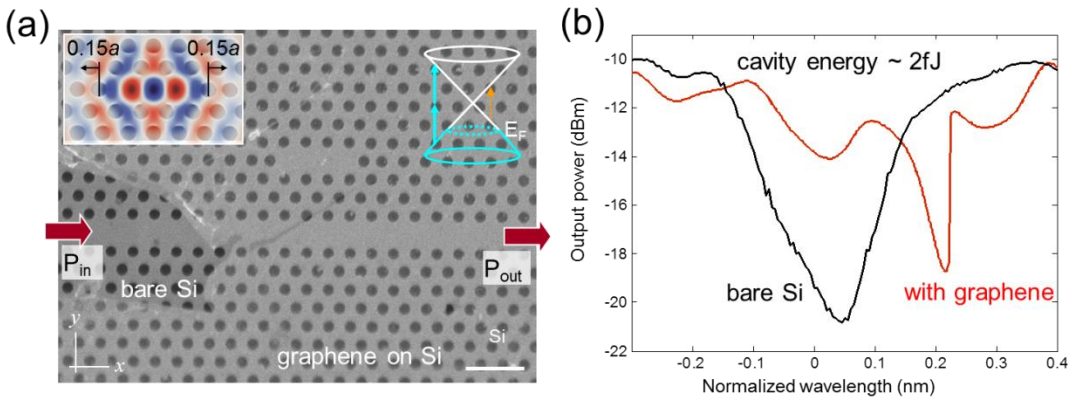

Figure 5-2 | Graphene-cladded silicon photonic crystal nanostructures. (a) Scanning electron micrograph (SEM) of tuned photonic crystal cavity, with lattice constant *a* of 420 nm. Example SEM with separated graphene monolayer on silicon for illustration. Scale bar: 500 nm. Inset: example E_z-field from finite-difference time-domain computations. Right inset: Dirac cone illustrating the highly-doped Fermi level (dashed blue circle) allowing only two-photon transition (blue arrows) while the one-photon transition (orange dashed arrow) is forbidden. (b) Example measured graphene-cladded cavity transmission with asymmetric Fano-like lineshapes (red dotted line) and significantly larger red-shift, compared to a control bare Si cavity sample with symmetric Lorentzian lineshapes (black dashed line). Both spectra are measured at 0.6 mW input power, and are centered to the intrinsic cavity resonances (λ_{cavity_0} = 1562.36 nm for graphene sample, and λ_{cavity_0} = 1557.72 nm for Si sample), measured at low power (less than 100 μW input power). The intrinsic cavity quality factor is similar between the graphene and the control samples.

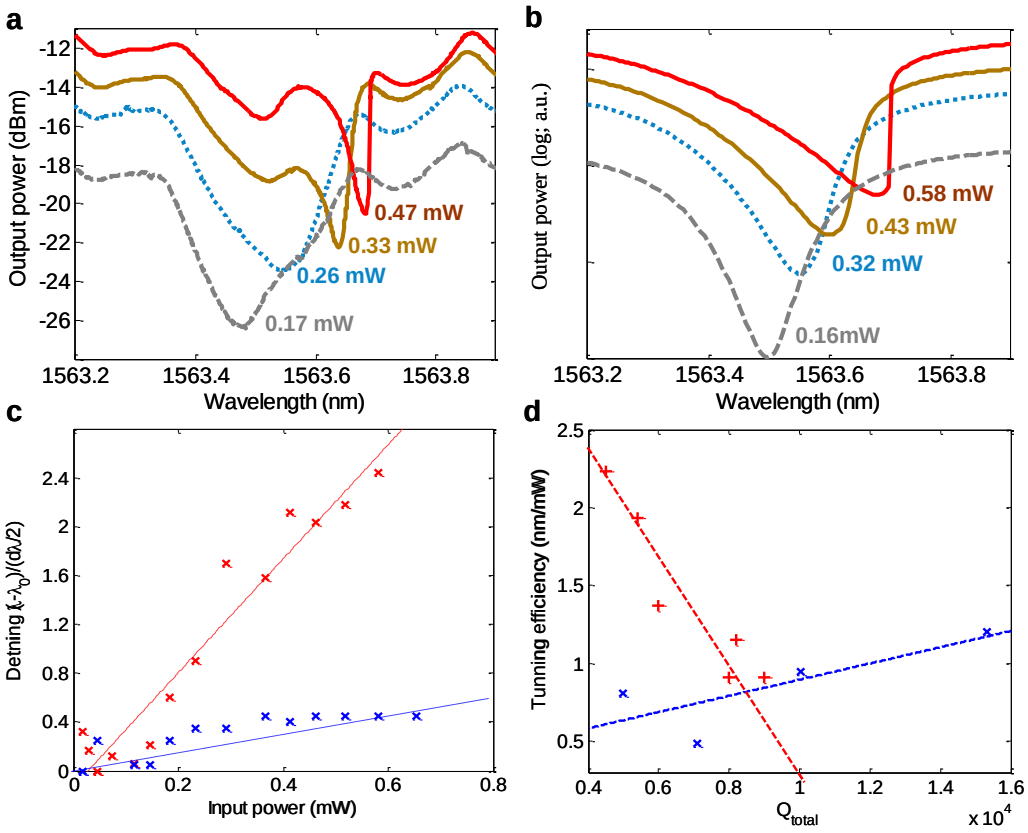

Figure 5-3 | Steady-state two-photon absorption induced thermal nonlinearities in graphene-silicon hybrid cavities. (a) Measured quasi-TE transmission spectra of a graphene-clad *L3* cavity with different input power levels (with extracted insertion loss from the facet of waveguides in order to be comparable to simulation in b). (b) Nonlinear coupled-mode theory simulated transmission spectra. The estimated input powers are marked in the panels. (c) Measured cavity resonance shifts versus input power, with the graphene-clad cavity samples (in red) and the monolithic silicon control cavity sample (in blue). (d) Tuning efficiencies for graphene-clad cavity samples (in red) and control cavity samples (in blue) for a range of cavity loaded *Q*-factors examined.

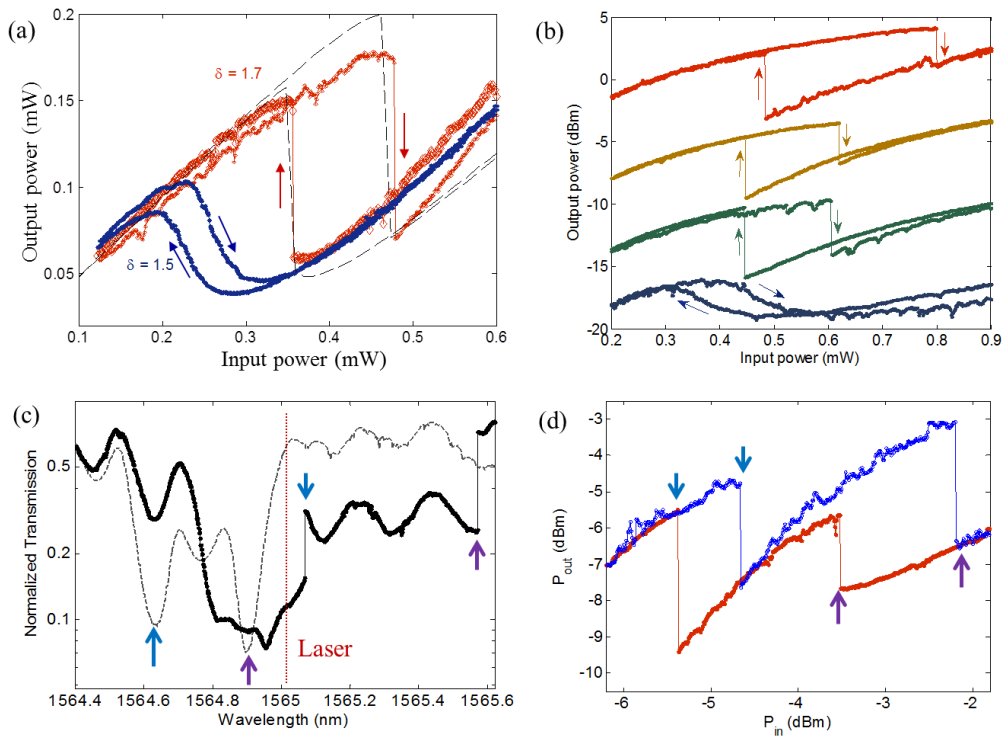

Figure 5-4 | Bistable switching in graphene-clad nanocavities. (a) Steady-state input/output optical bistability for the quasi-TE cavity mode with laser-cavity detuning δ at 1.5 (λ_{laser} = 1562.66 nm) and 1.7 (λ_{laser} = 1562.70 nm). The dashed black line is the coupled-mode theory simulation with effective nonlinear parameters of the graphene-silicon cavity sample.(b) Measured steady-state bistability at different detunings set at 0.18, 0.23, 0.26, 0.29 nm (from bottom to top). The plots are offset for clarity: green (offset 2 dB), brown (offset 8 dB) and red lines (offset 15 dB). (c) Normalized transmission of two cavities with resonance separation of δ =3. The grey dashed line is measured at -16dBm input power, and the solid black line is for 0dBm input. (d) The tranfer function for optical bistability in two cavity system as in (c). The laser detuning is set at δ =3 to the first cavity, and δ =1.5 to the second cavity (marked as dashed line in (c)).

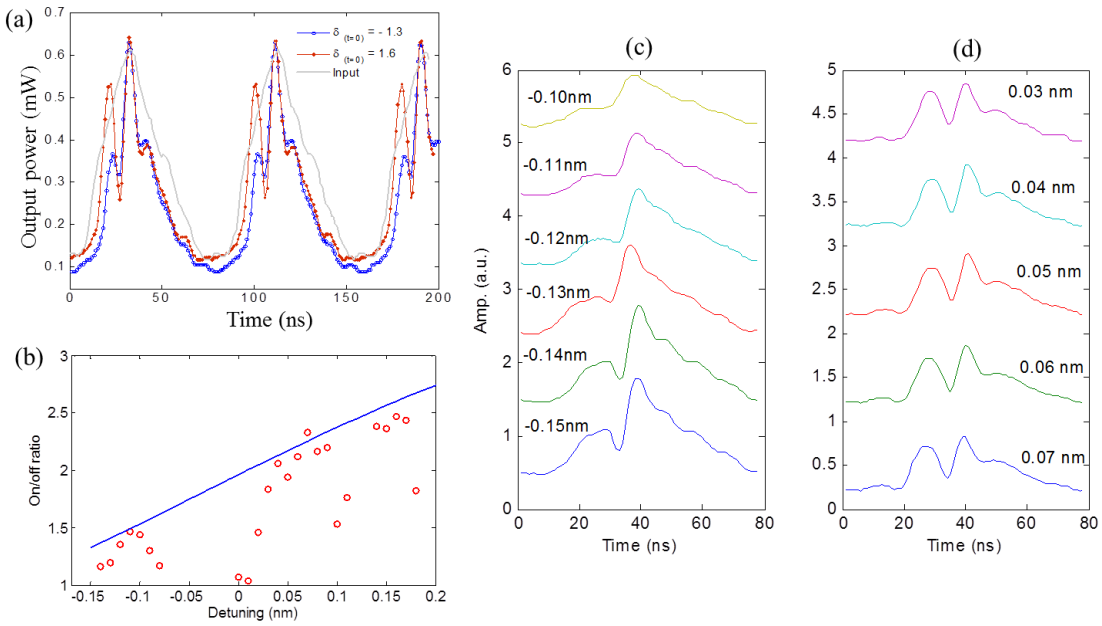

Figure 5-5 | Switching dynamics with triangular waveform drive input (a) The input waveform is dashed grey line. The bistable resonances are observed for both positive and negative detuning. Blue empty circles: δ(t=0) = -1.3(λ_{laser} = 1562.10 nm), red solid circles: δ(t=0) = 1.6 (λ_{laser} = 1562.68 nm). Inset: schematic of high- and low-state transmissions. (b) The ratio between the on off output intensities versus different detunings. (c) The output switching dynamics with the input as in (a), at negative detunings. (d) positive detunings.

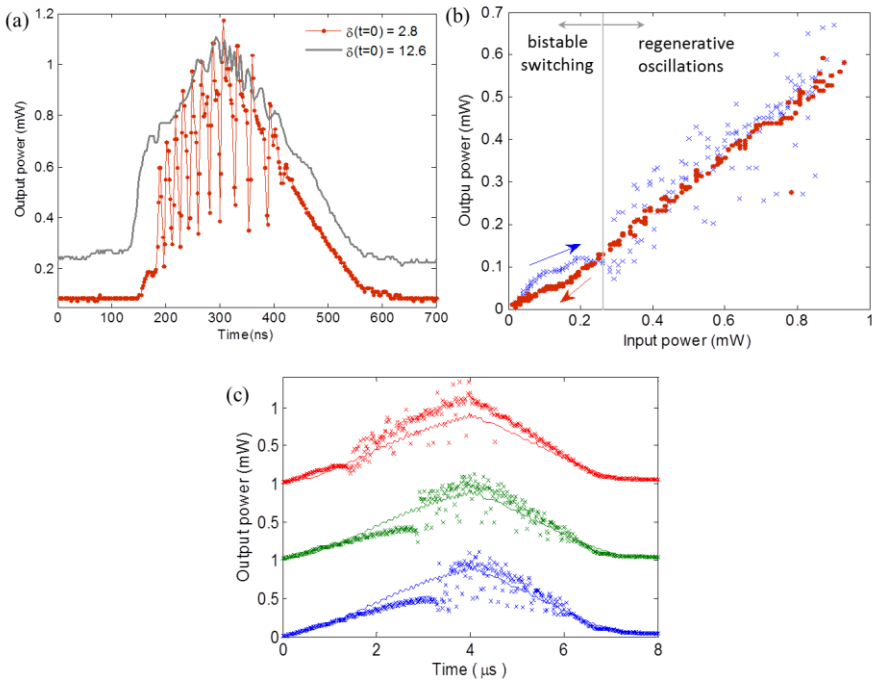

Figure 5-6 | Regenerative oscillations in graphene-cladded nanocavities. (a) Observations of temporal regenerative oscillations in the cavity for optimized detuning (λ_{laser} = 1562.47 nm). The input power is quasi-triangular waveform with peak power 1.2 mW. The grey line is the reference output power, with the laser further detuned at 1.2 nm from cavity resonance (λ_{laser} =1563.56 nm). (b) Mapping the output power versus input power with slow up (blue cross) and down (red) power sweeps. In the up-sweep process, the cavity starts to oscillate when the input power is beyond 0.29 mW.(c) Measured regenerative oscillations at down-sweep, longer temporal basewidths and different detunings in graphene-silicon nanocavities. Output cavity transmission with slowly-varying (7-ms) input laser intensities. The cold cavity resonance is 1562.36 nm, and the laser wavelengths from top to bottom are fixed at 1562.51 nm, 1562.60 nm, and 1562.62 nm. The oscillation starts when the ascending power reaches 0.29, 0.66, and 0.75 mW. Reference outputs plotted as in solid lines.

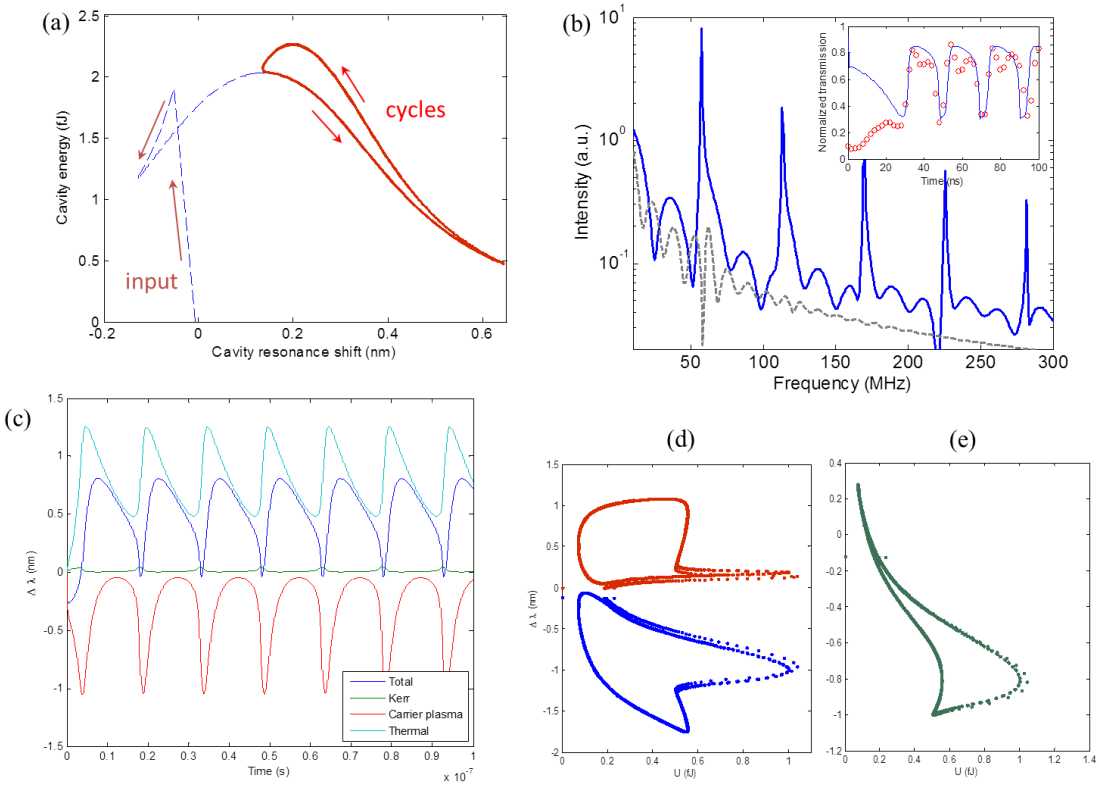

Figure 5-7 | Coupled mode theory calculated cavity resonance oscillation (a) Nonlinear coupled-mode theory model of cavity transmission versus resonance shift, in the regime of regenerative oscillations. With a detuning of 0.15 nm [δ(t=0) = 0.78] the free carrier density swings from 4.4 to 9.1×10^{17} per cm^3 and the increased temperature ΔT circulates between 6.6 and 9.1K. (b) RF spectrum of output power at below (0.4 mW, grey dashed line) and above oscillation threshold (0.6 mW, blue solid line) at the same detuning $\delta_{(t=0)}$ = 0.78 (λ_{laser}-λ_{caviy} = 0.15 nm). Inset: Normalized transmission from model (blue line) and experimental data at the same constant power level (red circles). (c) Cavity resonance shift due to different nonlinear dispersion versus time. (d) Thermal (red) and free carrier (blue) dispersion induced cavity resonance shift versus the energy circulating in cavity.(e) The total carrier resonance dispersion versus cavity.

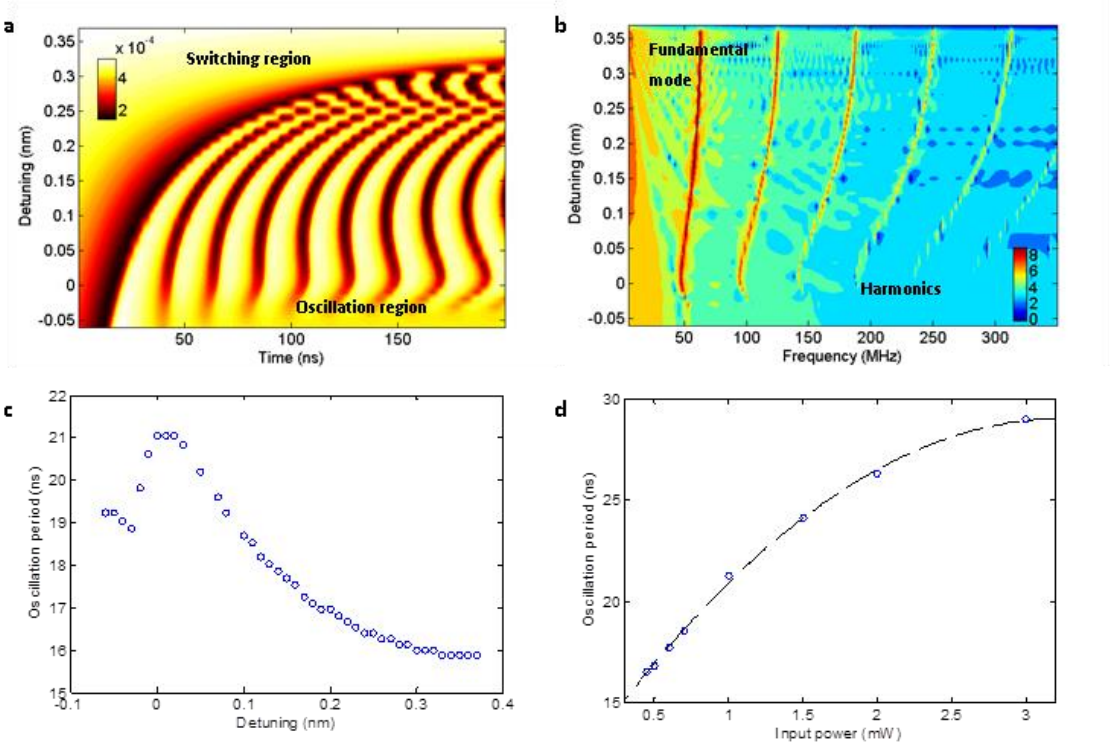

Figure 5-8 | Coupled-mode equations calculated time domain response to a step input with a graphene-clad silicon photonic crystal *L3* nanocavity side-coupled to a photonic crystal waveguide. (a) The output versus input powers for positive and negative detunings (laser-cavity detunings are set from -0.06 to 0.37 nm). Input laser power is set at 0.6 mW. The cavity switching dip is observed for all detunings, and regenerative oscillation exists only predominantly for positive detuning. (b) Frequency response of the cavity switching and oscillation dynamics with conditions as in a (in log scale). The laser detuning is set from -0.06 to 0.37 nm. (c) and (d) Oscillation period versus laser detunings and input powers respectively.

Chapter 6

Optical nonlinearity in PECVD grown silicon nitride ring resonators

6.1. Introduction:

Interplay of free carrier and thermal nonlinearities in high quality factor (*Q*) small mode volume (*V*) optical resonators gives rise to various phenomena including self-pulsation and bistable switching [1-3]. The free carrier generated in the band-to-band transition blue shifts the cavity resonance in different timescales compared to thermal nonlinearity, and can drive the cavities into regenerative oscillations. Plasma-enhanced chemically vapor deposition (PECVD) produced silicon nitride (SiN) is promising for the low loss waveguide and resonators. Second harmonic generation and Kerr nonlinearities are experimentally demonstrated in the PECVD SiN for on-chip nanophotonics [4-5]. In the wide bandgap material, however, midgap/bandtail states induce extra linear loss and thus the thermal nonlinearties. The midgap localized states formed in the PECVD growth enhance the optical nonlinearity of the wide band material to IR light [6]. The hydrogen-bond absorbed the IR light ~0.816eV and turns the optical energy directly to the lattice vibration. Near the absorption peak at 1520nm, the thermal induced nonlinearity effectively shifts the cavity resonance [7] and clear hysteresis loop is shown in the ring with quality factor versus mode volume ratio $(Q/v)=10^{15}$ cm^{-3}. The resonator induced Purcell factor (F) is $\sim 10^{7}$ for light-mater interaction at resonant wavelength [8]. Optical bistability is used to characterize the linear loss in resonators [9]. The ground state energy of the silicon quantum dots is twice as the [N-H] absorption band where laser excites [10]. The close investigation of the passive absorption process in silicon nitride rings is also useful for optimizing their active properties, such as Kerr nonlinearity induced parametric oscillation [11], where minimizing the linear absorption rate is of paramount importance

for low power operation.

6.2. Material analysis of PECVD silicon nitride

6.2.1 Fourier transform Infrared measurement

The optical properties of the waveguide, including refractive index and propagation losses, can be optimized by controlling the plasma frequency, precursor gas ratio and thermal annealing [12]. SiN films are grown by low frequency, low temperature (350^{o}C) PECVD. The 80sccm:4000sccm SiH_4:H_2 ratio and the 400W RF power control the deposition rate of 22.8A/s [13]. PECVD silicon nitride has Si/N ratio from 0.8-1, density of 2.5-2.8g/cm^3, and refractive index of 2.0 at 1550nm wavelength. The optical bandgap is estimated to be 3~4eV [14]. We probe the content of silicon nitride film by the transmission and reflection FTIR methods.

PECVD SiN is grown at low temperature (350^{o}C). Low interlayer stress allows the thickness of SiN layer up to 0.65 μm (Fig. 6-1a). Deep UV lithography defines the width of the waveguide and rings to be 1μm, and gives highly repeatable geometry and the following dry etch gives high aspect ratio. The high aspect ratio leads to distinctive extinction between TE and TM polarization (Fig. 6-1c). The optical properties of the waveguide, including refractive index and propagation losses can be optimized by controlling the plasma frequency, precursor gas ratio and thermal annealing [9]. The characteristic absorption wavelength at 1530nm arises from the superposition of molecular rotations and vibrations (Fig. 6-1c). We verified molecular vibration induced absorption by the FTIR method (Fig. 6-1d). The small band around 485 cm^{-1} is associated with Si

breathing vibrations [15]. The absorption band locates at 863 cm-1 is due to stretching vibration of Si-N bonds [16]. The stretching vibration of Si-N bonds in the alpha-modification of crystalline silicon silicon nitride is at 910 cm^{-1} [17-18]. The bands located around 3356 and 1155 cm^{-1} correspond to stretching and bending vibrations of N-H bonds. Si-H bonds' stretching mode is at 2205 cm^{-1}.

6.2.2 Transmission measurement in waveguide

CW light generated from tunable laser (AQ4321) is sent onto chip through polarization controller and lensed fiber. An automatic power control circuit built in Ando laser AQ4321 maintains the optical output stability within +/- 0.01 (0.05) dB or less in 5 min (1h). With integrated spot size converter, the total fiber-chip-fiber loss is reduced to 14dB. The output light is collected by both power meter and high speed IR photo-receiver photo detector (New Focus Model 1554B, DC-12GHz bandwidth). The fast photo-detector is connected to the digital phosphor oscilloscope (Tektronix TDS 7404, DC-4GHz bandwidth).

By scanning the tunable laser through the wavelength range from 1480nm to 1560nm, we measured the transmitted power of waveguides made of length ranging from 25mm to 44mm with 5mm step. The fitting the transmitted power versus waveguide length with linear model gives propagation loss of 4.3 dB/cm at 1550nm, and -13.5 dB insertion loss from the two facets of waveguides. However, the total loss is observed to be strongly wavelength dependent. The total optical loss includes the wavelength independent part (insertion loss, propagation scattering loss), and the wavelength sensitive part (molecular bond absorption). The propagation loss has an absorption peak at 1520 nm with 37.2 nm

(20meV) full width half maximum. The maximum loss is 6.8dB/cm at 1520nm and reduces to 2.3dB/cm when the wavelength detuned 25nm away from the absorption peak. The propagation scattering loss (wavelength independent) due to scattering is about 2dB/cm.

6.3 Linear absorption dependent quality factors

The wavelength dependent linear absorption is plotted in Fig. 6-1c, obtained by subtracting the transmission of the 25mm waveguide from the 40mm long waveguide, and then divided by the differential length between the two waveguides. The propagation loss composes of the scattering from the sidewall of the waveguide and the material absorption in near IR range. The scattering loss keeps constant over wide band. The material absorption near 1520nm is mostly induced by the absorption in [N-H] bond.

Fig. 6-2a plots the transmission of waveguide with side coupled ring and 25mm long waveguide at low power input. The distance between the ring and waveguide is 0.4μm. The relation between the ring quality factor (derived from the rings) and the linear propagation loss (derived from the transmission of waveguide) is plotted in Fig. 6-2b. The increasing quality factor with the linear propagation loss is due to the non-ideal coupling between the ring and the waveguide. The total *Q* factor of a microring resonator coupled to a single waveguide can be expressed as [20-21]:

$$Q_{total}(\alpha) = \frac{2\pi n_{eff}}{\lambda_0} \frac{L}{2\arccos[2-(0.5/t)\exp(-\alpha L/2)-0.5t\exp(\alpha L/2)]} = \frac{\lambda_0}{\Delta\lambda_{3dB}} \qquad (1)$$

Where n_{eff}=1.6 is the effective refractive index of silicon nitride waveguide. λ_0 is the

resonance wavelength of the ring, L is the circumference of the ring, t is the field transmission coefficient between the ring and waveguide. α is the wavelength dependent propagation loss of the waveguide. By fitting the model to the measured data, we obtained the field transmission coefficient t = 0.8 (Fig. 6-2b) for the gap of 0.5 μm between the waveguide and the ring. It is noted that the trend is inverse with t=1. The maximized linear absorption and ring quality factor near 1520nm form an ideal condition for investigating the optical nonlinearity from the light matter interaction. By comparing the ring resonance shift at 0.3 mW input power to cold ring resonance, the proportional relation between thermal optic shifts versus the quality factor in the inset of Fig. 6-2b.

The optical transmission of the ring at different input power is plotted in Fig. 6-2c. The experimental data are fitted by the nonlinear coupled mode theory (CMT). Nonlinear CMT incorporates the linear absorption and nonlinear absorption from the silicon quantum dots. The later one only contributes about 5% of the total thermal dispersion at 0.25mW input. The coupling and intrinsic quality factors are 85,000 and 1,500,000 respectively. The linear absorption from the [H-N] is maximized near the cold cavity resonance at 1532.212nm. From the CMT curve fitting at low power level, different loss rate in the ring from the lateral coupling to waveguide. The lateral coupling loss rate of the ring ($\omega_0/Q_{in}/2$) is 12.4 GHz, and the linear absorption rate is 2 GHz (Fig. 6-2c).

To verify the linear relation between the cavity resonance shift versus the input optical power. The steady state cavity tuning process by the optical absorption is tested by the cw pump-probe method (Fig. 6-2d). By setting the pump laser near the mode at 1540nm, and varying the probe detuning for its neighboring mode, we clearly observe the nonlinearity

shifts the cavity resonance approaches and deviates from probe wavelength as the pump power increases up to 140μW. The probed power is fixed at 22 μW. The output of the pump power is blocked by a 30dB notch filter, and only the probe power is collected as the pump laser increases its power. The tuning efficiency is 38pm/mW, similar to the method directly tracking the cavity resonance shift with pump mentioned in Fig. 6-3.

6.4. Steady state measurement of silicon nitride rings

The transmission lineshape evolves from symmetric Lorenzian to unsymmetrical bistable one as the input power increases from 10 μW to 200μW (Fig. 6-3 a-b). We measured three rings with radii of ~20, 40 and 70 μm, with loaded, intrinsic quality factor and FSR respectively of 24,500, 49,000, 69,600, 175,000,4.4nm and 77,300, 244,000, 2.9nm at 1550nm. The 40μm radius ring is presented here for nonlinearity investigation due to its highest *Q/V* ratio. The loaded and intrinsic factors are obtained by CMT curve fitting.

The plot of the probe detuning versus the pump power driving cavity onto resonance gives a linear cavity resonance shift of 35pm/mW at 1540nm (Fig. 6-3c). The tuning efficiency increases to peak value at 80pm/mW for the resonance at 1520nm wavelength, and drops to 10pm/mW near 1610nm resonance under optimized polarization and coupling control. Fig. 6-3d plots cavity resonance shift versus the input power. The straight linear relation implies negligible contribution from high order nonlinear absorption (Two Photon Absorption and Free Carrier Absorption related thermal nonlinearities).

6.5. Model calibration for the bi-stable switch

We model the nonlinear cavity transmissions with time domain nonlinear coupled mode

theory for the photon and temperature dynamics:

$$\frac{da}{dt} = (i(\omega_L - \omega_0 - \Delta\omega_T) - \frac{1}{2\tau_t})a + \kappa\sqrt{P_{in}}\,, \tag{2}$$

$$\frac{d\Delta T}{dt} = \frac{R_{th}}{\tau_{th}\tau_{lin}} |\, a\,|^2 + \frac{\Delta T}{\tau_{th}} \quad , \tag{3}$$

Where a is the amplitude of resonance mode; ΔT is the cavity temperature shift. P_{in} is the power carried by incident CW laser wave. κ is the coupling coefficient between waveguide and cavity, adjusted by the linear absorption in waveguide. ω_L-ω_0 the is detuning between the laser frequency (ω_L) and cold cavity resonance (ω_0). The thermal induced dispersion is $\Delta\omega T=\omega_0\Delta T(dn/dT)/n$. The total loss rate is $1/\tau_t = 1/\tau_{in}+1/\tau_v+1/\tau_{lin}$. $1/\tau_{in}$ and $1/\tau_v$ are the loss rates into waveguide (coupling loss) and into free space (scattering loss), ($1/\tau_{in/v} = \omega/Q_{in/v}$). The hydrogen bond absorption leads to the linear rate independent of time: $1/\tau_{lin}=c\alpha$. The linear absorption is expressed as: $\alpha=(\sigma_{Si\text{-}H}N_{Si\text{-}H}+\sigma_{N\text{-}H}N_{N\text{-}H})/n$. The Si-H bond and N-H bond density are derived from the Fourier transform infrared spectroscopy. By using SiH_4 to N_2 gas flow ratio of 80:4000 in the PECVD growth, the density of silicon-hydrogen and nitrogen-hydrogen bond are $\rho_{Si\text{-}H}=3.94\times10^{21}$ cm^{-3} and $\rho_{N\text{-}H}=5.11\times10^{21}$ cm^{-3} respectively; The absorption cross sections are $\sigma_{Si\text{-}H}=5.3\times10^{-18}$ cm^2 and $\sigma_{N\text{-}H}=7.4\times10^{-18}$ cm^2 for them respectively. Kerr dispersion is negligibly small compared to the thermal effect and thus not included here. The rest of linear and nonlinear parameters in silicon nitride ring are listed in the table 6-I.

To show the linear and nonlinear effect of absorption rate to resonator lineshape, we compared the linear and nonlinear response of the ring with different material absorption lifetime. We show the aligned model with the experimental data and simulated the other two conditions with too low and high absorption rate.

The optical absorption in near IR range composes of both linear absorption comes from the N-H bonds. Through the model-measurement alignment at different power levels, the

linear absorption lifetime is 0.4ns. In linear region, high linear absorption lowers the on-resonance transmission (Fig. 6-3a). In nonlinear region, the high linear absorption increases cavity resonance shift (Fig. 6-3b). The transmission spectrum of ring resonance at different power levels are shown in Fig. 6-3c-d. The transfer function of input and output power shows clear bistability when the laser detuning ($\delta=(\lambda_L-\lambda_0)/(\Delta\lambda/2)$) is set at δ=3.42 and 3.72 (Inset of Fig. 6-3d), where λ_L, λ_0, and $\Delta\lambda$ are laser wavelength, cold cavity resonance and cavity bandwidth respectively.

Table 6-I. Physical parameters used in the CMT model matching experiment

Parameter	Symbol (unit)	SiN
SiN refractive index	n	2.03
Radius of the ring	r (μm)	40
Mode volume	V(μm^3)	25.1 [FDTD]
Loaded Q	Q	85,000 [CMT]
Intrinsic Q	Q_0	1,500,000 [CMT]
Thermo-optic coeff.	dn/dT (K^{-1})	2.6×10^{-5} [23]
Scattering rate	$1/\tau_v$ (GHz)	0.42 [Cal]
Linear absorption rate	$1/\tau_{lin}$ (GHz)	2.5 [CMT]
Coupling rate	$1/\tau_{in}$ (GHz)	72.5 [Cal]
Heat capacity	C (J/K/kg)	700 [25]
Specific heat	$c_v\rho$ (W/Km^{-3})	1.84×10^6
Thermal resistance	R_{th} (K/mW)	17.5 [Cal]
Thermal relaxation time	$\tau_{th,c}$ (ns)	950 [24]

[CMT]: couple mode theory curve fitting; [Cal]: Derived value from other parameters [FDTD]: Finite difference time domain method calculation

To further interpret the thermal dispersive behavior and study the cavity tuning process, we applied steady state pump-probe method. By setting the pump laser near the mode at

1540nm, and varying the probe detuning for its neighboring mode, we clearly observe the nonlinear resonant shifts approaches and deviates from probe as the pump power increases up to 140μW. The probed power is fixed at 22 μW. The plot of the probe detuning versus the pump power driving cavity onto resonance gives the linear relation between cavity resonance shift efficiency 35pm/mW at 1540nm (Fig. 6-4a). The dynamic thermal lifetime is measured to be ~150μs as the laser wavelength set near the cavity resonance suddenly turned on, the transmission stabilized with the exponential decay within the thermal lifetime (Fig. 6-4b).

6.6. Conclusion:

The wavelength selective absorption in communication C band is investigated in CMOS-processed PECVD silicon nitride rings with 1.5 million intrinsic quality factor. The non-ideal coupling between the ring and waveguide makes the ring quality factor increase with propagation loss. Both the material absorption and the ring quality factor are maximized near 1520nm, inducing strong light-matter interaction for optical bistability. We calibrated the nonlinear parameters by the transmission lineshape of the ring and the waveguides, and show negligible modification from the silicon quantum dots to thermal nonlinearities despite of its long free carrier lifetime.

Bibliography

[1] X. Yang, C. Husko, C. W. Wong, M. Yu, and D. L. Kwong, "Observation of femtojoule optical bistability involving Fano resonances in high-Q/V_m silicon photonic crystal nanocavities," *Applied Physics Letters* **91**, 051113-051113 (2007)

[2] C. Husko, A. De Rossi, S. Combrié, Q. V. Tran, F. Raineri, and C. W Wong,. "Ultrafast all-optical modulation in GaAs photonic crystal cavities," *Applied Physics Letters* **94**, 021111 (2009).

[3] T. Gu, N. Petrone, J. F. McMillan, A. van der Zande, M. Yu, G. Q. Lo, and Wong, C. W. "Regenerative oscillation and four-wave mixing in graphene optoelectronics," *Nature Photonics* **6**, 554-559 (2012).

[4] T. Ning, H. Pietarinen, O. Hyvärinen, J. Simonen, G. Genty, and M. Kauranen, "Strong second-harmonic generation in silicon nitride films," *Applied Physics Letters* **100**, 161902 (2012).

[5] K. Ikeda, R. E. Saperstein, N. Alic and Y. Fainman, "Thermal and Kerr nonlinear properties of plasma-deposited silicon nitride/silicon dioxide waveguides," *Optics Express* **16**, 12987-12994 (2008)

[6] S. C. Mao, S. H. Tao, Y. L. Xu, X. W. Sun, M. B. Yu, G. Q. Lo, and D. L. Kwong, "Low propagation loss SiN optical waveguide prepared by optimal low-hydrogen module," *Optics Express* **16**, 20809-20816 (2008).

[7] A. Gondarenko, J. S. Levy, and M.. Lipson, "High confinement micron-scale silicon nitride high Q ring resonator," *Optics Express* **17**, 11366-11370 (2009).

[8] J. Vučković, M. Lončar, H. Mabuchi, and A. Scherer, "Design of photonic crystal microcavities for cavity QED," *Physical Review E* **65**, 016608 (2001).

[9] H. Rokhsari, S. M. Spillane, and K. J. Vahala,. ”Loss characterization in microcavities using the thermal bistability effect,” *Applied physics letters* **85**, 3029-3031 (2004).

[10] T. Carmon, L. Yang, and K. Vahala. "Dynamical thermal behavior and thermal self-stability of microcavities," *Optics Express* **12**, 4742-4750 (2004).

[11] J. S. Levy, A. Gondarenko, M. A. Foster, A. C. Turner-Foster, A. L. Gaeta, and M. Lipson, “CMOS-compatible multiple-wavelength oscillator for on-chip optical interconnects,” *Nature photonics* **4**, 37-40 (2009).

[12] A. Gorin, A. Jaouad, E. Grondin, V. Aimez, and P. Charette, “Fabrication of silicon nitride waveguides for visible-light using PECVD: a study of the effect of plasma frequency on optical properties,” *Optics express* **16**, 13509-13516 (2008).

[13] S. C. Mao, S. H. Tao, Y. L. Xu, X. W. Sun, M. B. Yu, G. Q. Lo, and D. L. Kwong, “Low propagation loss SiN optical waveguide prepared by optimal low-hydrogen module,” *Optics Express* **16**, 20809-20816 (2008).

[14] S. V. Deshpande, E. Gulari, S. W. Brown, and S. C. Rand, “Optical properties of silicon nitride films deposited by hot filament chemical vapor deposition,” *Journal of Applied Physics* **77**, 6534 (1995).

[15] D. V. Tsu, G. Lucovsky, and B. N. Davidson, “Effects of the nearest neighbors and the alloy matrix on SiH stretching vibrations in the amorphous SiO_r: H (0< r< 2) alloy system,” *Physical Review B* **40**, 1795 (1989).

[16] A. Ortiz, L. RodríGuez-Fernandez, and J. C. Alonso, “Composition, structural, and electrical properties of fluorinated silicon-nitride thin films grown by remote plasma-enhanced chemical-vapor deposition from SiF_4/NH_3 mixtures,” *Journal of Vacuum Science Technology* **22**, 570-577 (2004).

[17] D. V. Tsu, and G. Lucovsky, “Silicon nitride and silicon diimide grown by remote plasma enhanced chemical vapor deposition,” *Journal of Vacuum Science & Technology A: Vacuum, Surfaces, and Films* **4**, 480-485 (1986).

[18] N. Wada, S. A. Solin, J. Wong, and S. Prochazka, “Raman and IR absorption spectroscopic studies on α, β, and amorphous Si_3N_4,” *Journal of Non-Crystalline Solids* **43**, 7-15 (1981).

[19] A. Yariv. "Critical coupling and its control in optical waveguide-ring resonator systems." *Photonics Technology Letters, IEEE* **14**(4), 483-485(2002).

[20] H. Y. Wen, O. Kuzucu, M. Fridman, A. L. Gaeta, L.-W. Luo, and M. Lipson. "All-optical control of an individual resonance in a silicon microresonator." *Physical Review Letters* **108**, 223907 (2012).

[21] J. Niehusmann, A. Vörckel, P. H. Bolivar, T. Wahlbrink, W. Henschel, and H. Kurz, “Ultrahigh-quality-factor silicon-on-insulator microring resonator,” *Optics Letters* **29**, 2861-2863 (2004).

[22] A. Vorckel, M. Monster, W. Henschel, P. H. Bolivar, and H. Kurz, “Asymmetrically coupled silicon-on-insulator microring resonators for compact add-drop multiplexers,” *Photonics Technology Letters, IEEE,* **15**, 921-923 (2003).

[23] G. S. Wiederhecker, L. Chen, A. Gondarenko, and M. Lipson, “Controlling photonic structures using optical forces,” *Nature* **462**, 633-636 (2009).

[24] C. Baker, S. Sebastian, D. Parrain, S. Ducci, G. Leo, E. M. Weig, and I. Favero, "Optical instability and self-pulsing in silicon nitride whispering gallery resonators." *Optics Express* **20** 29076-29089 (2012).

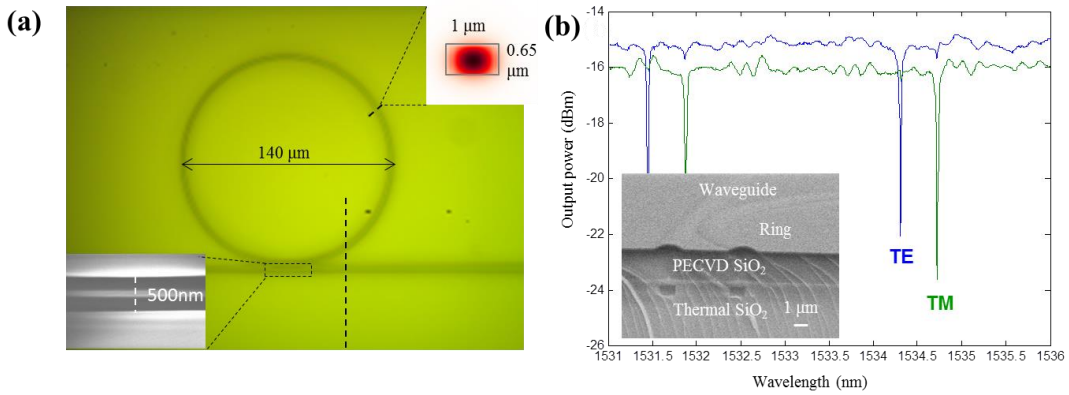

Figure 6-1 | Structure and linear optical properties of the device (a) Silicon nitride device layout. Optical image of top view of the ring, where the dashed line shows the cleaved position for the SEM image. (b) Output spectrum of TE and TM polarized input with 0dBm input power. Inset: 650nm PECVD silicon nitride is sandwiched between the PECVD silicon oxide up cladding layer and the thermal oxide lower cladding layer. Scale bar: 1um. Inset (up right): Cross section and the optical profile of the TE mode. Inset (bottom left): SEM image of the ring-waveguide coupling part.

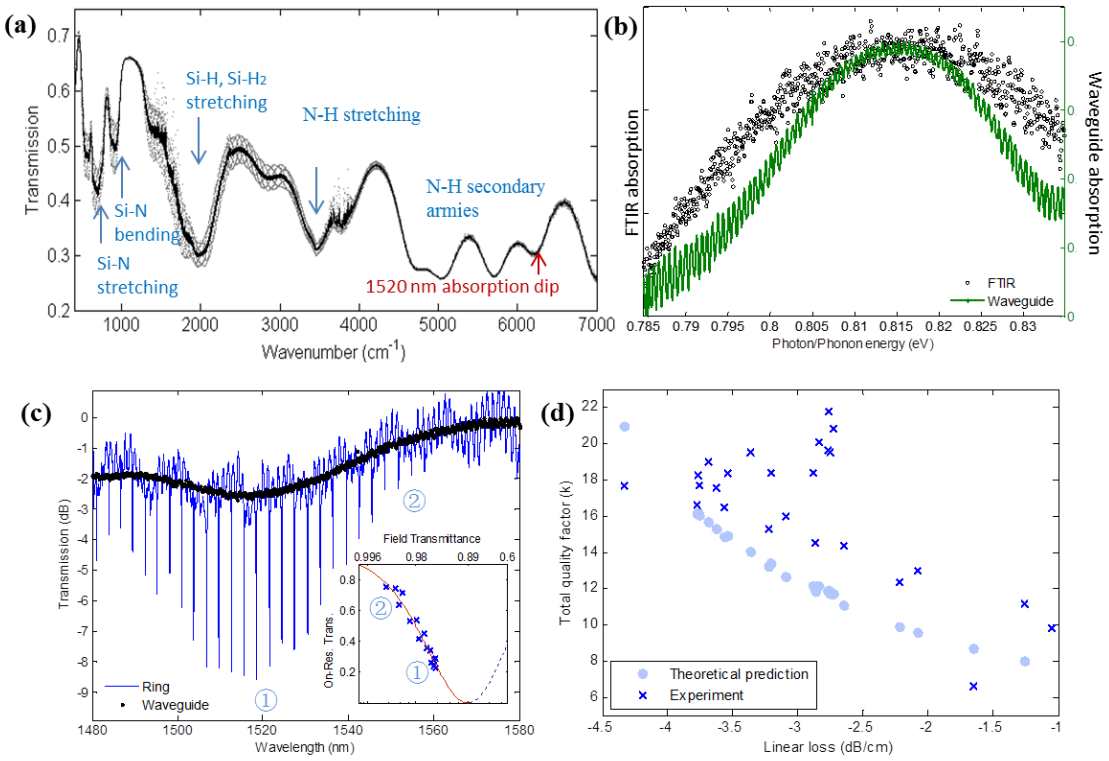

Figure 6-2 | Wavelength dependent absorption and ring quality factor (a) Linear absorption of the PECVD grown silicon nitride thin film, in the range of mid infrared and near infrared. (b) FTIR measured absorption versus phonon energy of PECVD silicon nitride thin film (black circles) and the absorption of a 25mm long SiN waveguide versus photon energy from tunable laser (green line). Wavelength dependent linear propagation loss near 1520nm. The absorption peak is at 0.815eV with FWHM of 0.03eV. (c) Normalized transmission of ring resonator of 70um radius (blue) and 6.7 mm long waveguide (black). Inset: transmission on resonance versus intracavity field transmission. The blue crosses are experimental data. Red solid line and blue dashed line are theoretical predictions for over-coupled and under-coupled region respectively. (d) Linear loss depdent total quality factors. Experimental results are directly derived from fitting the ring resonances in c, and theoretical predicts are given by Eq. 6-2.

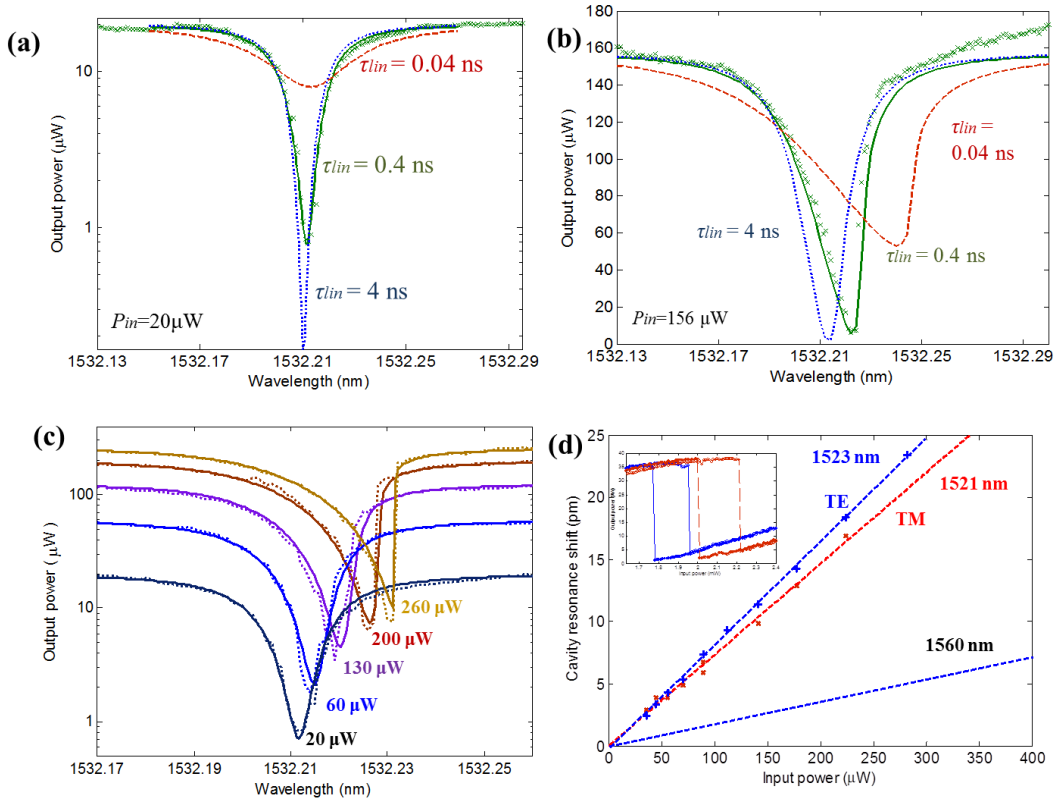

Figure 6-3. | Photon loss and thermal dispersion (a) The transmission spectrum with input power at 20uW for linear characterization. The red dash curve, green solid curve, and the blue dotted curve are CMT simulation results with linear absorption rate of 1/0.04ns, 1/0.4ns and 1/4ns. The cross is experimental data. (a) The transmission spectrum with input power at 156μW for linear characterization. The red dash curve, green solid curve, and the blue dotted curve are CMT simulation results with linear absorption rate of 1/0.04ns, 1/0.4ns and 1/4ns. The cross is experimental data (b) Optical transmission lineshape at different optical input power (0.02, 0.06, 0.13,0.20 and 0.26mW). The dashed curves are experimental data and the solid curves are coupled mode theory simulation. (c) Cavity resonance shift versus the input power at absorption peak (80pm/mW near 1520nm) and away of the absorption peak (20pm/mW near 1560nm) Inset: The Hysteresis loop of the output versus input power is measured for the resonance near 1523nm with TE polarization. The laser-resonance detuning are set at 33 and 34pm for the blue and red lines respectively.

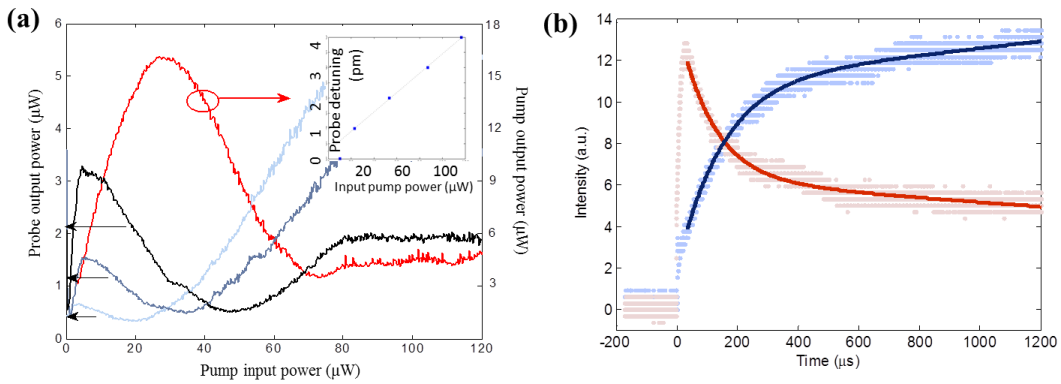

Figure 6-4 | Thermal optical bistability near the molecular vibration peak (a) Output power of pump and probe versus input pump power. The pump detuning is 3.06 (red) to mode resonant at 1540.065nm and the probes are set at 2.81 (light blue), 2.87 (navy), and 2.93 (black) to the mode resonant at 1542.962nm (b) Time domain cavity response to the step function input. The laser intensity turns on at 0μs to 1mW. The laser-cavity detunings are -2pm (red) and 2pm (blue) respectively. The dots are experimental data and the lines are the exponential curve fitting. The lifetime is about 150 μs for both cases.

Chapter 7

Carrier recombination and transport in GaAs based InAs/InGaAs DWELL solar cells

7.1 Introduction

Photon absorption, carrier generation, transport and collection are firmly related processes in solar cells, determined by the three dimensional band structure of the material. In some cases, not all photogenerated carriers are collected by electrodes, shown by degraded open circuit voltage in heterojunction solar cells, including semiconductor quantum dots solar cells and almost of the low-coast solar cells [1-3]. The carrier transport efficiency is related to electron/hole mobility as they travel through the *pn* junction. Involving materials with low bandgap would enhance light absorption, but both photocurrent and dark current are disturbed by the interface states in the heterostructure. In most organic solar cells, *p* region and *n* region are diffused into reach other, and thus the dark current is enhanced through decreased shunt resistance/random oriented current channels. Semiconductor *epi* wafers have sharp junction by well controlled Molecular Beam Epitaxy (MBE) / metalorganic vapor phase epitax (MOCVD) growth, and the built-in field is parallel to carrier transport direction [2-6]. The quantum dots in different layers are self-aligned, and thus form vertical channels to guide photo-generate carriers [4]. It is reported that InAs/InGaAs dots-in-a-well (DWELL) in intrinsic layer are firmly related to photocurrent generation and transport process in *pin* junction [5-7]. The strong confinement provided by the uniform dots randomly embedded in quantum well plane efficiently suppresses lateral carrier diffusion to other randomly oriented current channels (e. g. cell edge states) [8-9]. The diffusion blocking effect could be explained by Anderson localization in 2D system, which is demonstrated to decrease the conductivity (carrier diffusion and conduction are proportionally related by Einstein relation). The strong carrier confinement effect is

indirectly observed here in MBE growth samples with high uniformity [11], but not in MOCVD grown samples [12]. Also it is interesting to observe that solar cell with collapsed DWELL layers (voids in DWELL layers) exhibit similar IV behavior as organic solar cells, with low shunt resistance and filling factor, even the photocurrent remains high.

Recent interest in using InAs quantum dots (QDs) in the absorbing region of solar cells has focused primarily on the predicted increase in quantum efficiency due to the intermediate band effect or simply larger short circuit current density. However, the three-dimensional carrier confinement inherent to QDs endows them with carrier transport capabilities that have not been previously explored in the context of solar cells. In this chapter, it is observed that InAs/InGaAs "dots-in-a-well" (DWELL) structures efficiently suppress lateral carrier diffusion. Therefore, not only do the DWELL structures enhance photocurrent by extending the absorption edge, but they should also inhibit the spreading of current to the perimeter of a device where edge recombination can dominate [13-14]. I examine this premise by comparing the dark current behavior of DWELL cells and GaAs control cells of varying area. The results are promising for applications such as concentration and flexible surfaces where shrinking the size of the device while maintaining high charge collection efficiency are of paramount importance.

7.2 Fabrication and measurement

The control and DWELL samples were fabricated simultaneously to minimize process variation. The Ge/Au/Ni/Au emitter metallization creates the solar cell finger grid and is laid out in three different areal dimensions ($5\times5mm^2$, $3\times3mm^2$, and $2\times2mm^2$). The bottom

Ti/Pt/Au p-type contact is common for the solar cells on the sample. A 270-nm deep mesa, which reaches the intrinsic region, is dry-etched to separate neighboring solar cells with an isolation resistance of ~10^5 Ohm. Finally, an anti-reflective coating (ARC) layer is deposited on the front surface for reducing the reflection loss and improving the surface passivation. The ARC layer is 80-nm thick Si_xN_y with a refractive index around the geometric mean of air and GaAs.

Table 7-1: Measured short circuit current densities (J_{sc}), open circuit voltages (V_{oc}), and efficiencies of the GaAs control cells and InAs DWELL solar cells under AM1.5G illumination.

Size	***J_{sc} (mA/cm^2)***		***V_{oc} (V)***		***Efficiency (%)***	
	Control	*DWELL*	*Control*	*DWELL*	*Control*	*DWELL*
5×5 mm^2	9.46	11.23	0.914	0.665	8.85	7.04
3×3 mm^2	9.08	12.23	0.890	0.670	7.61	7.79
2×2 mm^2	9.17	12.93	0.834	0.675	7.41	8.17

For IV characterization, the cell is illuminated using an ABET Technologies 150-Watt Xe lamp. A filter is inserted between source and cell to simulate the AM1.5G spectrum. The solar cell is connected to an HP parameter analyzer by a four-point probe approach to eliminate the series resistance introduced by the probes and the parameter analyzer. A TE cooler is used to fix the cell temperature at 25.0±0.1^{o}C throughout the test. As shown in Figure 7-1, the typical DWELL device exhibits higher short circuit current density (J_{SC}) while maintaining the same open circuit voltage (V_{OC}) for smaller areas. For the GaAs control cells, however, smaller size, which has a higher perimeter-to-area ratio, makes edge recombination current dominant in these devices, and, thus, severely impacts their

V_{OC} and efficiency. Here V_{OC} of the 2×2 mm^2 GaAs cell is 10% lower than the 5×5 mm^2 one as shown in Figure 7-1 & table 7-1.

7.3 Modeling

To investigate the underlying physics of the V_{OC} degradation in the control samples, the dark IV is measured and the carrier recombination mechanism is analyzed. Here, the conventional single-diode model described in [15] with constant reverse saturation current and ideality factor fails to describe the dark behavior of either the control or DWELL cells, so different models involving non-radiative recombination on the edge or in the quantum dot layers are constructed for the control and DWELL cells, respectively.

The ideality factors for both the control and DWELL cells are measured as shown in Figure 7-2(a) and (c). Substantial differences between the GaAs and DWELL cells include the shoulder in the GaAs cells' IV curves and the resulting hump in the local ideality factor. Neither of these effects is observed for any area size in the DWELL cells. The peak in the ideality factor is more significant as the area of the GaAs cell decreases, which suggests that edge recombination is important. Another series of wafer growths and processing produced the same results. This strongly voltage-dependent ideality factor can be modeled by the pinning of the Fermi-level to surface states at the device perimeter [17-19].

7.3.1 GaAs control cell

The relevant equations for modeling the GaAs controls cells are:

$$J_d = J_b + J_p \tag{1-a}$$

$$J_b = J_{b0} \exp\left(\frac{V - J_d \times A \times R_s}{n_b V_t}\right) \tag{1-b}$$

$$J_p = q \frac{n_s p_s - n_i^2}{(n_s + n_l)/S_{p0} + (p_s + p_l)/S_{n0}} \times d \times \frac{P}{A} \tag{1-c}$$

where J_b is the bulk contribution and J_p is from the perimeter of the cell. The parameters are well adjusted for this model to fit the experimental data as shown Fig7-2(a) and (b). J_b follows the conventional diode equation, and J_p is modeled using Shockley-Read-Hall (SRH) statistics as expressed in equation (1-c) [20]. It is assumed that the ideality factor (n_b) and reverse saturation current density (J_{b0}) of the bulk diode are constants over the bias range where SRH recombination dominates. The surface carrier density (p_{s0}, n_{s0}) influences the peak location of the hump in the ideality factor in Fig. 7-2(a), and the surface recombination rate (S_{p0}, S_{n0}) determines the shape of the hump. At high bias (>0.8V), the series resistance (R_s) dominates the trend. Based on these features, the model is adjusted to fit the tested ideality factor and dark current density (Fig. 7-2 (a-b)). The parameters used in equation (1-b) for describing the bulk component, are the same for three different scales, while the exposed edge surface to area ratio is rising with the shrinking size. The misfit between the model (dash line) and the experiment (solid line) in Fig. 7-2 (a) and (b) might be due to the non-uniform current distribution as shown in the Silvaco simulation picture inserted in Fig. 7-2(c).

In equation (1), n_i is the intrinsic carrier density for GaAs, and V_t is the thermal voltage at room temperature. p_s,n_s = p_{s0},n_{s0} + dn where dn is the injected carrier density ($n_i exp(V/2/V_t)$). n_b is 1.31, J_{b0} is $1.2*10^{-10}$ mA/cm^2. S_{p0} is 0.8, 1.0, 1.0x10^{7}cm/s, S_{n0}=7, 3, 2x10^{7}cm/s, p_{s0} is 6, 1, 3x10^{13} cm/s, R_s is 2.2, 1.0, 0.6 Ohm, and the exposed edge surface to diode area ratio is 10, 5.5, 2.5x10^{-6} for the 2x2, 3x3 and 5x5 mm^2 cells, respectively.

7.3.2 DWELL cell

Here, the dual diode model is applied to simulate the dark behavior of the DWELL cells:

$$J_d = J_{diff} + J_{rec} \tag{2-a}$$

$$J_{diff} = J_{01}\left[\exp\left(\frac{V - J_d \times A \times R_s}{n_1 V_t}\right) - 1\right] \tag{2-b}$$

$$J_{rec} = J_{02}\left[\exp\left(\frac{V - J_d \times A \times R_s}{n_2 V_t}\right) - 1\right] \tag{2-c}$$

where the dark current is decomposed into the diffusion (J_{diff}) and recombination (J_{rec}) parts. The diffusion part from the bulk is the same as in the GaAs control (equation 1-b), but the edge component is adjusted from SRH statistics to treat the nonradiative recombination current in quantum dots with constant ideality factor (n_2) and reverse saturation current (J_{02}). The parameters are the same for the three different scales, where J_{01} equals J_{b0}, n_1 equals n_b, J_{02}=$7*10^{-8}$ mA/cm^2, and n_2 is 2.

7.3.3 Model comparison

Good agreement is achieved between the model and the data for Figs. 7-2(a) and (b). It is found that the edge recombination current is proportional to the perimeter of the cell, while the bulk current scales with the cell area. Therefore, as predicted by the simulation and confirmed experimentally, the smaller cells, which have a comparatively larger P/A ratio, are more susceptible to the edge recombination phenomenon. Any minor disagreement between the experiment and model can be explained by our assumption that there is uniform edge recombination current across the device perimeter and that n_b and J_{b0} are constants. The edge recombination component has been simplified to a 1D model with constant etched depth and surface states over the exposed perimeter. In reality, however, the recombination current is most intense near the contact fingers and decreases with distance away from the metal edges. This was verified by 2D electroluminescence of the device and a SILVACO ATLAS simulation.

Although the DWELL and GaAs control cell were processed in the same run, the humps in the ideality factor disappear completely in all of the DWELL cells as demonstrated in Fig. 7-2(c). Similar to previously published observations [8], the DWELL structure is effective at blocking lateral current flow to the device perimeter where surface recombination can occur. Although thermal re-emission and non-radiative recombination generally increase the dark current of the DWELL cells compared to the control ones, the overlapping IV curves shown in Fig. 2(d) for different size DWELL devices further supports the idea that the dots play an effective role in suppressing edge current.

7.4 Quantum dots size dependent solar cell efficiency

Embedding quantum dots in GaAs solar cell *pin* junction has been employed Smaller quantum dots lead to better quantum confinement, and thus the higher energy for ground transition. The energy for the ground state transition increases with the decreasing dots size. By using k.p method to calculate valence band to intermediate band transitions, it is theoretically predicted that the reducing quantum dot size increases photocurrent [21]. We measured the photoluminescence of four wafers: 1. 6 stack small DWELL without InP strain compensation (SC) layer; 2. 6 stack small DWELL with SC; 3. Large 6 stack DWELL without SC; 4. Large 6 stack quantum dots with SC (Fig. 1). Four samples have the same design for epitaxial layers. The emission peak would slight red shifted after adding the strain compensation layer (Figure 7-3).

Two components Gaussian curve fitting are applied on the photoluminescence spectrum for separating the emissions from quantum well and quantum dots. The Gaussian component with shorter wavelength is from the quantum well, while the longer one is the quantum dots emission. The central wavelength, full wave half maximum, intensity of the emission peaks are given in Table 7-2. Sample 1 and 2 contains smaller quantum dots and thus their emission wavelengths are ~200nm shorter than sample 3 and 4. The variance is also represented by the emission peaks. The intensity ratio between quantum dots and quantum well represents the carrier distribution between quantum well and quantum dots.

TABLE 7-2 Parameters of DWELL layers' photoluminescence at RT

		λ	E_0	FWHM	I	I_{QD}/I_{QW}
1	Dot	1106 nm	1.12eV	41.76 nm	0.88	1.42
	Well	1043 nm	1.18eV	43.81 nm	0.62	
2	Dot	1120 nm	1.11eV	31.88 nm	0.54	1.07
	Well	1098 nm	1.13eV	62.09 nm	0.50	
3	Dot	1270 nm	0.97eV	28.74 nm	0.75	2.40
	Well	1230 nm	1.00eV	76.83 nm	0.31	
4	Dot	1333 nm	0.93eV	29.60 nm	0.74	1.70
	Well	1279 nm	0.97eV	75.02 nm	0.43	

* 1,2,3,4 are correspondent to samples marked in Fig. 7-3; Dot: Emission of InAs quantum dots; Well: Emission of InGaAs well; λ: Wavelength of the ground transition; E_0: Energy of ground transition; FWHM: Full width half maximum; I_{QD}/I_{QW}: Intensity ratio between the quantum dots and well emission

The accurate solutions can be obtained by solving Hartree-Fock formulation for electrons and holes with three dimensional simulations. Considering the complex structure of InAs quantum dots, I apply the simplified equation for estimating the effective radius of InAs quantum dots. The first approximation for effective ground state transition of InAs quantum dots would be:

$$E = E_g + \Delta E_c = E_g + \frac{1}{R^2}\left(\frac{1}{m_e^*} + \frac{1}{m_h^*}\right)\frac{h^2}{8} \tag{3}$$

Where R is the effective average radius of the quantum dots. E_g is the band gap of bulk InAs; E_c is confinement potential; $m_e^* = 0.028m_0$ and $m_h^* = 0.33m_0$ [22] are effective mass for electron and holes respectively; h is Planck constant. From the ground state energy

measured from PL, the effective radius for samples 1-4 are 4.35, 4.39, 4.83, 5.02 nm respectively (Table II).

Although the solar cells on four different wafers are processed in cleanroom in the same run, the random quantum dots distribution and non-idea alignment during photolithography and correspondent etching process would introduce variance for samples' photovoltaic performance throughout the wafer. Figure 7-4 show the configuration of samples with three different sizes defined on a quarter wafer. Panel (a-d) show the short circuit current (I_{sc}), open circuit voltage (V_{oc}), Filling Factor (*FF*) and Efficiency respectively. The V_{oc} and *FF* are uniform except the edge region, but I_{sc} varies more among the devices. We defined solar cells with three different sizes (Fig. 7-4d). Little systematical difference is observed for solar cells of different sizes [23].

By comparing Fig. 7-4a-c, we will see the space dependent distribution of the three parameters. Fig. 7-4d maps the solar cell efficiency, which is the product of I_{sc}, V_{oc} and *FF*. The differences between the V_{oc} is 0.18V, compared to the bandgap difference 0.17eV. At low temperature, the FWHM is narrower and the emission peaks blue shifts about tens of nanometers. The picosecond scale Auger carrier-carrier interaction dominants the carrier relaxation in quantum dots, with non-trivial role of phonon emission at room temperature [23]. The quantum dots with smaller size and well positioned energy level is expected to reduce thermal carrier escape, and thus increases the photocurrent and open circuit voltage.

7.5 Carrier transport in DWELL structures

The carrier diffusion to the surface states on cell edge is inhibited by the in-plane carrier scattering provided by InAs/InGaAs Dots-in-a-Well (DWELL) layers in standard *pin* diode structure grown by Stranski-Kranstanov method. The typical DWELL solar cell exhibits higher photo-current and dark-current. The contributions from quantum dots to photocurrent include (1) extra photo absorption in IR region (2) assistance to dissociate photo-excited carriers in localized quantum dots states. External quantum efficiency (EQE) shows factor (1) contributes less than five percent to the photocurrent enhancement, while the DWELL samples exhibit 41% higher photocurrent than the control. The self-aligned quantum dots would guides carrier vertically transported in *pin* junction. In quantum well plane, random dots with high uniformity would shorten the lateral diffusion length and block other random oriented shunt channels. Also, further work on engineering the band diagram to optimize vertical carrier transport between DWELL multilayers also presented. We explore the relation between photo and dark current by comparing the photo/reverse saturation current ratio for different *epi* layers, including GaAs control, 6 stack DWELL with/without strain compensation (SC), and 13 stack DWELL with SC. The photo absorption and carrier transport efficiency is further analyzed through EQE with reverse bias.

7.5.1 Carrier confinement in DWELL plane

The efficiency under AM 1.5G of the GaAs control cell decrease from 8.85% to 7.41%, as the size shrinks from 25 mm^2 to 4 mm^2, compared to the increase from 7.04% to 8.17% in

the DWELL solar cells. The lower open-circuit voltage in the smaller GaAs control cells is caused by higher dark current, and the diode parameters are found to be strongly voltage dependent. The divergence from traditional diode behavior is caused by the non-uniform current distribution in the plane perpendicular to carrier transportation in GaAs control sample. Without DWELL structure, the surface states on the perimeter of solar cells would non-radiatively consume the laterally diffused carriers, so the Fermi level in the depleted region would bend down/pinned to surface hold-like states. Laterally, the quantum dots with average 15nm diameter and 6×10^{11} cm^{-2} density are randomly distributed in plane. Vertically, they are lined up between the quantum well layers. The quantum dots are self-assembled, so the local coherent length is decreased to less than 0.1μm, compared to the diffusion length in GaAs (70 μm at high injection). The edge current component is absent for DWELL cells.

This strongly voltage-dependent reverse saturation current can be attributed to the disrupted crystal lattice on exposed edge surface, where the recombination rate is enhanced by the dangling bonds [19-22]. The quasi Fermi level of electron and holes moves with external voltage supply. The trap-assisted carrier consumption is most serious when the maximum of carrier population is driven to the defect states on edge, as the band diagram illustrated in figure 7-6. It is noted that the band diagram is not tilted by applied voltage in the depletion region, because the build-in electric field is perpendicular to xz plane.

7.5.2 Carrier transport through DWELL layers:

Figure 7-7(a) shows the I-V characteristics for the 3x3 mm^2 GaAs control cells. The control cell (red line) has an open circuit voltage (V_{oc}) of 0.89V and a short circuit current density (I_{sc}) of 9.1 mA/cm^2. The 6-stack InAs QD solar cell with (or without) strain compensation has an open circuit voltage (V_{oc}) of 0.72 V (or 0.68 V) and a short circuit current density (J_{sc}) of 10.5 mA/cm^2 (or 12.2 mA/cm^2). Then the photocurrent is decomposed through single diode equation $J=-J_{ph}+J_{d0}\,exp(V/nV_t)$, where n and J_{d0} are local ideality factor and reverse saturation current. J_{ph} is photocurrent, and V_t is thermal voltage at room temperature. The three IV curve shares the same cross point, implying the linear relation between J_{ph} and J_{d0}.

Both n and J_{d0} are voltage dependent and reach their minimum value at the same bias, excluding the series and shunt resistance effects. The voltage bias for minimum ideality factor are 0.39, 0.43, 0.49, 0.92 V for 6 stack DWELL without SC, with SC, 13 stack with SC and control respectively. It is noted that J_{ph} does not equal to short current density for 13 stack DWELL sample. J_{ph} is the current value at reverse bias V=-1, due to low shunt resistance for that sample. By substituting the $\Delta J_{ph}/\Delta J_{d0}$ =0.5e6 into the single diode model, it is found that the diode ideality factor is around 1.8 for Vc=0.61V.

7.5.4 Carrier transport efficiency with reverse bias

To understand the photocurrent generation and carrier transport in DWELL layer, the EQE is also tested in order to confirm that *pin* junction works classically. Compared to control samples, the DWELL cells show extended response up to ~1200 nm due to the absorption of long wavelength photons by the DWELL layers. EQE of 6-stack DWELL cell increases very little (<2%) in the wavelength range of 500-870 nm compared to an increase of about

10% in the wavelength range of 900-1100nm. The noise level increases with increasing reverse bias beyond 1200 nm. The light absorption from quantum dots (>870nm) contribute just 1% extra light absorption, which is subtle compared to the measured enhancement from 9.17 to 12.93 mA/cm^2 for control and DWELL cells (41% enhancement). It is worried that the defects in DWELL structure would consume carriers, so strain compensation layer was applied to balance the interfacial states. However, the high band gap GaP strain compensation layer suppress both light and dark current, and shows limitation on balancing the strains when the number of stacking layers doubles.

Different from other photovoltaic devices (such as Laser, LED), solar cells suggest carrier pairs to separate rather than combine. EQE here is defined by multiplying internal quantum efficiency (IQE) to carrier transport efficiency (CTE) and charge collection efficiency (CCE). CTE represents the drift and diffusion of charge carriers in *epi* layer. CCE is determined by the charge delivering from semiconductor to metal.

$$EQE(\lambda, V) = IQE(\lambda) \times CTE(V) \times CCE \tag{4}$$

Incremental absorption plots in Fig. 7-8 (a-c) are the differential EQE spectrum (EQE enhancement the input wavelength blue shifts 1nm). The absorption is proportional to IQE and confirmed to be stable over different bias in well grown samples (Fig. 3 (a-b)). The first peak locating at 880nm in Fig. 7-8 (a-c) represents the absorption edge of GaAs, and the multiple peaks in the frequency range from 900nm to 1100nm fingerprints excited states in DWELL layer. The photoluminescence (PL) in Fig. 3 (d-f) shows the ground state of quantum well and dots. The main peak at 1106nm is from quantum dots, and the shoulder

around 1045nm marks the lowest energy level for band to band transition in quantum well. The full width half maximum (FWHM) of quantum dots PL is 80nm for 6 stack with and without SC, and slightly expanded to 90nm for 13 stack DWELL with SC (Fig. 7-7 (d-f)). The FWHM represents the DWELL layer-to-layer uniformity.

With different reverse bias, the IQE stays same, unless the vertical alignment between DWELL layers is disturbed by grown process (13 layer sample as shown in figure 3(c)). Figure 2 (g-i) are correspondent CTE. Since the band gap difference between InAs and GaAs is 0.44eV, it is assumed that 100% carrier transport efficiency is achieved when the *pin* layer is reversely biased 1V. CTE is obtained by CTE(V)/CTE(V=-1). The transmission channels provided by quantum well locating at ~920nm and 1030nm, and the extra enhancement above 1050 nm is from quantum dots.

7.5.4 Charge collection efficiency and surface plasmonics

Different from carrier transport efficiency, charge collection efficiency is independent of wavelength and bias (for Ohmic contact here). The photocurrent is observed to be size dependent in DWELL cells. The small cells with denser finger grids exhibit higher photocurrent density. Since the enhancement is absent in control cell, it may due to the surface plasmonics between periodic metal array coupled to DWELL layers, as reported in DWELL detectors [25]. The field enhancement from metal grid assists charge collection when it travels close to surface. Transparent conductive electrodes are also considered to further enhance the plasmonic-quantum dots coupling, especially large scale grown graphene with demonstrated multiple advantages [25-27].

The InAs/InGaAs DWELL solar cell grown by MBE is a standard *pin* diode structure with six layers of InAs QDs embedded in InGaAs quantum wells placed within a 200-nm intrinsic GaAs region. The GaAs control wafer consists of the same *pin* configuration but without the DWELL structure. The typical DWELL solar cell exhibits higher short current density while maintaining nearly the same open-circuit voltage for different scales, and the advantage of higher short current density is more obvious in the smaller cells. In contrast, the smaller size cells, which have a higher perimeter to area ratio, make edge recombination current dominant in the GaAs control cells, and thus their open circuit voltage and efficiency severely degrade. The open-circuit voltage and efficiency under AM1.5G of the GaAs control cell decrease from 0.914V and 8.85% to 0.834V and 7.41%, respectively, as the size shrinks from $5*5mm^2$ to $2*2mm^2$, compared to the increase from 0.665V and 7.04% to 0.675V and 8.17%, respectively, in the DWELL solar cells.

The lower open-circuit voltage in the smaller GaAs control cells is caused by strong Shockley-Read-Hall (SRH) recombination on the perimeter, which leads to a shoulder in the semi-logarithmic dark IV curve. However, despite the fact that the DWELL and GaAs control cells were processed simultaneously, the shoulders on the dark IV curve disappear in all the DWELL cells over the whole processed wafer. As has been discussed in previous research on transport in QDs, it is believed that the DWELL cells inhibit lateral diffusion current and thus edge recombination by collection first in the InGaAs quantum well and then trapping in the embedded InAs dots. This conclusion is further supported by the almost constant current densities of the different area DWELL devices as a function of voltage.

7.6 CONCLUSIONS

In summary, compared to GaAs *pin* diode cells that experimentally display degradation of the dark current and ideality factor as the device perimeter/area ratio is increased, solar cells with an InAs/InGaAs DWELL structure positioned in the intrinsic region do not exhibit this problem. The strong peaking of the ideality factor in the GaAs control cells has been theoretically explained by a model that includes bulk and edge recombination effects. Since a hump in the ideality factor of the DWELL cell is completely absent, it is concluded that the DWELL structure limits lateral current movement and subsequent edge recombination. The DWELL devices should be especially useful for concentrated and flexible solar applications for which small area devices are highly desirable.

Also, we characterized the MBE grown InAs quantum dots-in-a-well structures using photoluminescence. The ground transition energy of quantum dots represents their average size, and the intensity ratio between the QD PL and QW PL decreases with the InP strain compensation layer. The samples with smaller quantum dots and low intensity ratio between QW and QDs represents higher short circuit current and open circuit voltage in wafer scale.

Bibliography

[1] R. B. Laghumavarapu, M. El-Emawy, N. Nuntawong, A. Moscho, L. F. Lester, and D. L. Huffaker, Improved device performance of InAs/GaAs quantum dot solar cells with GaP strain compensation layers, *Appl. Phys. Lett.* **91**, 243115 (2007).

[2] S. M. Hubbard, C. D. Cress, C. G. Bailey, R. P. Raffaelle, S. G. Bailey, and D. M. Wilt, Effect of strain compensation on quantum dot enhanced GaAs solar cells, *Appl. Phys. Lett.* **92**, 123512 (2008).

[3] H.-Y. Chen, J. Hou, S. Zhang, Y. Liang, G. Yang, Y. Yang, L. Yu, Y. Wu, and G. Li, Polymer solar cells with enhanced open-circuit volage and efficiency, *Nature Photonics*, **3**, 649 (2009)

[4] N. Nuntawong, S. Birudavolu, C. P. Hains, S. Huang, H. Xu, and D. L. Huffaker, Effect of strain-compensation in stacked 1.3 um InAs/GaAs quantum dot active regions grown by metalorganic vapor deposition, *Appl. Phys. Lett.* **85**, 3050 (2004)

[5] A. Stintz, G. T. Liu, A.L.Gray, R.Spillers, S.M.Delgado, and K.J.Malloy, Characterization of InAs quantum dots in strained $In_xGa_{1-x}As$ quantum wells, *J. Vac. Sci. Technol. B* **18**(3) 1496 (2000)

[6] G. T. Liu, A. Stintz, H. Li, K.J. Malloy and L.F. Lester, Extremely low room-temperature threshold current density diode lasers using InAs dots in In 0.15 Ga 0.85 As quantum well, *Electronics Letters*, **35**, 1163 (1999)

[7] S. Raghavan, P. Rotella, A. Stintz, B. Fuchs, and S. Krishna, High-responsivity, normal-incidence long-wave infrared (λ~7.2μm) InAs / $In_{0.15}Ga_{0.85}As$ dots-in-a-well detector, *Appl. Phys. Lett.* **81**, 1369 (2002)

[8] P. W. Anderson, Absence of diffusion in certain random lattices, *Phys. Rev.* **109**, 1492 (1958)

[9] D. P. Popescu, P. G. Eliseev, A. Stintz, and K. J. Malloy, Temperature dependence of the photoluminescence emission from InAs quantum dots in a strained $Ga_{0.85}In_{0.15}As$ quantum well *J. Appl. Phys.* **94**(4), 2454 (2003).

[10] P. A. Lee and D. S. Fisher, Anderson Localization in Two Dimensions, *Phys. Rev. Lett*. **47**, 882 (1981)

[11] T. Gu, M. A. El-Emawy, K. Yang, A. Stintz and L. Lester, Resistance to edge recombination in GaAs-based dots-in-a-well solar cells, *Appl. Phys. Lett.* **95**, 261106 (2009)

[12] S. J. Polly, M. L. Harris, Z. Bittner, C. R. Plourde, C. G. Bailey, D. V. Forbes and S. M. Hubbard, Effect of cell size on GaAs concentrations with InAs quantum dots, *Photovoltaic Specialists Conference (PVSC), 35th IEEE,* 002057 (2010)

[13] K. R. McIntosh, Ph.D. thesis, University of New South Wales (2001).

[14] http://www.eis.na.baesystems.com/media_resources/ast_mast.htm

[15] S. O. Kasap, *Optoelectronics and Photonics: Principles and Practices*; Prentice Hall: Englewood Cliffs, NJ, 262 (2006).

[16] M. D. Abbott, J. E. Cotter, T. Trupke, and R. A. Bardos, Suns-photoluminescence: Contactless determination of current-voltage characteristics of silicon wafers, *Appl. Phys. Lett.* **88**, 114105 (2006).

[17] P. E. Dodd, T. B. Stellwag, M. R. Melloch, and M. S. Lundstrom, Surface and perimeter recombination in GaAs diodes: an experimental and theoretical investigation, *IEEE Trans. Elec. Dev.* **38**, 1253 (1991).

[18] K. R. McIntosh, and C. B. Honsberg, *16th European Photovoltaic Solar Energy Conference*, Glasgow, UK (2000).

[19] S. J. Robinson, S. R. Wenham, P. P. Altermatt, A. G. Aberle, G. Heiser, and M. A. Green, Recombination rate saturation mechanisms at oxidized surfaces of high‐efficiency silicon solar cells, *J. Appl. Phys.* **78**, 4740 (1995).

[20] W. Shockley and W. T. Read, Statistics of the recombinations of holes and electrons, *Phys. Rev.* **87**, 835 (1952).

[21] M. Alexander, A. Luque, I. Tobías, and A. Martí, The influence of quantum dot size on the sub-bandgap intraband photocurrent in intermediate band solar cells, *Appl. Phys. Lett*. **101**, 133909 (2012)

[22] G. Pellegrini, G. Mattei, and P. Mazzoldi, Finite depth square well model: applicability and limitations, *Journal of applied physics* **97**, 073706 (2005)

[23] R.P. Prasankumar, R.S. Attaluri, R.D.Averitt, J.Urayama, N.Weisse-Bernstein, P.Rotella, A.D.Stintz, S.Krishna, and A.J. Taylor, Ultrafast carrier dynamics in an InAs/InGaAs quantum dots-in-a-well heterostructure, *Optics Express*, **16**, 1165 (2008)

[24] C.-C. Chang, Y. D. Sharma, Y. –S. Kim, J. A. Bur, R. V. Shenoi, S. Krishna, D. Huang, and S. Huang, and S.-Y. Lin, A surface plasmon enhanced infrared photodetector based on InAs quantum dots, *Nano Lett.* **10**, 1704 (2010)

[25] F. Bonaccorso, Z. Sun, T. Hasan and A. C. Ferrari, Graphene photonics and optoelectroncs, *Nature photonics* **4**, 611 (2010)

[26] X. Li, W. Cai, J. An, S. Kim, J. Nah, D. Yang, R. Piner, A. Velamakanni, I. Jung, E. Tutuc, S. K. Banerjee, L. Colombo, and R. S. Ruoff, Large-Area Synthesis of High-Quality and Uniform Graphene Films on Copper Foils, *Science* **324**, 1312 (2009).

[27] K. F. Mak, M. Y. Sfeir, Y. Wu, C.H Lui, J. A. Misewich, and T. F. Heinz, Measurement of the Optical Conductivity of Graphene, *Phys. Rev. Lett.* **101**, 196405 (2008).

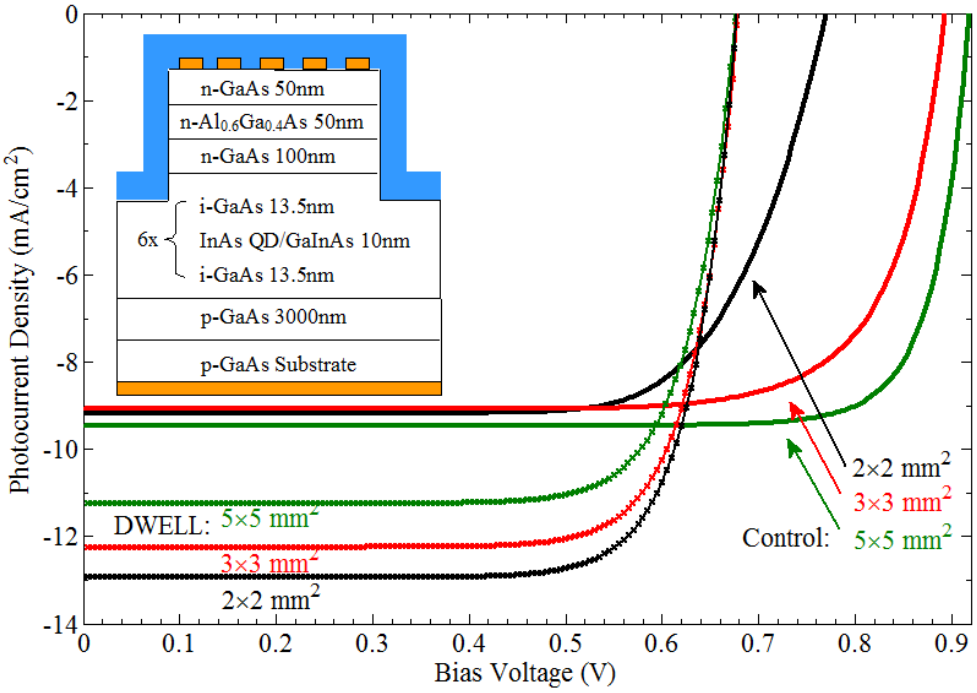

Fig. 7-1 | Photocurrent of DWELL and GaAs control cell of different sizes (2×2 mm^2, 3×3mm^2 and 5×5 mm^2) under AM 1.5G illumination. The inserted picture is the schematic diagram of the DWELL solar cell with six-stacks of InAs QDs embedded in InGaAs quantum wells.

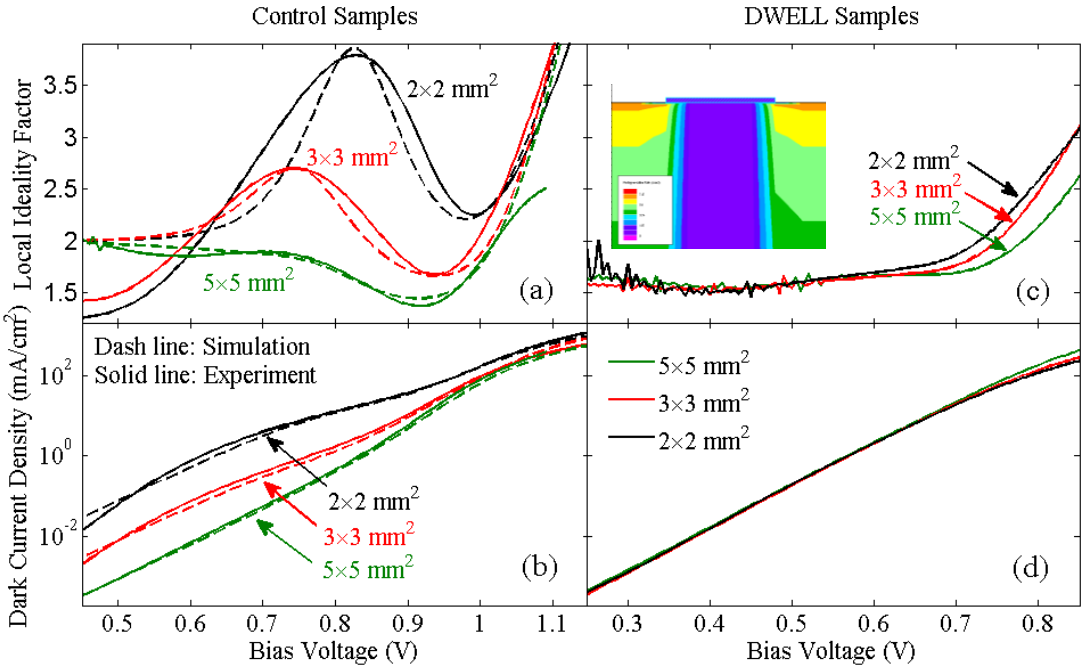

Fig. 7-2 | A comparison of the dark behavior of GaAs control and DWELL cells for the same dimensions (2×2 mm^2, 3×3 mm^2 and 5×5 mm^2). Measured and simulated local ideality factor (a), and the measured and simulated semi-logarithmic dark current density (b) for the control cells. Measured local ideality factor (c) and dark current density (d) for the DWELL cells. The simulation is based on Equation 1(a), where the parameters extracted by the curve fitting are illustrated in the modeling part. The inserted picture is a Silvaco simulation of the non-uniform current distribution in the device.

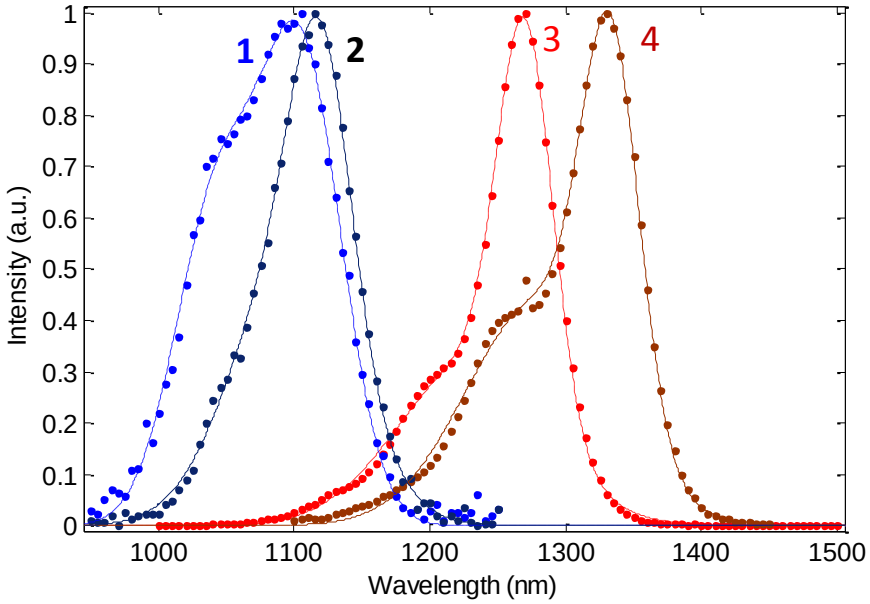

Fig. 7-3 | Normalized photoluminescence of four six stack DWELL samples. The dots are experimental data and the curves are two components Gaussian fitting for QW and QDs. 1, DWELL without InP strain concentration (SC) for small quantum dots size; 2, with SC; 3. larger quantum dots w/o SC, 4. Larger QDs with SC.

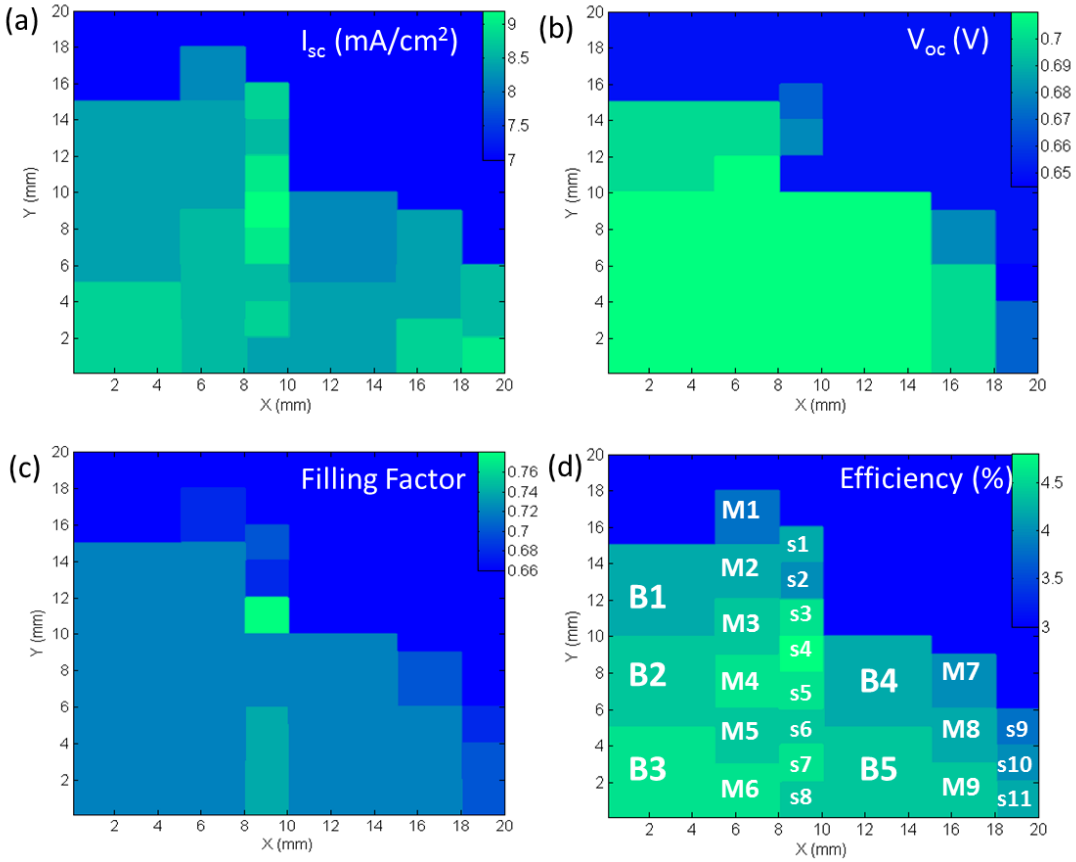

Fig. 7-4 | Wafer scale solar cell performance (6 stack DWELL cells with strain compensation) (a) Short circuit current (b) Open circuit voltage (c) Filling factor (d) Efficiency (%). Solar cells with three difference sizes are numbered in (d). B1-B5: 5 by 5 mm^2, M1-M9: 3 by 3 mm^2, S1-S11: 2 by 2 mm^2

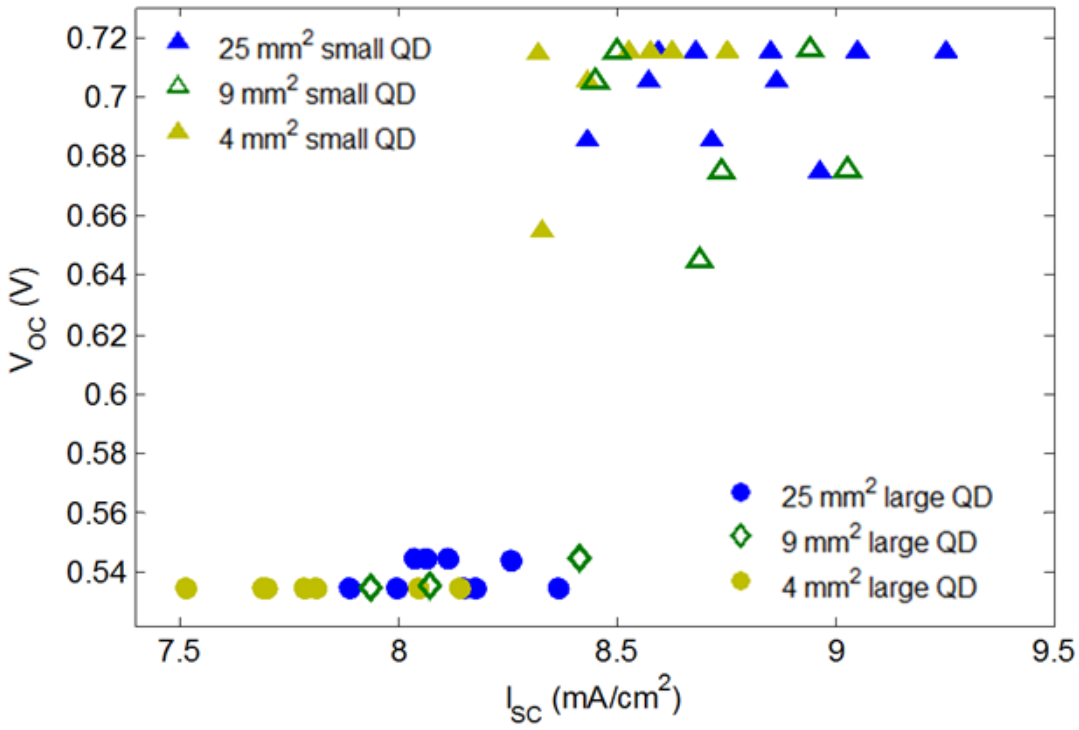

Fig. 7-5 | The open circuit voltage versus the short circuit current for 6 stack DWELL cells with strain compensation (small dots and large dots), with three different solar cell sizes.

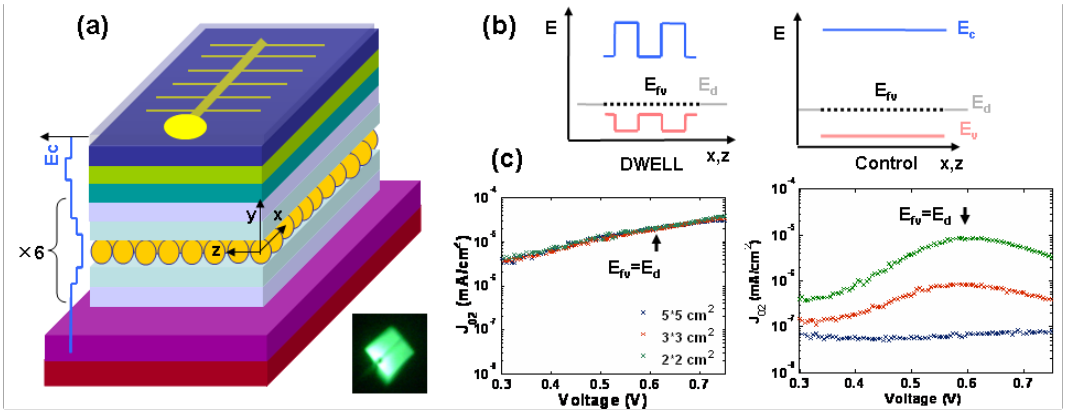

Fig. 7-6 | (a) Bulk structure of solar cells with six-stacks of InAs QDs embedded in InGaAs quantum wells. The inserted picture is the top electroluminescence when the cell is forwardly biased. (b) Schematic band diagram is plotted according to x/z axis for DWELL (left) and Control (right). E_c, E_v, E_{fv} and E_d mark energy level of conduction, valance band, quasi hole Fermi level (under bias V~0.6V), and edge state. (c) Recombination reverse saturation current density for DWELL (left) and control cells (right).

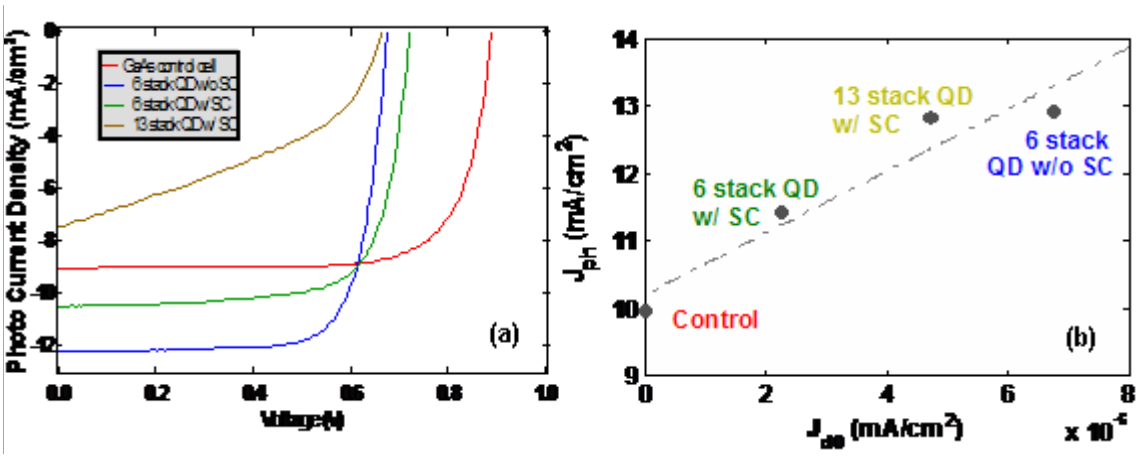

Fig. 7-7 | (a) Measured I-V characteristics of 6-stack w/ and w/o SC, 13-stack DWELL and GaAs control cell under AM 1.5 global illumination. (b) Photocurrent versus reverse saturation current in dark for different samples.

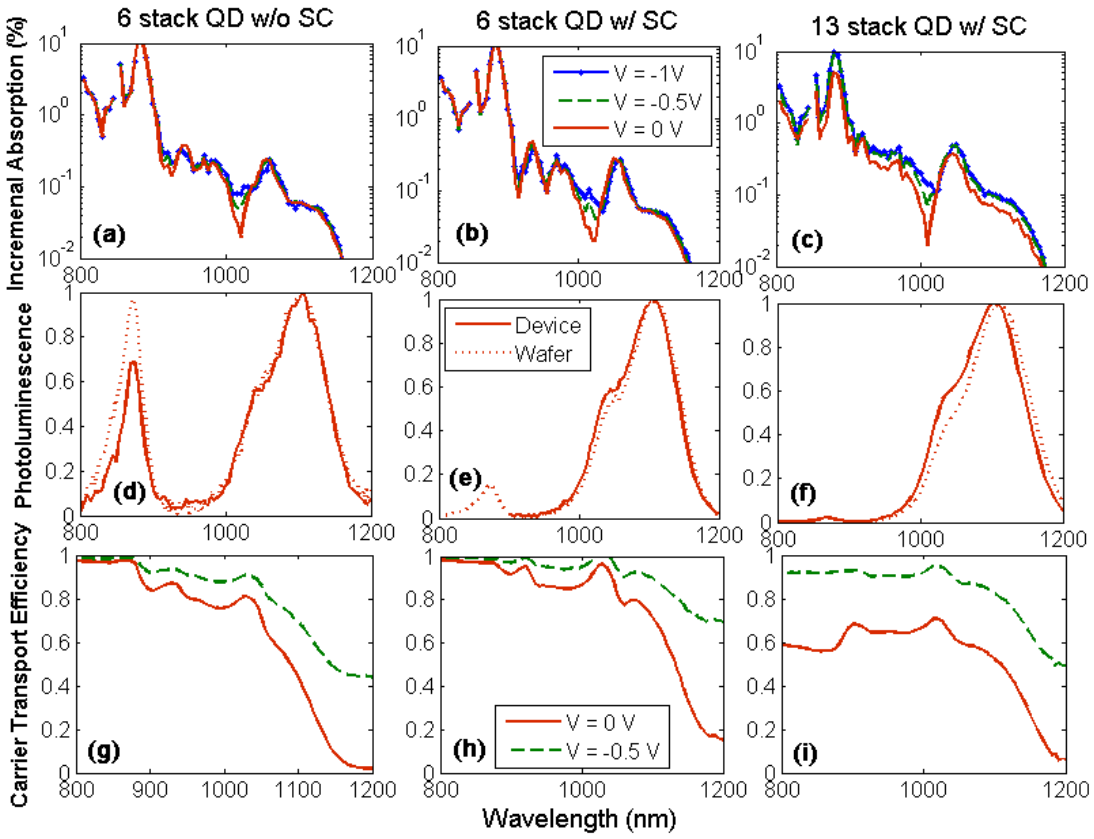

Fig. 7-8 | External quantum efficiency measurement (a-c) Incremental absorption and (d-f) Photoluminescence of device and as-grown wafer (g-i) carrier transport efficiency versus wavelength for three DWELL samples: 6 stack DWELL with/without SC, 13 stack with SC at room temperature. The lines mark the ground state of quantum well.

Chapter 8

Conclusion and perspective

In optoelectronics/nonlinear optics, the electronic structure and population of material are perturbed by electron injection/optical excitation respectively. The perturbation can be externally introduced by electric contacts (Electric field effect or carrier injection), magnetic field or optical beam injection. The probe (weak) light would follow the alternation of the electronic structure of the atoms/molecular, and deliver the information to the transmission port. Dispersion and absorption modifies the photon propagation by changing the real and imaginary parts of the media refractive index.

In classic region, both of the dispersive and absorptive effects can be manifested in the optical resonators. The enhancement is proportional to the ratio of quality factor and cavity mode volume (similar scheme can be applied to slight light enhanced light-matter interaction). In this thesis, we explored various chip scale nanostructured semiconductor materials, and probe the electron/phonon dynamics through cavity resonance shifting, which modifies the intensity of transmitted light and spectrum. The ways for controlling the spectral and temporal properties are investigated numerically and experimentally. The new properties of different materials could be matched to enhance the existing optical device functionalities, such as bistable switch, tunable radio-frequency photonic source, wavelength converter, tunable filter, etc.

On one side, the integrated geometry provides a robust platform to test the material properties, in terms of optical nonlinearity, electro-optic tuning, opto-electronic response, etc.; An appropriate combination and design of material and geometry with specific functionality would provide a protocol for industrial products. Nanostructure increases the surface versus body volume. The contribution from the surface recombination would further

shorten the electron lifetime and fastens the device speed, but the shortened diffusion length would enhance dark current and degrades its photovoltaic performance. Table 8-I summarize specific demands of the material for optoelectronic devices.

Table 8-1: Optimized material properties for target optoelectronic functionalities

Material properties	**Demand**	**Junction structure**	**Photon lifetime**	**Electron lifetime**
Solar cell (DC)	High absorption, broadband	Vertical	Long	Long
Detector (AC)	High absorption, fast	Vertical	Long	Short
Modulator (AC)	Low absorption, fast	Lateral/ Vertical	Short	Short